

**ALMA MATER STUDIORUM
UNIVERSITÀ DI BOLOGNA**

ARCES – ADVANCED RESEARCH CENTER ON ELECTRONIC SYSTEMS
FOR INFORMATION AND COMMUNICATION TECHNOLOGIES “E. DE CASTRO”

**A SKIN SURFACE CHARACTERIZATION SYSTEM
BASED ON CAPACITIVE IMAGE ANALYSIS**

Alessandro Gherardi

TUTOR

Professor

Alessandro Bevilacqua

COORDINATOR

Professor

Riccardo Rovatti

COTUTOR

Professor

Roberto Guerrieri

PHD THESIS

January, 2005 – December, 2007

PHD PROGRAM IN INFORMATION TECHNOLOGY

CYCLE XX – ING-INF/06

To Elisabetta, my wife

Contents

Abstract	iii
1 Introduction	1
1.1 Motivation and objective	2
1.2 The human skin	3
1.3 Skin characterization: conventional approaches	8
1.4 Thesis outline	16
2 Skin characterization system	19
2.1 The capacitive device	19
2.2 The acquisition system	24
2.3 Device characterization	27
2.4 Dataset of capacitive skin sample	40
2.5 Conclusion	42
3 Capacitive images quality assessment	45
3.1 Introduction	45
3.2 Extracted features	46
3.3 SVM classifier	48
3.4 Experimental results	50
3.5 Conclusion	52
4 Algorithms	53
4.1 Skin surface characterization	53
4.2 Feature extraction and testing methodology	61
5 Experimental results	73
5.1 Feature sensitivity	73
5.2 Skin ageing evaluation	76
5.3 Repeatability of measures	82

5.4	Computational complexity	84
5.5	Conclusion	84
6	Applications: follow-up studies	89
6.1	Introduction	89
6.2	The method	90
6.3	Experimental results	93
6.4	Conclusion	98
7	Final Conclusion	101
A	Skin acquisition framework	107
B	Basic notions	113
	Publications	117
	Bibliography	119

Abstract

DURING the last few years, several methods have been proposed in order to study and to evaluate characteristic properties of the human skin by using non-invasive approaches. Mostly, these methods cover aspects related to either dermatology, to analyze skin physiology and to evaluate the effectiveness of medical treatments in skin diseases, or dermocosmetics and cosmetic science to evaluate, for example, the effectiveness of anti-aging treatments. To these purposes a routine approach must be followed. Although very accurate and high resolution measurements can be achieved by using conventional methods, such as optical or mechanical profilometry for example, their use is quite limited primarily to the high cost of the instrumentation required, which in turn is usually cumbersome, highlighting some of the limitations for a routine based analysis. This thesis aims to investigate the feasibility of a non-invasive skin characterization system based on the analysis of capacitive images of the skin surface. The system relies on a CMOS portable capacitive device which gives 50 micron/pixel resolution capacitance map of the skin micro-relief. In order to extract characteristic features of the skin topography, image analysis techniques, such as watershed segmentation and wavelet analysis, have been used to detect the main structures of interest: wrinkles and plateau of the typical micro-relief pattern. In order to validate the method, the features extracted from a dataset of skin capacitive images acquired during dermatological examinations of a healthy group of volunteers have been compared with the age of the subjects involved, showing good correlation with the skin ageing effect. Detailed analysis of the output of the capacitive sensor compared with optical profilometry of silicone replica of the same skin area has revealed potentiality and some limitations of this technology. Also, applications to follow-up studies, as needed to objectively evaluate the effectiveness of treatments in a routine manner, are discussed.

Chapter 1

Introduction

THE SKIN, playing a vital role on the proper health status of the human being, has been widely studied for decades. Lines of investigations cover aspects related to the field of dermatology, to analyze skin physiology and to evaluate the effectiveness of medical treatments in skin diseases. Skin care, however, is not just a matter of health but a matter of aesthetics as well. The human skin surface analysis retains great importance also in dermocosmetics and cosmetic science to evaluate, for example, the effectiveness of anti-wrinkle or hydrating treatments.

During one's life, several factors could affect the skin conditions such as skin diseases or disorders that alter the normal skin functions. Also, environmental factors such as chronic exposure to the sun alter the skin structures and functions, emphasizing this process of changes (*photoageing*) in a different way with respect to common physiological changes that occur in normal skin ageing. In these cases, changes in the skin appearance are induced from both physiological and morphological point of view and as a final result, fine lines and wrinkles appear. Besides, most of these physiological changes are reflected in the outermost layer of the skin which produces the most visible effect. Therefore, the analysis of the topographic changes in the skin surface micro-relief represents a valuable step in order to assess the condition of the skin as well as the individual health status. [1] For these reasons the skin surface topography is, and will long remain, one of the most frequently investigated aspects of dermatologic and dermocosmetic science.

This chapter introduces the motivation and objective of the research work together with an overview of the structure and function of human skin, followed by a review of conventional approaches for characterizing the skin. Finally, an outline of the thesis is provided.

1.1 Motivation and objective

Among the different devices and methods aiming at extracting skin surface properties *in vivo*, only in the last few years some new optical methods have been proposed dealing with mid-cost systems. Conventional approaches have been usually relied on high cost complex system such as mechanical or optical profilometers.

The motivation that support this research work arise from a lack of current methodologies in the skin surface evaluation primarily due to their complexity, device non portability, as well as to the high cost of instrumentations and maintenance required. These factors limit the use of current devices on a large scale. Besides, the main advantage of using skin evaluation systems is the possibility to achieve numerical results of the skin under study. This can lead the typical approach of a *qualitative* and perhaps subjective judgment of the skin condition up to an objective evaluation supported by *quantitative* measurements. However, high cost devices are not so widespread, mainly limited to specialized centers and large hospitals. Even though the final dermatologist advice is properly considered the most valuable judgment for skin evaluation, automatic medical imaging could represents a valid support tool in diagnostic assessment. Moreover, quantitative evaluations are necessary when objective assessment of the skin response to dermatologic or dermocosmetic treatments is under study. Typically, starting from a pre-treatment condition, the skin must be followed up during the therapy in order to evaluate the clinical response. A skin assessment tool in this context can provide numerical quantification of this response to help dermatologists in the evaluation process. However, most of the dermatologists still have to rely on qualitative analysis only and any other supporting tool for quantitative evaluation is precluded.

The objective of this research is to evaluate the feasibility of a low cost skin analysis system able to give quantitative measurements of the skin status based on image processing techniques. Images are based on a principle of acquisition previously unseen in the skin surface analysis context: the skin is imaged by a capacitive device. This device is compact and the system for skin acquisition and evaluation could be easily integrated into a portable system. These characteristics are of a great importance for a large scale skin analysis system. Moreover, a compact and portable system can also be employed when measurements have to be achieved in a routine approach, such as in the case of treatments evaluation using follow-up methodology.

1.2 The human skin

The skin represents the body's first line of defense against the exterior environment. As the largest organ of the human body, and since it covers the whole body, skin has the largest surface area with respect to all the other organs. It weighs more than any single internal organ, accounting for about 15 percent of body weight. It has many important functions that are critical to our well being. Skin prevents or reduces the attacks of viruses, bacteria, chemical substances and even ultraviolet light. It regulates body temperature by blood flow and evaporation through sweat. The secretion of sweat and skin lipids cause the elimination of a number of harmful substances resulting from internal metabolic activities. Also, skin protects the body from friction and impact wounds thanks to its flexibility and toughness. Furthermore, skin can act as a sensory organ as well, since it has a large amount of nerve fibers and nerve endings. When exposed to sunlight skin produces vitamin D, which is a necessary substance for the body. These functions of the skin tend to vary according to age, race, gender and individual health status. When the skin gets older, for example, it tends to lose its flexibility and toughness. [2]

The skin is divided into layers of different thickness according to each body site. In Figure 1.1, the typical schematic structure of the human skin is depicted. Here, the three main skin layers of epidermis, dermis and hypodermis are shown.

Epidermis

The external layer of the skin is the epidermis, which represents the main barrier against its surroundings. Here is where the main skin protective actions are performed. The total thickness of epidermis is of 0.027 - 0.15 mm depending on the different body site considered. Only at the lower base of the epidermis (*stratum basale*) some blood supply is present, whereas in the upper regions no blood support is present. This is why the epidermis is mostly formed by dead cells. The newly generated cells in the lower region replace the older ones that in turn are progressively displaced toward the upper regions. These cells are organized in a network fashion with cytoplasmic bridges that connect each other (in the *stratum spinosum*) which serves as to provide structural support to the epidermis, helping the skin to resist deformations due to stress and strain. [3]

The outermost section of the epidermis is the *stratum corneum*, which is a stratified structure composed mainly of dead cells, called corneocytes, em-

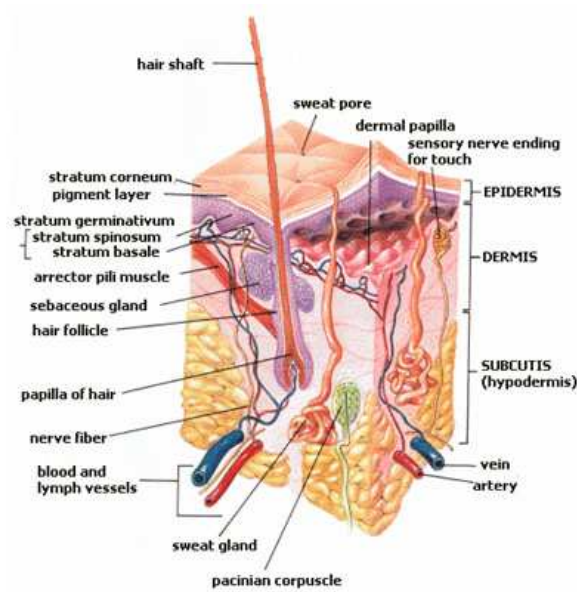


Figure 1.1: The layers of human skin.

bedded in a particular lipid matrix forming a rigid and impermeable layer. The thickness of this layer is approximately of 0.01 - 0.02 mm, being greater in palms and soles which are areas mainly subjected to interface directly the environment. The regenerative process which changes normal epithelial cells into a keratin filled structure (called *keratinization*) is fundamental in order to maintain the functionality of the epidermis, since most of the dead cells are lost during the interaction with the environment. [4]

The epidermis also propagates and absorbs light. The absorption property comes mostly from melanin, a natural chromophore, which is produced by cells called melanocytes in the stratum basale. From the electrical point of view, skin capacitance depends mainly on the water content of the stratum corneum.

Dermis

The dermis is a 0.6 - 3 mm thick vascularized structure [3] primarily composed of dense, irregular connective tissue with nerves and blood vessels and contains nerve terminations, sweat and sebaceous glands. The dermis is formed by two regions: the papillary dermis and the reticular dermis.

The former is composed of loose areolar connective tissue. Above the fingerlike projections called papillae, the epidermis grows (see Figure 1.1). This

region serves as a strong connection tissue between the dermis and the epidermis. Also, the typical contour pattern found on the surface of the skin is due to the papillae formation. By projecting into the epidermis, the papillary dermis forms ridges along the whole body and “friction ridges” in the palms, fingers, soles and toes. In these dermatoglyphic sites, where ridges pattern are mostly genetically determined, friction ridges help increasing hand and foot friction in order to better grasp objects. Moreover, these ridge pattern are unique to each individual, making it possible to use fingerprints or footprints as a means of person identification and verification. [3]

The latter, the reticular region, is beneath the papillary region and it is the largest part of the dermis. It is formed by dense irregular connective tissue made of fibroblast cells, which is a type of cell that synthesizes and maintains the extracellular matrix that supports tissues and gives cells structure from the outside. The dense concentration of protein fibers such as collagen, elastin, and reticular fibers give the dermis its properties of strength, extensibility, and elasticity. Along with soft keratin, collagen fibers are responsible for skin strength and elasticity, and degradation of these fibers leads to wrinkles that accompany the aging process. This region contains also most of the active structures on the skin, such as hair follicles, sweat and sebaceous glands, receptors and blood vessels (see Figure 1.2).

Hypodermis

Although usually not considered properly part of the skin, the innermost layer of the skin is the hypodermis, also known as adipose tissue layer because it contains over 50% of the total body fat. It is composed of loose elastic and adipose tissues and has two main functions: firstly as a strong connection layer between the skin and the muscles or bones beneath, and secondly for thermal insulation purposes. It also serves as a protective layer by absorbing impacts from the outside that could result in internal damage for nerve endings and blood vessels. [3] The size of this layer varies considerably throughout the body. It can be up to 3 cm thick in the abdomen and totally absent in the eye lids. Most of the visible light that reaches this tissue is reflected back to the upper layers.

1.2.1 Skin surface pattern

The intact surface of the skin presents a characteristic pattern due to the presence of intersecting lines that forms the skin *micro-relief*. These fine wrinkles,

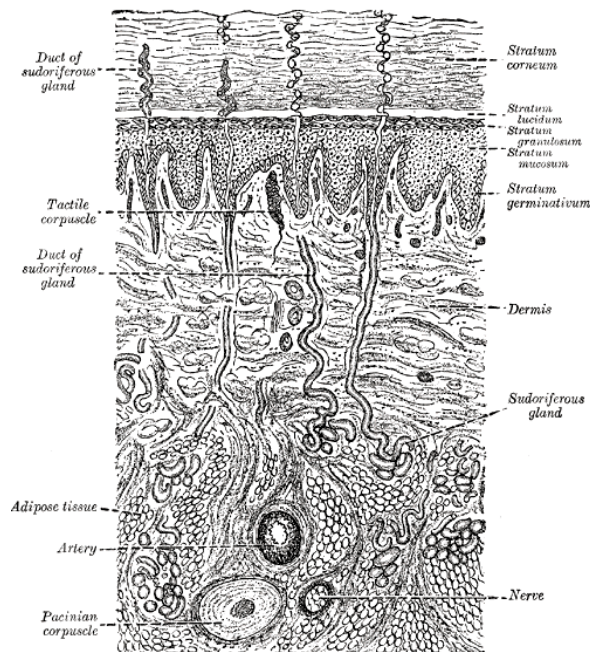


Figure 1.2: Drawing of a cross section of the skin revealing the main components of the epidermis and dermis layers.

also referred to as *sulcus cutis*, are furrows that cross each other and form squares, rectangles, triangles and trapezoids, as shown in Figure 1.3. These lines are oriented along the direction of elastic tension proper of each body site. The surface is also pitted by pores constituted by the orifices of sweat glands and hair follicles. Pores and lines of the skin surface give every region of the body a unique and characteristic topography, mostly established before birth whilst other lines appears afterward, as a consequence of wounds or ageing. Ageing, for example, emphasize preexisting congenital lines that become wrinkles and furrows as skin gets older. Deep analysis of each surface pattern show that each area of the body is peculiar to each individual. Dermatoglyphic zones such as fingerprints are chosen as a means of personal identification due to their highly remarked relief, which is more evident and easily obtainable with respect to other body sites. [3]

It is readily apparent that skin structure varies to some degree over the human body; the stratum corneum is thicker on the palms of the hands and soles of the feet where the contact with the environment is more frequent, and thinner on the lips or eyelids. Lines of fine wrinkles in the skin micro-relief are classified into primary lines and secondary lines based on their directions,

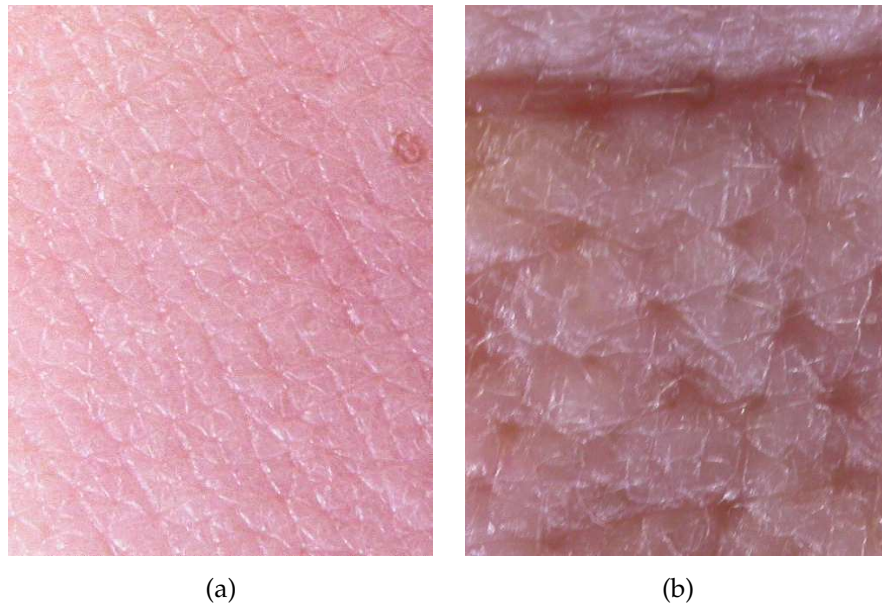


Figure 1.3: Skin surface of a ventral forearm (a) and the forehead (b) of a volunteer as acquired by a CCD digital camera at the same magnification level. Fine lines of the skin micro-relief pattern are visible mostly in (a), whereas in (b) a deep wrinkle and pores are noticeable.

widths and depths. The primary lines are oriented parallel to each other and are much wider and deeper than secondary lines which are shallow and narrow. The secondary lines are diagonal to the primary lines, forming polygonal patterns such as triangles, trapezoids or rhomboids onto the skin surface. The morphology of these lines varies primarily with differences in body regions and age. [5,6] Also, the effect of aging, tends to widen the primary lines making them aligned to a few preferential directions.

1.2.2 Wrinkles

When looking to the closeup images of Figure 1.3, taken with a digital CCD camera with same magnification factor, the morphology of fine wrinkles in the volar side of the forearm (Figure 1.3(a)) is different than the deep wrinkle and structures of the forehead of the same subject (Figure 1.3(b)). Wrinkles are folds of the skin formed through the process of skin deformation, increasing with ageing and occurring more frequently on the face, the neck and the hands. They are an outward sign of cutaneous ageing appearing preferentially on sun-exposed areas (*actinic ageing*).

Wrinkles can be classified into two types: shallow wrinkles and deep wrinkles. The distortion of the epidermis caused by water-loss induce shallow wrinkles to appear on the skin. On the other hand, a decrease of collagen and elastin fibers produces a distortion of the dermis due to loss of elasticity and deep wrinkles are formed.

1.2.3 Skin Ageing

There are clear structural and functional alterations that occur to the skin as it ages. Melanin is produced in less quantity causing sensitivity to light and white or gray hair. Also, due to an uneven distribution of melanocytes in the stratum basale, liver spots can appear. Production of collagen in the dermis diminishes and the skin loses elasticity. Skin sags and wrinkles are formed due to thinning of subcutaneous fat and lose of elasticity. The number of blood vessels, capillaries, and sweat glands diminishes. Also, the moisture content of human skin decreases with age. [7] Beside, it is difficult to ascribe some of the age-related changes to inherent ageing processes or to cumulative environmental damages. In fact, damage may result from repeated chemical assault due to excessive use of soaps or cosmetics, for example, or from a long exposure to UV radiation as sunlight. However, it is generally recognized that the stratum corneum remains essentially invariant during a normal lifespan, though that an intact stratum corneum barrier is necessary for our life. [8]

Skin ageing evaluation has had a great interest in literature especially for the assessment of the skin properties and functions. [9] Knowing a direct relationship between the skin ageing process and the characteristic skin properties under study is crucial in order to infer quantitative assessment of the skin. Since the ageing process changes most of the skin functions and structures, any parameters related to this process is sensitive to changes of skin conditions, thus acting as an viable indicator of the overall skin status. [1]

1.3 Skin characterization: conventional approaches

The human skin have been widely studied for decades. Among the many approaches used to study skin properties, the emerging technologies have been mainly focused on non-invasive methods in order to limit pain to patients. Lines of investigations cover aspect related to dermatology or dermocosmetic science by exploiting characteristic measurements related to mechanical, electrical and morphological properties of the skin.

1.3.1 Mechanical Properties

Most of the mechanical properties of skin are related to friction and suction measurements. To assure body movements, the skin exhibits both flexibility and relative resistance to deformation, allowing temporary compression and distension of a part. Once the temporary deformation has ceased, elasticity normally permits the skin to return spontaneously and progressively to its initial shape. Generally, unaffected skin is never loose or stiff, and the quantification of its mechanical properties can determine its status.

In all the different methods used to quantify the mechanical property of skin, the general process is to press a probe perpendicular to the skin surface and to either pull or push along the skin. Probe sizes, shapes, different materials and differences in measuring techniques are some of the main factors that influence variability in the assessment of skin friction or suction coefficients. Previous studies have focused on correlating the skin mechanical properties with age, gender, anatomical site, and hydration. However, age-related studies have reached disparate conclusions. [10, 11] Despite the many devices that have been developed in the last twenty years, a lot still remains to be accomplished in terms of comparability of the measures and standardization of the results. In fact, even when dealing with the same parameters, different devices could yield different values. [12] Finally, methods relying only on mechanical properties cannot assess topography measurements of the skin. [11]

1.3.2 Electrical Properties

Assessing the skin surface is possible through measurement techniques based on its electrical properties: capacitance, conductance, and impedance. The effect of the keratinization process, as discussed in the previous section, by which the epithelial cells in the epidermis are pushed towards the stratum corneum, is to transform the cell from a soft, living structure to a solid, impermeable layer. Similarly to other proteins, keratin is not a good electrical conductor. Therefore, besides its mechanical and bacteriological protection functions, the epidermis serves also as an electrical insulation layer, having an electrical resistance of more than 1000 times greater than the resistance of the dermis. However, some conductive paths are present: as explained in [13], the majority of the electrical current paths along the skin are concentrated in regions close to pores, where the sweat saline solution offers a higher conductivity path with respect to keratin filled cells of the epidermis. The electrical impedance of the

skin depends on three factors:

1. Temperature
2. Voltage
3. Frequency

Temperature controls the production of sweat in order to prevent overheating. As the sweat is deposited over the skin, the electrical currents are able to bypass the epidermis, and the impedance of the skin is reduced. As long as the voltage applied to the skin increases, the current flowing into the skin produces heat. The skin reaction is to produce more sweat in order to lower the skin temperature inducing a non-linear relationship. Under the threshold of 20V, the characteristic current-voltage relationship is linear. Unlike the epidermis, the cells in the dermis are alive, thus making the skin model a multi-layer membrane. For a constant-field multiple barrier model of membrane the skin current-voltage relation can be modeled as: [14]

$$I = kV \exp\left(-\frac{\Delta G}{RT}\right) \frac{C_o \exp(\xi) - C_{in}}{\exp(\xi) - 1} \quad (1.1)$$

where I is the current through the membrane, k is a constant depending on the membrane permeability, V is the voltage across the membrane, ΔG is the height of the energy barrier, R is the universal gas constant, T is the absolute temperature, C_o and C_{in} are the outside and inside ionic concentrations, and $\xi = VF/(RT)$, where F is the Faraday constant. Equation 1.1 shows that, if the concentrations of ions outside and inside the membrane are different, the membrane has "rectification" properties. Therefore, the current has different values for positive than for negative voltages across the membrane, and its magnitude depends on the membrane permeability to different ion species and its temperature. Also, impedance varies as a function of the signal frequency. As frequency increases, skin resistivity and relative permittivity (ϵ/ϵ_0) non-linearly decrease.

Therefore, the dry stratum corneum acts like a dielectric medium: addition of water makes the stratum corneum responsive to an electrical field. Moreover, with an adequate amount of water in the stratum corneum the skin maintains its intact barrier function, feels soft and flexible and looks smooth and healthy. Typically, electrical methods are utilized for the assessment of skin hydration, such as by using Corenometer devices that rely on capacitance measurements of the skin. [15] The capacitance is measured involving two oppositely charged plates held in close proximity. An electric field is formed between them, and the maximum charge on each plate per voltage applied is

Method	Signal	Resolution	Skin Depth
Photography	Visible spectrum (450–700 nm)	0.1 – 0.5mm	0.1mm
Profilometry	Mechanical stylus	0.1 – 0.5mm	–
Profilometry	Optical interferometry - laser	0.55 – 7.5 μ m	\leq 30 μ m
Ultrasonography	Sound wave (13.5–100 MHz)	60 – 120 μ m	\leq 7mm
Dermatoscopy	Visible spectrum (450-700 nm)	Magnification up to 80 x	2mm
OCT	Near infra-red (700-2500 nm)	5 – 15 μ m	1 – 2mm
Spectroscopy	Visible spectrum and near infra-red (400-2500 nm)	Inversely proportional to fiber diameter	0.1 – 1mm
Confocal imaging	Near infra-red (700-2500 nm)	1 μ m	300 μ m
MRI	magnetic flux (1.5 Tesla)	19 – 70 μ m	\leq 7mm

Table 1.1: Review of the principal non-invasive skin imaging methods in use.

known as the capacitance. When a dielectric material is placed into the gap between the two plates, capacitance value varies according to the the permittivity (ϵ_0) of the material.

By recording the skin's resistance to an electrical current (a few microamperes, in order not to harm the skin), conductance measurements of the skin can be performed. Impedance of the skin present differences according to anatomical locations and environmental conditions. In any case, electrical methods typically rely on a single measurement value (conductance, capacitance or both: impedance) mostly related to the overall skin hydration status under the measurement probe. No detailed and high resolution map are achieved in order to assess topography measurements of the stratum corneum.

1.3.3 Morphological properties

The morphology of the skin surface has had a great interest both in dermatology and in dermocosmetic field by analyzing the main topographic structures such as skin lesions or fine lines and wrinkles of the micro-relief. The process involved in the acquisition of the skin topography is sometimes referred as *skin imaging*.

In Table 1.1, the main non-invasive methods in use for skin imaging and characterization are shown, together with the kind of signal used to image the skin, the planar resolution at the skin surface and the penetration depth into the skin tissue. [16, 17, 18, 19] Briefly, they can be divided in methods relying

primarily on the skin surface evaluation and methods that allow a deeper skin tissue penetration. The former are:

Photography

Through the use of optical devices, photography is the most widely used form of skin imaging. Either in the form of digital image or conventional analogical photograph, this technique could reduce the use of other invasive approaches, like biopsies, in lesion evaluation and melanoma detection. Moreover, digital photography forms the basis of teledermatology. By using polarizing and ultraviolet filters, the surface morphology of skin lines and wrinkles can be enhanced and deeper features like erythema and pigmentation can be also resolved. [16]

Optical devices have been widely used to detect and study different types of skin lesions [20,21,22] by exploiting image processing techniques based on the analysis of features related to shape, boundary irregularities, color, size of cells and skin line patterns. However, this approach suffers from the transparency of skin to light and from the complex changes in illumination and viewing directions. Accurate imaging and light condition setup must be performed prior to the acquisition. These are limiting factors to assess accurate skin topography measures in vivo.

Profilometry

To give measures of the skin surface topography and to quantify its changes, most of the methods are still grounded on skin molds, or negative replicas of the skin zone under study. These non-invasive approaches consist of making a silicone polymer replica of the skin surface and measuring its profile by using either mechanical or optical profilometers [23,24]. When using profilometry, the skin surface analysis yields very accurate measurements in regard to skin topography, for instance depth and width of wrinkles can be measured up to a nano-scale resolution.

Mechanical profilometry involves the drawing of a metal stylus across a skin surface replica. The vertical movements across the surface change the output voltage of the system, from which the surface height can be recorded. In optical profilometry, skin surface replica is assessed by interference fringe projection technique in which the reflection of incident light is dependent on depths and angles of the surface relief. Mathematical modeling allows the valleys and peaks of the specimen to be computed, by extracting characteristic

measures such as Ra (mean roughness) and Rz (surface depth). Today, its use is mostly grounded on quantitative evaluation of hydrating or anti-wrinkle creams (micro-topography). [16]

In [25], authors use a mechanical profilometer to achieve accurate measurements of skin surface roughness, differentiating between solar ultraviolet exposed and normal samples. The two parameters used by the authors are not sensitive for under 30 years subjects. In addition, these parameters are not correlated to chronological ageing in non exposed sites even for over 30 years subjects. Besides, because of the sensitivity of the devices mechanical head, all the experiments need to be accomplished on skin surface replicas.

The work in [23] deals with optical profilometry analysis to achieve skin topography measurements. Nevertheless, new optical profilometers, based on interference fringe projection and other 3D optical systems based on image triangulation have been successfully employed in vivo to measure the skin surface directly. In particular, the light-cutting method has been used to correlate these measures to chronological ageing [26]. This method is suitable for evaluating some skin surface parameters directly, without using replicas. In particular, the authors have found out a correlation between depth (and width) of wrinkles and subjects chronological age. They also compare their direct 3D method and the related replica-based method, finding that their approach always achieves more accurate and reliable results.

However, to our purposes it is worth remarking that profilometers as well as 3D optical systems are very expensive and they could be employed for routine measurements with difficulty.

The other quantitative methods that penetrates the skin tissue for a subsurface characterization are:

High resolution ultrasonography

Ultrasound imaging relies on the differing acoustic impedance of tissues. The path length between transducer and tissue allows time-gated layer separation. This method allows to achieve good sectional images of the skin layers, where epidermis and dermis can be easily resolved. It is primarily used in monitoring and assessment of inflammatory conditions, skin lesion as well as clinical evaluation of skin ageing. [16, 17] In particular, the presence of age-dependent characteristics in some of the skin properties is well established and studied through processing ultrasonographic images of the skin. This technique has been also proposed as a marker of *photoageing*, the cumulative effects of so-

lar ultraviolet radiation. In [8], accurate experiments have been accomplished on a dataset made of ninety Caucasian skin samples, divided into two groups depending on the exposure or non-exposure to the sun, in order to extract features independent from exposure. After an accurate ultrasound device calibration, results show a correlation between chronological age and skin echogenicity of the sub epidermal low-echogenic band (SLEB). In a recent work [27], the authors extend the same study including children and investigating the correlation between photoageing and SLEB also considering different body sites. Differently from what it has been previously achieved, conclusion points out that SLEB might not be a very sensitive and specific marker of photoageing.

Dermatoscopy

Since reflected light from the skin surface limits the visualization of deeper structures, by coupling the light source at the epidermis with a liquid-glass interface, surface reflection can be reduced, enabling a deeper penetration of incident light. Dermatoscopy uses this principle, allowing direct examination and imaging of the epidermis and papillary dermis, to assess pigmented lesions and melanoma, for example. [16]

Optical Coherence Tomography

OCT produces images of skin morphology by using interference pattern that corresponds to layers through the subject tissue, allowing a clear separation of skin tissue at different levels. Subsurface assessment of tissue morphology is possible due to the image generated that resembles an unstained histology section of the skin. It is used in assessment of epidermal hydration, steroid atrophy, ethnic variations and acne lesions. While only the upper layers of skin can be studied, the resolution of this technique may approach the cellular level in the near future. [18] However, so far this method has not been used as a diagnostic tool in clinical evaluations.

Spectroscopy

A spectrophotometer (or spectroscope) separates the returned light into individual colors (according to different wavelengths) and assesses them individually. Its principle is based on the fact that light penetrating the skin tissue is absorbed by different skin components called chromophores, some of which emit radiation back toward the skin surface. Spectroscopy is currently only used in a research setting. The method is used in diagnosis of melanoma and

non-melanoma skin cancer, assessment of biochemical composition and spectral imaging. [16]

Confocal imaging

In confocal laser scanning, light is focused through a lens system at a specific depth. Unlike conventional microscopy, the system allow to target only a chosen plane since the returned light from adjacent layers is inefficiently transmitted. Resolution is very high compared to other subsurface methods and it is possible to visualize cell nuclei and successfully identify all epidermal layers, without requiring an invasive approach such as biopsy. [28] Potentially, this method could be a powerful tool for *in vivo* microscopy since real time imaging is feasible. However, due to the high cost of the system, it is not currently used in the clinical setting.

Magnetic resonance imaging

MRI allows noninvasive visualization of skin tissue in different planes from free and water-bound proton estimation through the use of new supercoils that enhance skin imaging resolution. Thickness measurements and characterization of skin layers are derived through quantitative analysis of intrinsic parameters, such as T1 and T2 relaxation times. [19] Hydration of the skin in normal, aged and diseased states can be assessed. Although it is primarily used in diagnosis of brain diseases, no specific dermatological application has been established. [16]

What emerges from this brief survey is that methods relying only on mechanical or electrical properties of the skin are not enough mature to determine skin assessment in a complete and reliable manner. Also, it must be pointed out that among the different techniques involved in morphological evaluation of the skin properties by skin imaging devices, even though that complex and reliable analysis can be performed, so far no compact and portable system can achieve such measurements. Usually, the most accurate the measurement achieved, the complex and cumbersome the system needed. Moreover, these devices and methods are usually very expensive and new devices based on promising technology are not mature enough to rely on low-cost systems.

Recently, a portable capacitive device has been used to achieve *in vivo* direct measures of the skin hydration [29]. The device has been employed to

achieve skin image samples, later analyzed off-line by dermatologists which counted manually the overall amount of wrinkles [30].

1.4 Thesis outline

This thesis is organized as follows. Chapter 2 deals with the the system developed for the acquisition and analysis of the skin samples. The system, which is based on a prototype version of a capacitive device, will be characterized giving details about the working principles together with advantages and limitations of the method. In particular, to overcome some limitations of the capacitive device, a pressure sensor is integrated into the resulting acquisition system. Moreover, the outcome of the capacitive device is compared with the analysis of the same skin area carried out by using optical profilometry. Also, the methodology used to acquire the dataset of skin samples will be presented. Details about the software and tools developed for the skin acquisition and characterization system are available in Appendix A.

In Chapter 3 a potential problem that affect the acquisition of the capacitive images of the skin by the proposed device is discussed and faced. In fact, most of the images acquired by non trained personnel have been subsequently judged of poor quality by an expert. To overcome this limitation, potentially dangerous for the subsequent feature extraction and evaluation steps, a Support Vector Machine (SVM) classifier has been trained in order to recognize good quality and bad quality images.

The algorithms involved in the analysis of the images acquired by the capacitive device will be presented in Chapter 4. Features are devised to extract characteristic information out of the skin capacitive micro-relief. In particular, three main features will be presented: the first one is based on the area of the skin plateau that forms the typical pattern of the skin and is computed by using the watershed segmentation; the second one is related to a multiresolution analysis carried out using the wavelet transform, whereas the last feature is based on a photometric property related to the local contrast of the enhanced skin wrinkles.

Further on, the results of the experiments accomplished on the whole dataset will be presented in Chapter 5, where the algorithms previously devised for characterizing the skin are tested and evaluated.

After having validated the proposed features, an application of the method in follow-up studies is presented in Chapter 6. The ability to detect changes in

the skin topographic structures is used to keep track of the possible improvements due to a dermatologic treatment. Preliminary results and considerations about the proposed method will be discussed.

Finally, Chapter 7 outlines the conclusions and perspectives of this dissertation.

Chapter 2

Skin characterization system

IN THIS CHAPTER, the system developed for the acquisition and analysis of the skin samples is presented. The system is based on a prototype version of a capacitive device that has been adapted to interface the skin. Details about the working principles that governs the device functionality together with advantages and problems of the device will be discussed. In particular, to overcome some limitations of the capacitive device, a pressure sensor is integrated into the resulting acquisition system. Moreover, the outcome of the capacitive device is compared with the analysis of the same skin area carried out by using optical profilometry in order to characterize the system. Finally, the methodology used to acquire the dataset of skin samples will be presented.

2.1 The capacitive device

To achieve a digital representation of the skin surface, a capacitive device has been used. This device is a prototype version of a fingerprint acquisition device originally developed at the D.E.I.S. department of the University of Bologna. [31] Originally developed for fingerprint acquisition and recognition in biometric applications, the capacitive device relies on an active capacitive pixel sensing technology and it is able to capture detailed images of the skin at a resolution of $50 \mu\text{m}/\text{pixel}$. The active capacitive sensing approach provides much higher immunity to parasitic effects, meaning a higher signal-to-noise ratio and a capacity for capturing images with a higher sensitivity. The sensor's array is composed of 256×360 pixels and is of 12.8×18.0 mm. Each pixel is composed of two adjacent metal plates (Figure 2.1). When live skin is brought *near to* the sensor plates, the skin interferes with field lines between the two plates and

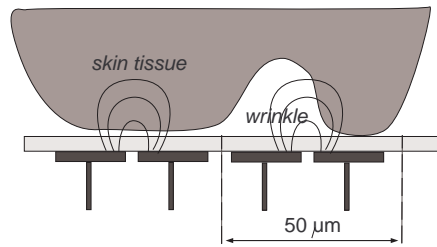


Figure 2.1: Cross section of the sensor schematic principle.

the feedback capacitance is maximized. Conversely, when the skin is moved *away from* the sensor surface the feedback capacitance is minimized. Therefore, the gray level values of the output image represent the 3D skin surface: darker under skin tissue and lighter under skin wrinkles. Images are acquired in real-time by pressing the device lightly over a skin's Region of Interest (ROI). Besides, some physiological factors contribute to a gray level value of each output image pixel. For instance, due to the physics of device pore sweat may originate black spots. Moreover, the thin layer of fat on the skin (often not detected by human eyes being quite transparent) as well as skin hydration can alter the gray level information in a non controlled way.

In order to help the reader to better interpret the device outcome of the capacitive sensor, in Figure 2.2 images taken from different body sites are shown. Figure 2.2(a) shows a ROI of the periorbital region of a 27 years old female. In Figure 2.2(b) it is shown a ROI of a 37 years old female's cheek, (c) shows a ROI of a 37 years old male's forehead, while (d) presents a ROI of the forearm of a 72 years old female. As expected, in this figure it is readily evident that the morphology of the skin varies remarkably with differences in body regions. In the periorbital zone, cheek and forehead no clear topographic pattern can be seen, while in the forearm the primary and secondary lines of the skin micro-relief, which are imaged as bright gray level pixels, are much clear. Moreover, the figure shows how these high resolution capacitance maps can be of a great interest for dermatologists, since even without additional processing they provide detailed information regarding the arrangement of the skin micro-relief.

2.1.1 Working principle

A basic sensing cell of the sensor array is shown in Figure 2.3. Here the sensing principle is based on the feedback capacitance C_r , composed of three plates,

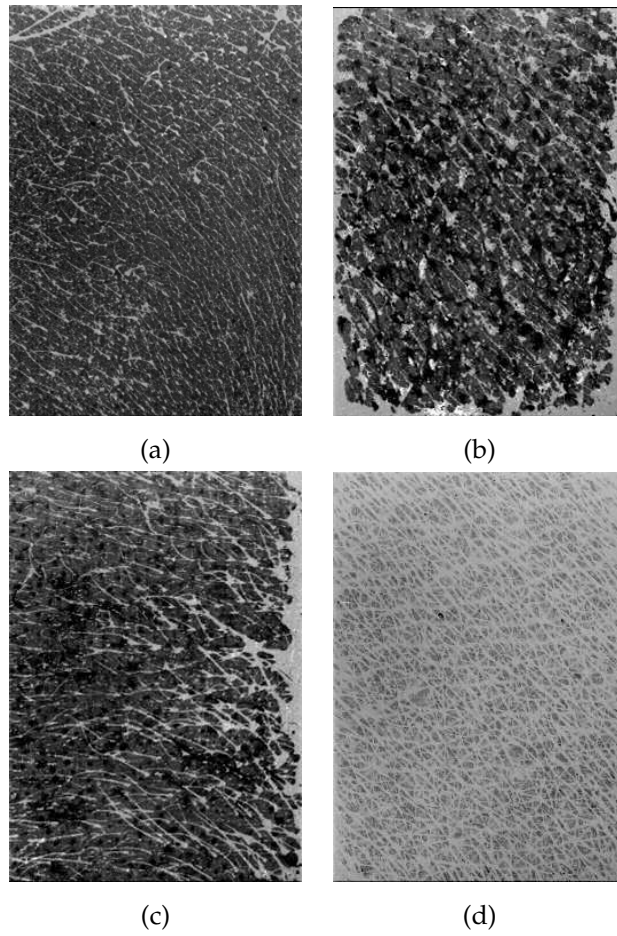


Figure 2.2: Capacitance images referring to a ROI's of a 27 y.o. female's periorbital zone (a), a 37 y.o. female's cheek (b), a 37 y.o. male's forehead (c) and a forearm of a 72 y.o. female (d).

two of which are coplanar and facing the third plate that is floating. The two innermost plates are made in 2-Metal CMOS technology, covered by a thin protective layer of oxide, whereas the outermost floating plate is due to the skin tissue approaching the sensor area.

According to the circuit of Figure 2.3, Equation 2.1 shows that the change in output signal voltage

$$\Delta V_o = \frac{\delta Q}{\frac{C_i}{A_0} + \left(1 + \frac{1}{A_0}\right) C_r} \quad (2.1)$$

is proportional to the amount of charge injected δQ in the charge amplifier and inversely related to the loading C_i and feedback capacitance C_r . As the third plate is assumed floating, a parasitic capacitance C_p is also present due to

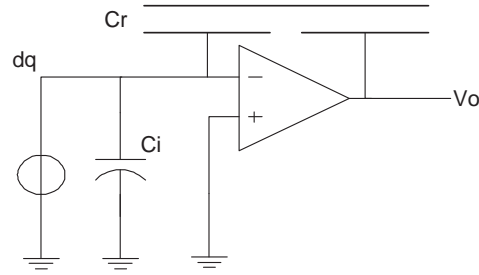


Figure 2.3: Schematic draw of a capacitive feedback scheme sensing microcapacitor composing the sensor array of capacitive cell.

the electric fringing field, so that the real feedback capacitance term is due to $C'_r = C_r + C_p$. By definition the feedback capacitance is:

$$C_r = \frac{\epsilon_0 S}{2d} \quad (2.2)$$

where ϵ_0 is the relative permittivity of the dielectric medium, S is the surface area of the capacitive plates and d is the distance between the sensor plates and the skin surface. When using an high gain amplifier, such as in the case of an high gain CMOS inverter, so that $A_0 \gg 1$, and considering $C_p \ll C_r$, the effective output of the capacitive sensing cell is due to:

$$\Delta V_o \approx \frac{\delta Q}{C_r} = \frac{2\delta Q}{\epsilon_0 S} d \quad (2.3)$$

showing a linear relationship between output signal and the distance between the skin surface and the capacitive device. [31]

However, experimental results have shown that the resulting output value depends also from skin physiological factors, such as moisture contents of the stratum corneum. Moreover, noise alter the gray level value in a non predictable way. Also, the pressure applied between the skin surface and the sensor during the acquisition stage can have a role in the resulting gray level intensity of the capacitive image. Therefore, several issue arise from the variability of the images captured by the sensor. Among the main challenges we can list the following:

- *skin physiological factors* - the condition of the skin surface influences the output of the capacitive cells, so that the more the moisture content of the skin, the darker the gray level of the resulting pixels. As a consequence, capacitance map of the skin may vary according to subject skin dryness or according to time-dependent behavior such as prolonged contact during

the acquisition, where pore sweat activity increases the moisture level on the skin surface;

- *skin hair* - capacitance map of the skin is influenced also by skin hair structures. As the stratum corneum, hair is composed of keratin, a low conductive substance, but the lipids in hair account for only 2% of its mass. Therefore, hair structures are imaged as low capacitance thus giving high gray level values. In any case, skin topography capacitance values are hidden under hair structures;
- *sensor noise* - the capacitive image can be corrupted by speckles unrelated with the skin surface topography such as parasitic effects, quantization noise or pixels stuck at low or high values due to dirt on the sensor;
- *uneven sensor output* - the output response of the capacitive device varies according to pixel displacements, as the sensor shows a different behavior in the upper part of the cell's array, where pixel values tend to deflect to higher gray level values;
- *contact pressure* - as long as contact pressure between the capacitive sensor and the skin surface increases during the acquisition, structures of the skin topographic micro-relief become more evident in the resulting image. Therefore, a too high value in contact pressure may determine large distortions of the imaged skin structures. By contrast, a too low pressure may result in partial and uncomplete acquisitions of the real skin micro-relief. Moreover, gray level values change accordingly to pressure values, as the distance between the sensor capacitive cells and the skin topographic micro-relief varies.

An example of these problems is shown in Figure 2.4, which resembles many of the device issues. This figure shows capacitive image samples acquired during an acquisition stage. Here, the contact pressure increases from left to right, showing remarkable differences in the capacitive images acquired. At a low pressure of about $0.016N/mm^2$, only part of the effective skin topography is imaged, whereas progressive increase in contact pressure reveals the real micro-relief. We can also notice the effect of fuzzy hair on the skin surface, as imaged by curvilinear structures with bright pixel values. To an untrained eye, these structures tend to mismatch with lines and fine wrinkles of the skin micro-relief. Differences in hydration state of the skin are visible: zones with high moisture contents are marked by low gray levels, especially in the high pressure image at right. Moreover, pore perspiration activity is clearly visible

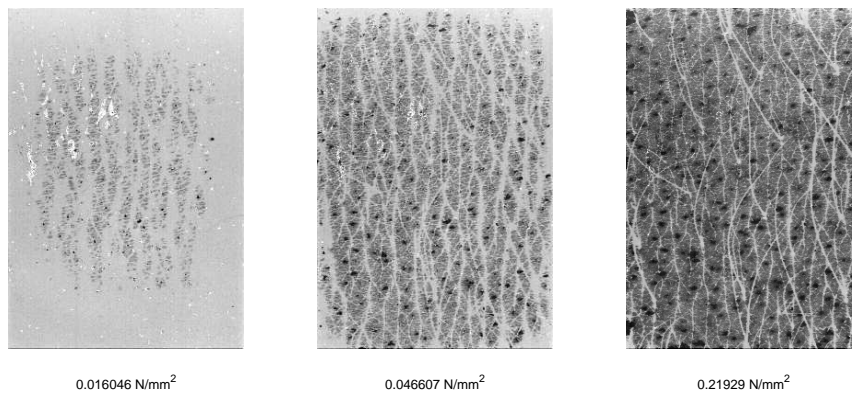


Figure 2.4: Sensor issue related to skin physiological factors, sensor noise, uneven sensor output and differences in contact pressure during acquisition.

as depicted by black spots through all the images. In this figure, it is readily apparent the effect of noise: the very white pixels are due to a non proper cleaning of the device before the acquisition took place. Finally, if we take a close look at the first image, the upper region shows brighter pixel levels. This is due to an artifact of the device sensor readout, in which the sensor output response varies according to the displacement of the addressed cell.

Prior to make any assessment of the skin surface by the device, we are therefore forced to address these issues.

2.2 The acquisition system

The capacitive device by itself could not be employed directly for a reliable skin surface assessment. The limitations outlined in the previous section are too restrictive in order to extract quantitative measurements out of the skin capacitive images in a reliable manner.

Although some countermeasures to limit the impact of these drawbacks can be demanded to software based algorithms after the acquisition of the images, other device problems have to be tackled at system level. In particular, noise and output response shift could be addressed by image processing filtering algorithms designed on purpose. Also, capacitance values response due to changes in physiological factors, which cannot be faced at system level, may be addressed at software level by studying features related to these skin properties. Nevertheless, these properties can be related to interesting phenomena such as effective skin hydration.

Specification	Typical value
Measuring range	0 – 20Kg FS
Sensitivity	2mV/V FS
Total error	$\leq \pm 0.5\%$ FS
Repeatability	$\leq \pm 0.1\%$ FS
Power supply	5V DC
Diameter	16.5mm

Table 2.1: Pressure sensor specifications.

However, changes in gray level output due to differences in contact pressure must be faced properly with adequate instrumentation. In order to improve reliability, the contact pressure during each capacitive image acquisition should be kept under control. To this purpose, a pressure sensor has been integrated into the skin acquisition system. This sensor is a miniaturized load cell (DS Europe, IT), placed under the sensor active area and having axial alignment according to the direction of the perpendicular force applied to the sensor during acquisition.

Table 2.1 shows the main technical specifications of the pressure sensor. The pressure applied through a compression force is converted into an electrical signal by sensing the deformations of a strain gauge. The output voltage, which is within a millivolt range, is then amplified and normalized through a signal conditioning circuit before being converted by an ADC converter into a digital form suitable for computer processing. To this end, a Digital Acquisition Board (DAQ - Minilab 1008, Measurement Computing Inc., USA) in differential input mode has been used. After having calibrated the pressure sensor in the new setting, a software application has been developed in order to record the corresponding contact pressure value for each capacitive image acquired.

Figure 2.5 shows the diagram of the skin characterization system. Here, a hardware layer is composed of a capacitive sensor together with the pressure sensor whose analogic output is converted through the DAQ. An intermediate layer interfaces the hardware devices with the software algorithms by providing driver support. In the software layer, the application is linked by the drivers through the data acquisition interface. A user-friendly graphic user interface (GUI) controls the user input and displays acquired images and results of elaboration by graphic components. The business logic of the application integrates these two components with the image processing unit, where the skin

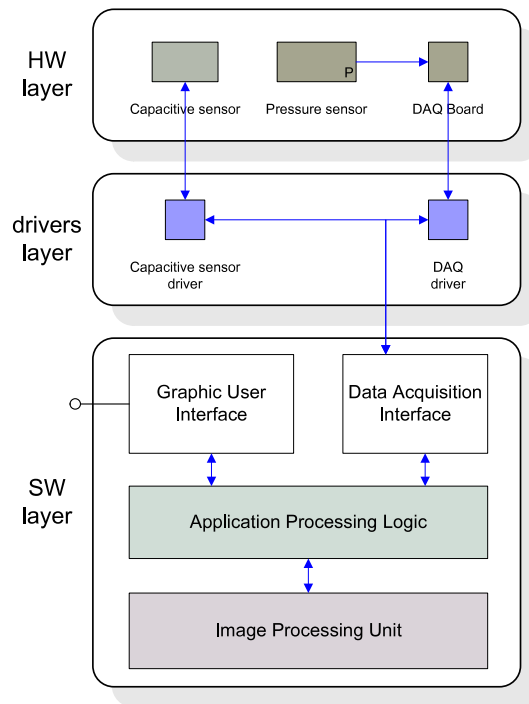


Figure 2.5: Architecture of the skin characterization system.



Figure 2.6: Prototype of the skin acquisition system.

characterization algorithms resides.

The hardware composing the skin acquisition system used is shown in Figure 2.6, where the DAQ board and signal conditioning circuit are visible in the

upper part of the picture, while the capacitive device is on the bottom side of the figure. Here, on the top of the device we have the capacitive sensor, coupled with the load cell beneath the two metal guides.

Details about the software and tools developed for the skin acquisition and characterization system are available in Appendix A.

2.3 Device characterization

The gray level output of each pixel of the capacitive image represents a capacitance map of the skin surface. As pointed out in Section 2.1.1, capacitance is modulated primarily as a function of the distance between the capacitive sensor and the skin micro-relief, as expressed by Equation 2.3. Besides, in this equation the output signal voltage depends also by the permittivity of the medium acting as the dielectric material. Since the stratum corneum is the primary responsible layer that acts as the dielectric in the measured capacitance, variations of the permittivity of the stratum corneum is relevant to the output gray level of each capacitive image pixel. Therefore, the information carried out is not only related to the skin 3D profile of the surface micro-relief, but also to the variable dielectric constant of the skin. Therefore, differences in permittivity of the stratum corneum mainly due to different amounts of water molecules, whose macroscopic effect is viewed as inhomogeneity of different hydrated zones, affect the output gray level of the sensor.

Moreover, the output response of the capacitive device varies according to pixel displacements, as the sensor shows a different behavior in the upper part of the cell's array. Here, the capacitive background image (the image acquired without anything on top of the device sensor area, hereinafter briefly *background*) tends to deflect to higher gray level values. Finally, noise alters the final gray level values of a capacitive image.

Facing these problems is crucial to infer real absolute metric measures from the skin topographic structures detected in the capacitive images.

In order to characterize the system, a comparison between the capacitive sensor output and a ground truth profile of the same skin area is necessary. Since profilometry has been considered one of the most accurate method for the characterization of the skin surface, a validation testbed has been setup to achieve comparison between skin capacitive profile and profilometric measurements. To this end, since high resolution measurement with optical profilometry are not feasible in vivo, because a long time is required to achieve a profilometric map, in order not to corrupt the measurements with movements

of the living skin, a skin replica of the same area covered by the capacitive device sensor has been used for the profilometric acquisition.

A mold of silicone resin (Silflo, CuDerm Inc., USA) has been used to setup a cast of each corresponding body region acquired by the capacitive device. A cardboard skin-safe adhesive locator, adapted to have the same size of the capacitive sensor array, has been placed onto the skin region previously acquired by the capacitive device and subsequently filled by a mixture of silicone resin and catalyst in order to produce the cast.

The negative silicone replicas produced have been further analyzed with an optical profilometer (Veeco Instruments Inc., USA) equipped with a $20\times$ magnification objective and a $.5\times$ scale factor reducer lens, thus giving an overall magnification factor of $10\times$. The system, based on white light interferometry, provides accurate surface data depths of a limited region of the replica, being the field of view of $0.62 \times 0.47\text{mm}^2$ and 640×480 pixel the image resolution.

Comparison between the two measurement system is archived in two ways:

1. **3D skin profile characterization:** the depth of the skin micro-relief profile is compared in order to assess the relationship between the skin capacitive profile and the real skin surface 3D profile;
2. **2D skin surface characterization:** only 2D planar information are compared, limiting the analysis on the skin surface plane only.

In particular, in the first case an analytical model of the capacitance response sensed by the system is devised according to the skin surface profile. In the second case the attention is focused on the inter-wrinkle distance, that is the measure of the distance between two adjacent wrinkles as viewed by a top plane.

Figure 2.7 shows the capacitive image and the photographic (CCD) image of the replica, respectively, referring to the same skin ROI of a 42 male subject arm. The black spots in Figure 2.7(b) point out the regions sampled by the profilometer. For the sake of clarity, each black spot requires many profilometric measures, thus yielding many profilometric image maps (Figure 2.8(a)), accordingly. In fact, due to the magnification lens, each profilometric map measures $627.6\mu\text{m} \times 470.7\mu\text{m}$, requiring more than 756 profilometric map to cover the same capacitive image size. Therefore, in order to have quite a large area to be compared from the two devices, these profilometric image maps have to be mosaiced (Figure 2.8(b)). In this example, the overall area covered by the mosaic is $1.92 \times 0.98\text{mm}^2$. Since a long time is needed in order to setup each profilometric acquisition, covering a larger area is not feasible. The CCD

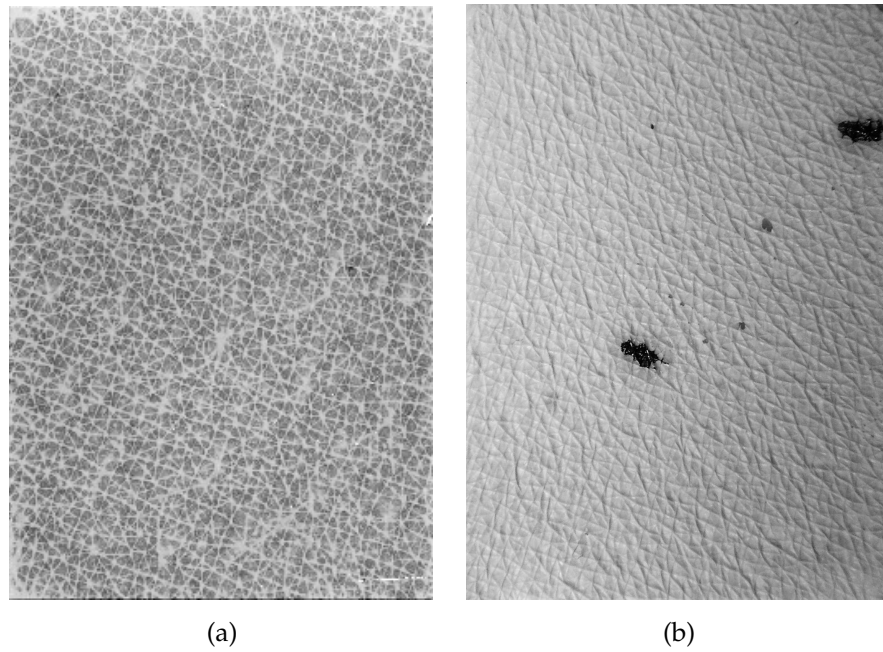


Figure 2.7: Capacitive image (a) and photographic (CCD) image of the silicone replica (b).

image helps us to find out this very small region within the capacitive image. In Figure 2.8(b), the black region refers to both the area not covered by image stitching and the depth not measured by the profilometer, darker and brighter pixels correspond to greater (wrinkle) and smaller (skin tissue) depths, respectively.

2.3.1 Experimental results

Background normalization

In order to correct the shift of the output response of the capacitive sensor in the upper region and to denoise the image coming out of the capacitive device, a background subtraction operation has been performed, where the background B_G is an image generated statistically, according to Equation 2.4:

$$B_G = B^N - \mu_{B^N} \quad (2.4)$$

where B^N is the temporal averaged background image referring to N background images subsequently acquired and μ_{B^N} is the constant mean value computed on B^N . Generating a background statistically is necessary since the

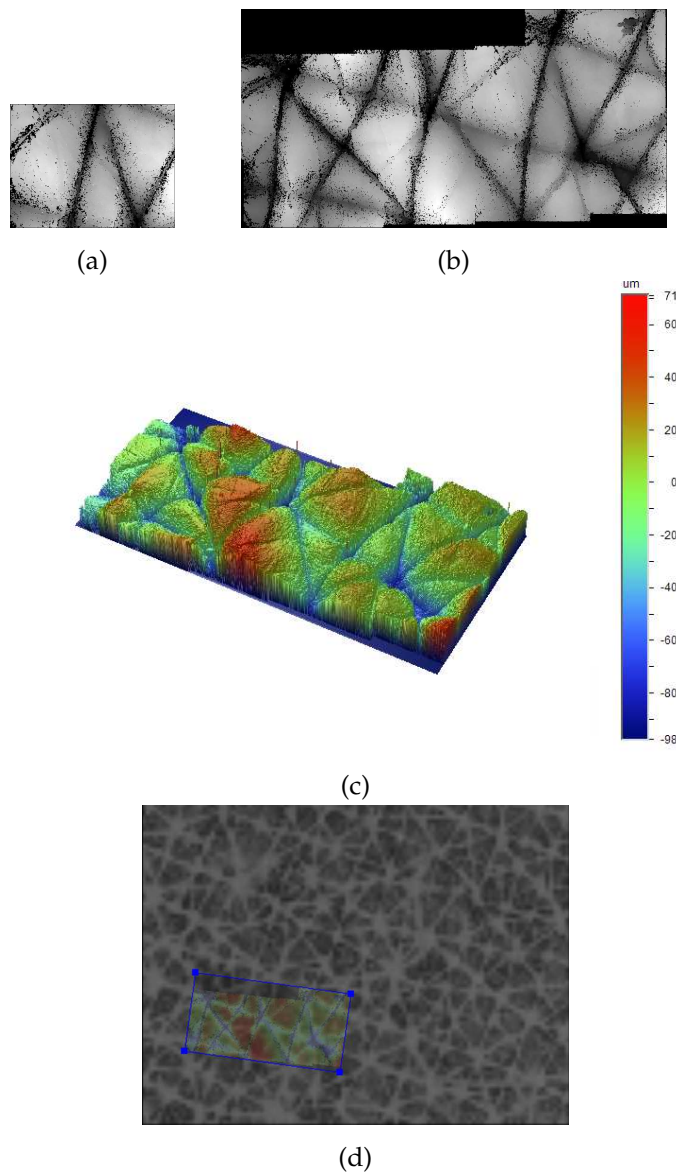


Figure 2.8: One profilometric image (a) and the mosaic (b) referring to the lower black spot of Figure 2.7(b). In (c) the 3D profilometric mosaic is then stitched on the capacitive image to cover the same region (d).

background itself is affected by noise and varying output response according to pixel displacement. Figure 2.9(a) represents a line profile of a generic background image B extracted along the vertical axis from bottom to top (corresponding to the left and the right side of the figure, respectively). As one can see, at right values increase rapidly up to 10%. In order to assess the efficacy

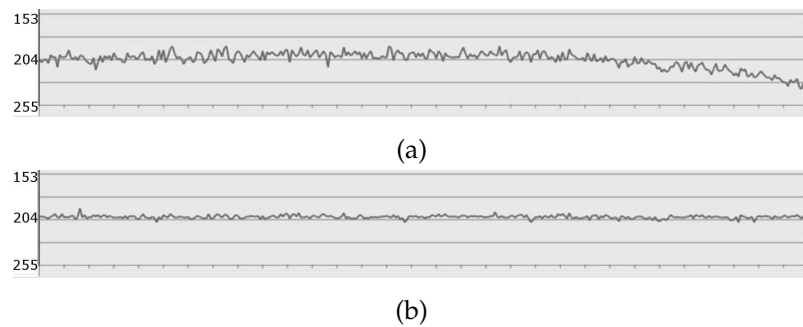


Figure 2.9: Plot profile of a line along the vertical axis of the background image (a) and the corresponding profile after calibration (b).

of the generation operation we extract the same line from the image given by $B - B_G$. Figure 2.9(b) shows that the use of B_G improves the quality of the input image in terms of both calibration (this is a flat field output response, as correctly expected) and signal standard deviation. The calibrated background

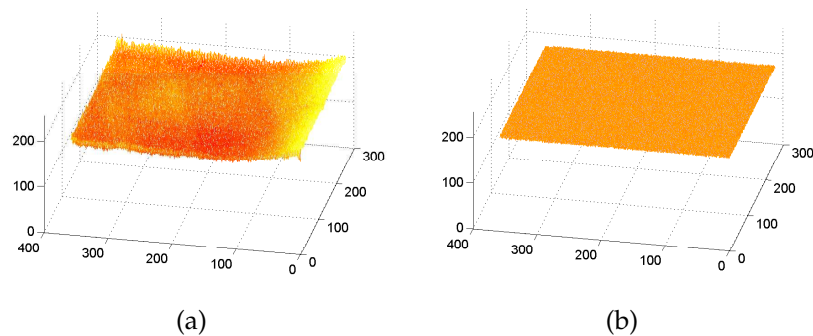


Figure 2.10: A detail of the sensor background image (a) and the corresponding calibrated image (b).

image is shown in Figure 2.10(b) together with the uncalibrated input background (a). After that, the input image to the following module is simply the difference between the image just acquired and B_G .

3D skin profile characterization

The comparison between the profilometer and the capacitive measurement system is archived firstly by analyzing the depth of the skin micro-relief profile. In the first case, in order to assess the relationship between the skin capacitive profile and the real skin surface 3D profile, several skin replica and capacitive samples have been acquired. A supervised tool developed on purpose

has been used to extract the same line profile from these samples, by registering the profilometric and capacitive maps. By drawing a line segment over the two registered maps, corresponding pixel intensity values determines the two line profiles. Since the planar sampling resolution of the capacitive images ($50\mu\text{m}/\text{pixel}$) is quite lower than the acquired profilometric data ($0.98\mu\text{m}/\text{pixel}$), in order to compare the two profile at subpixel level, the profile extracted from the capacitive image has been interpolated by natural cubic spline. To this end, the control points used in the spline interpolation are simply the values of the capacitive image pixels.

Pressure during the acquisition is recorded for each capacitive image. Figure 2.11(a-d) shows a sequence of acquired capacitive images together with the pressure values (e). We can notice in this figure, how low contact pressure yield uncomplete skin micro-relief, while progressive increase in contact pressure reveals the structures of the skin.

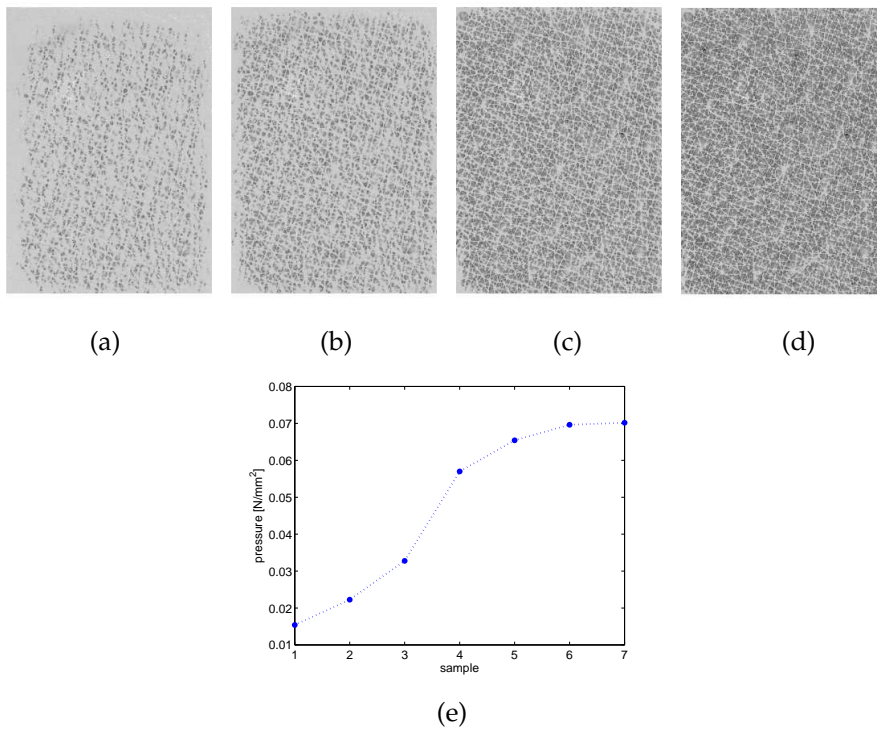


Figure 2.11: An example of samples (a-d) acquired at increasing values of pressure (e). The first two images (a,b) correspond to the first two points of the plot in (e), whereas the last two images (c,d) are acquired at higher pressure values corresponding to the last two points in the plot.

Capacitive images are gray level maps in which each pixel is modulated

according to the sensed capacitance of the skin in a 8 bit range (values from 0 to 255). By contrast, profilometric images are very detailed height maps representing the true skin micro-relief, even though some errors could be present due to the skin replica based process. [32] These maps contains depth values (expressed in μm). In order to compare the two, a mapping between capacitance gray levels and real μm units is needed. In a first setting, the modulated capacitance profile is linearly transformed into micrometric values according to:

$$y_u = gI_c + o \quad (2.5)$$

where y_u is the micrometric result of the capacitive gray level value I_c (which as been normalized in the range $(0-1)$), g is the gain factor and o is the offset. This relationship is due to the fact that, according to Equation 2.3, the capacitive sensor output value varies in a linear fashion with the distance of the sensed skin. The gain and offset will be determined empirically.

Figure 2.12 shows the extracted line profiles referring to the samples shown in Figure 2.11(a-d), at increasing value of pressure applied. Capacitive profile points, which are depicted with blue squares, are interpolated by natural cubic spline to form the capacitive profile shown in red. The profilometric profile, shown in black, looks quite different. Even changing the gain and offset parameters of Equation 2.5, structures do not match. This is even more true at low levels of pressure, as not all the skin topographic structures are imaged (Figure 2.12(a)). As long as pressure increases, the capacitive spline-interpolated profile trend to reshape the fine wrinkles of the real profile (Figure 2.12(c-d)). However, something is still missing. Most of the real profile is distorted and the central wrinkles are not imaged correctly by the capacitive sensor. This mismatch could result from a non perfect alignment of the profilometric and capacitive maps, since the resolution of the two maps is very different and registration errors may become critical.

In another example of profiles extracted from the same capacitive images of Figure 2.11(a-d), a better alignment between the two line profiles is shown. Again, in Figure 2.13(c-d) contact pressure plays an important role in the depth characterization of the real profile. Besides, the better alignment achieved in this case is not sufficient for the characterization of the real profile. In fact, another drawback of the capacitive sensor emerges. The deep wrinkle at the left side of this figure, accurately imaged by profilometry, is not sensed completely by the capacitive device. Contrarily to what happens to the rightmost shallow wrinkle, which is somehow correctly approximated, in this region a sort of sensor "saturation" occurs.

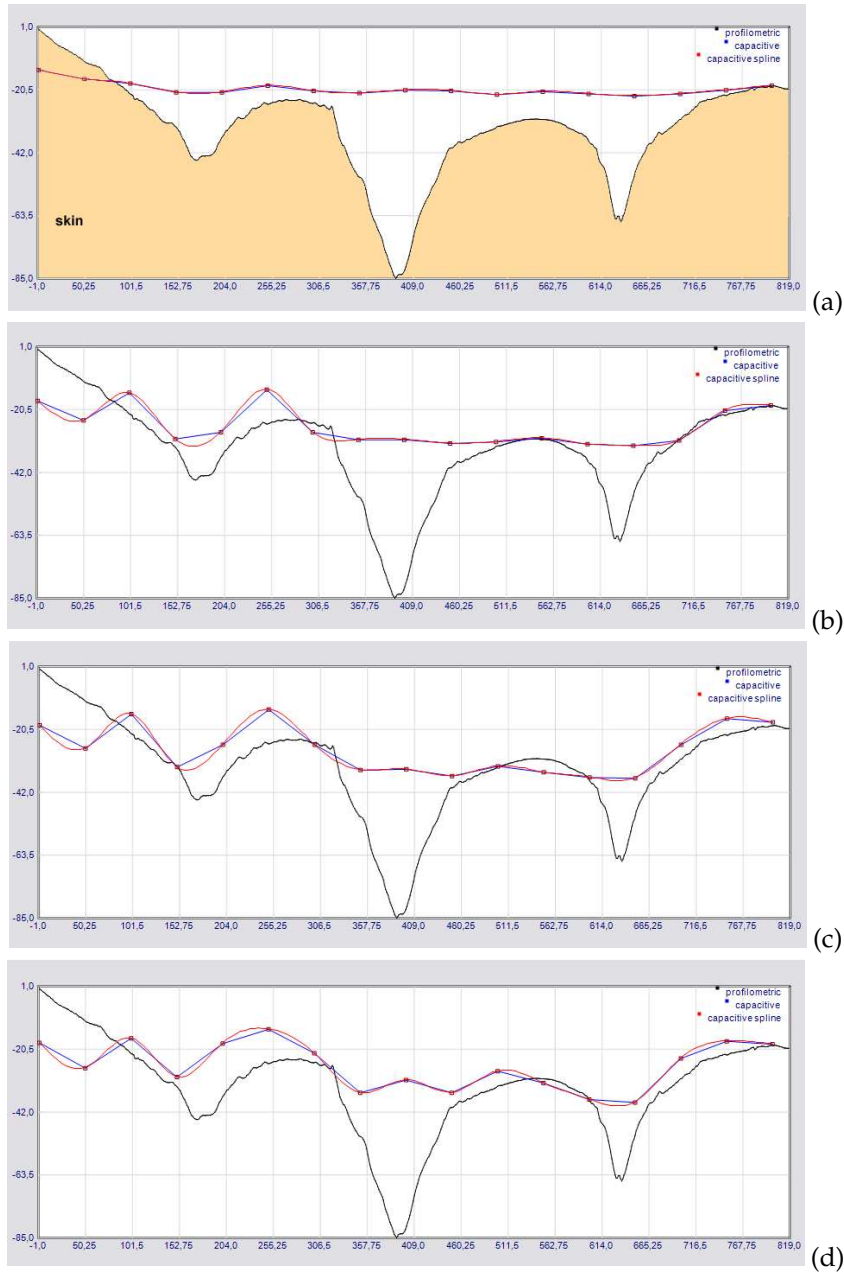


Figure 2.12: An example of non perfectly aligned line profiles referring to the samples shown in Figure 2.11(a-d), at increasing value of pressure applied (a-d). Capacitive profile points (blue squares) are interpolated by natural cubic spline to form the capacitive profile (red curve), which is superimposed on the real profilometric profile shown in black. Units are in μm .

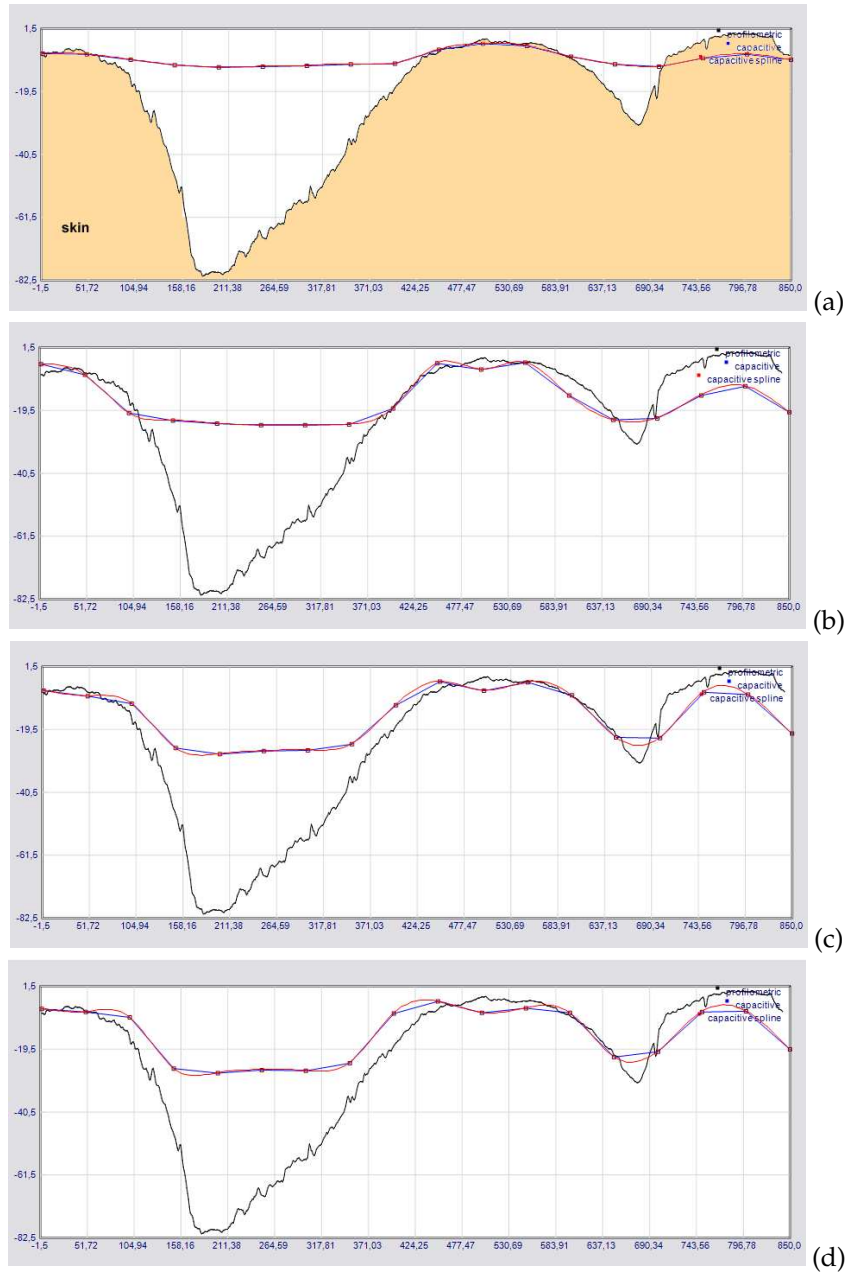


Figure 2.13: Extracted line profile referring to the samples shown in Figure 2.11(a-d), at increasing value of pressure applied (a-d). Capacitive profile points (blue squares) are interpolated by natural cubic spline to form the capacitive profile (red curve), which is superimposed on the real profilometric profile shown in black. Units are in μm . In this figure, profile matching is increased.



Figure 2.14: Gradient based spline interpolation of the line profile referring to the samples shown in Figure 2.11(a-d).

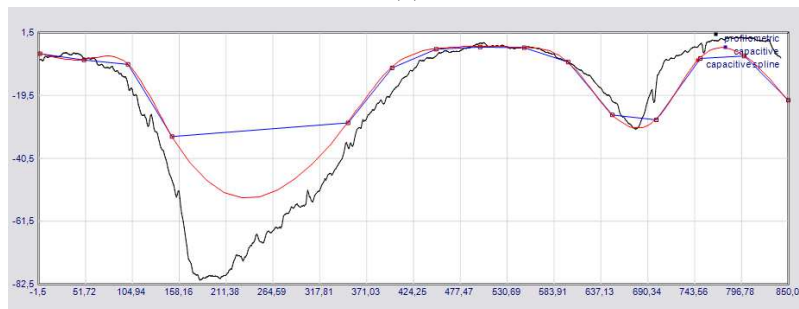
The results of the comparison between profilometry and capacitive images have shown that this behavior is due to a limited sensing of the capacitive device, in which the fringing capacitance field lines are unable to penetrate the skin as deep as is needed. With a gain parameter $g = 65$ and offset o set accordingly to the profilometric profile (in order both to be aligned on top), the maximum measurable capacitive profile depth is $32\mu m$. Wrinkles deeper than this value are imaged as the background value of the image sensor, and therefore saturated.

To try to overcome this limitation, a gradient based approach has been followed in the capacitive profile interpolation. Simply, control points in saturated regions that are close to high gradients of the capacitive profile are automatically removed from the spline interpolation. Experiments on other skin samples have revealed that, once fixed the gain parameter, with the gradient based approach wrinkles depth can be characterized up to $50\mu m$, thereby increasing depth sensing of about $20\mu m$. Result of this method is shown in Figure 2.14. Here, the capacitive profile tend to better resembles the real profilometric data. However, a lack of accuracy is still present.

Another limitation that has emerged from the comparison of the capacitive profiles with real profilometry is due to the fact that capacitive acquisitions rely on a contact method. When the skin is imaged in this way, the contact pressure may deform the outermost skin structures, as it is evident when looking at the top of the capacitive profiles of Figure 2.13, especially for the central ridge. Here, structures of the skin at the top of the profile, which are in direct contact with the sensor, are progressively squeezed. Even the gradient based approach does not resolve this problem (Figure 2.14). Therefore, by taking into account the contribution of these top structures during the acquisition at increasing value of pressure, it is possible to reconstruct the real top profile. The



(a)



(b)

Figure 2.15: Effect of the profile estimation algorithm (a) referring to the samples shown in Figure 2.11(a-d). In (b), also the gradient based spline interpolation method has been applied.

algorithm works by weighting the gray level value of pixels corresponding to the skin structures that first came into contact with the device sensor, in function of the applied pressure to estimate the undistorted profile. Figure 2.15(a) show the result of this method applied to the normal spline interpolated profile, while in (b) also the gradient based spline interpolation method has been applied.

2D skin surface characterization

In the second case the attention is focused on the inter-wrinkle distance (IWD), that is a measure of the distance between two adjacent wrinkles as viewed by the image 2D plane. To achieve and validate an IWD measure, it is necessary to extract the 2D profile of the same line from both the capacitive and the profilometric images. Therefore, following the same method used for the first case, after reducing the resolution of the profilometric image and resizing the capacitive image with bilinear interpolation, the two images are fused manually in

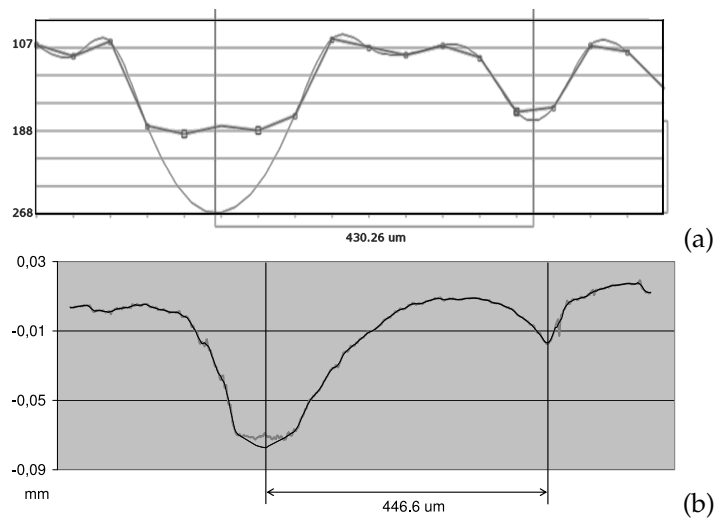


Figure 2.16: Plot profiles of the same line extracted from capacitive (a) and profilometric (b) images.

order to detect same reference points and structures. This is accomplished in a supervised manner by using a graphic tool developed on purpose. Nevertheless, the measures are always attained on the original images.

In order to improve the measure resolution for the capacitive image ($50 \mu m$) a natural cubic spline interpolation of the 2D profile has been performed, thus achieving a sub-pixel resolution comparable with profilometric measurements. However, the maximum depth which can be detected by the capacitive device is limited: as a consequence, for the deepest and largest wrinkles, the profile is flattened and local minima could not be evaluated effectively (left wrinkle of Figure 2.16(a)). Therefore, by using high gradient control points only, the 2D wrinkle profile can be reconstructed effectively, thus making local minima easier to be computed.

In this case, 57 couple of measures (capacitive and profilometric) have been achieved by analyzing different body sites (lower and upper ventral forearm, forehead) of a few subjects, although no significant differences have been noticed in the IWD determination. For each ROI analyzed, at least 6 IWD measures have been computed, depending on the area of the mosaic. The wider the area the more measures can be achieved. The measures attained through the profilometric analysis have been used as the ground truth to validate capacitive IWD's. Figure 2.16 shows a significant couple of such measurements, referring to line profiles extracted from capacitive (a) or profilometric (b) images. The

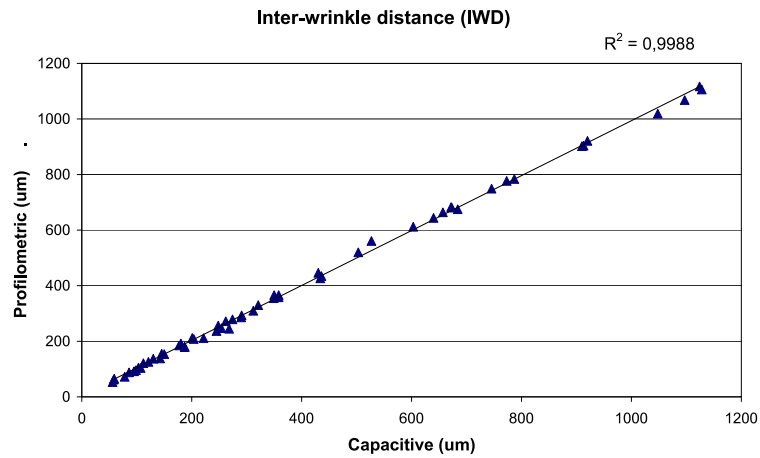


Figure 2.17: Capacitive vs ground truth profilometric IWD measures (in μm).

IWD is measured between the two vertical lines: for the capacitive image the measure is $430.26 \mu m$ while for the profilometric one it is $446.6 \mu m$. The first IWD is 96.3% with respect to the ground truth. All the capacitive IWD measures expressed in μm have been collected and plotted in Figure 2.17 against the ground truth values, where a linear regression has been computed. The correlation coefficient R^2 is 0.998 thus pointing out an excellent linear correlation. The mean absolute error measured between capacitive and profilometric IWD's is $8.39 \mu m$, while absolute maximum and minimum measured errors are $34.0 \mu m$ and $0.1 \mu m$, respectively.

To summarize, the main aspects found regarding the capacitive device characterization can be listed as the following:

- A linear model has been devised according to the capacitive sensing design in order to map the gray-level capacitive profile to a micrometric output. The model has been further enhanced with natural cubic spline interpolation in order to increase the capacitive profile resolution and to allow the comparison with the high-resolution profilometric data. The gain parameter g has been set to a value of 65, according to the experimental results. The offset o represents a regularization parameter of the model that depends only on the alignment between profilometric and capacitive profiles.
- Contact pressure plays a key role during the acquisition: experiments show that when pressure is in a range between 0 and $25 \times 10^{-3} N/mm^2$

skin structures are imaged only partially, yielding incorrect profiles. Above the $25 \times 10^{-3} N/mm^2$ pressure threshold value, skin is imaged correctly up to about $20 \times 10^{-2} N/mm^2$, after which distortion in the skin structures becomes predominant. This upper limit, however, may depend from different body site and from person to person.

Besides, even images acquired at lower value of pressure are important in order to reconstruct the profile, since deformations that occur in skin structures directly in contact with the sensor may be recovered by exploiting low-pressure information;

- The capacitive device shows a saturation effect in the depth characterization of the 3D skin profile: this is due to a limited electric field that penetrates the skin tissue, limiting the appreciable depth to $32\mu m$. By exploiting gradient-based spline interpolation of the sensed capacitive profile, this increases the ability to characterize skin wrinkle depths up to $50\mu m$. However, some of the skin wrinkles could be deeper than this value.
- Planar 2D characterization, as revealed by IWD measures, shows congruent measurements between profilometric and capacitive wrinkle analysis. This proves the effectiveness and the reliability of the measures related to 2D skin topography attained from the capacitive device.

2.4 Dataset of capacitive skin sample

In order to have a remarkable number of capacitive images of the skin at our disposal for devising and testing the skin characterization algorithms, a dataset of capacitive skin samples has been acquired under the supervision of a dermatologists team. Acquisitions of the samples were accomplished *in vivo*, during normal dermatological examinations and after that subjects have signed written consent form. The study protocol was approved by the Independent Ethics Committee of the Maggiore-Bellaria Hospital of Bologna. The chosen body site to sample was primarily the upper ventral forearm of healthy volunteers, whereas forehead, cheek, and other body sites have been acquired as well. This choice, shared by most of the researcher in the field, is due to the fact that in the forearm region, skin topography is better marked with respect to other body sites. Moreover, the ventral forearm region is a quite protected area from exposition to solar ultra violet radiation, and photo-ageing effects are limited. Hair in this region should be absent or limited, therefore reducing possible

mismatch with thin wrinkle structures. Together with the capacitive samples, also optical images of the acquired body region have been collected during the acquisition. This is to have both a reference of the body site acquired and also a comparison with what normally dermatologists are used to see during clinical skin evaluation. A CCD digital camera, with a special illuminator for macro imaging, has been used to take closeups of the acquired skin region with a resolution of 1200×1600 pixels.

Since several factors affect the capacitive skin images during the acquisition stage, a protocol of acquisition has been setup together with the dermatologists, in order to reduce the possible sources of errors. The protocol of acquisition involves the following steps:

1. Before the dermatological examination starts, the subject must relax in order to minimize the effect of changes in temperature and humidity.
2. One of the two personnel in charge of the acquisition (dermatologist A) ask the age of the subject and record the data in the samples database, together with subject's gender, body site acquired and type of skin (caucasian white, black, ...).
3. The other dermatologist (B), firstly cleans the capacitive sensor with a dry gauze and wipes the sweat away from the subject's skin. Only after this process, the acquisition starts by pressing the device over the selected body site. Images are collected in the database of samples together with the recorded data at point 2.
4. Once dermatologist B has finished the acquisition, dermatologist A takes a picture of the acquired body region by the digital camera. Again, this picture is added to the above information stored in the database.

As a result, a first database of more than 250 capacitive and optical (CCD) samples of male and female subjects was collected.

At the time the acquisition campaign was started, pressure information was not yet available. Only in a second setting, also pressure was recorded during the acquisition. Moreover, due to the originality and novelty of the proposed method, previously unseen in the field, dermatologists involved in the samples acquisition were not sufficiently trained to recognize artifacts on the acquired capacitive images. As a consequence, most of the sample acquired in this stage were affected by distortions, limiting their use for the evaluation of the algorithms.

Finally, more than 320 samples constitutes the available dataset.

2.5 Conclusion

This chapter has been focused mainly on the hardware components of the skin characterization system. The capacitive device used to image the skin surface suffers from physiological skin conditions as well as physics due to the acquisition principle. Images have shown that gray levels do not depend only on 3D skin surface information and several drawbacks limit the applicability of this method. Therefore, in order to attain better knowledge of the device, the system has been characterized. In particular, after having calibrated the background to denoise the capacitive images through background subtraction, a profilometric analysis has been carried out. Accurate experiments have been accomplished by comparing the measures attained from capacitive images with the ground truth achieved by an optical profilometer. In particular, the same line extracted from corresponding points in capacitive and profilometric images has been profiled and analyzed.

A linear model has been devised according to the capacitive sensing principle of acquisition, in order to map the gray-level capacitive profile to a micro-metric output. The model has been further integrated with spline interpolation in order to increase the capacitive profile resolution and to allow the comparison with the high-resolution profilometric data. According to the experimental results, the gain parameter g of the model has been set to a value of 65.

The capacitive device shows a saturation effect in the depth characterization of the skin profile: this is due to a limited electric field that penetrates the skin tissue, limiting the appreciable depth with the proposed model up to $32\mu\text{m}$. Exploiting gradient-based spline interpolation of the sensed capacitive profile increases the ability to characterize skin wrinkles depths up to $50\mu\text{m}$. However, some of the skin wrinkles could be deeper than this value.

Contact pressure plays a key role during the acquisition: experiments show that when pressure is lower than $25 \times 10^{-3} \text{ N/mm}^2$ not all the skin structures are imaged, yielding incorrect profiles. Above this pressure threshold value, skin is imaged correctly up to about $20 \times 10^{-2} \text{ N/mm}^2$. Further increasing of the contact pressure yields distortions that occur in the skin structures to become predominant. This upper limit, however, may depend from different body site and from person to person. Besides, by exploiting low-pressure information that occurs in the skin structures directly in contact with the sensor during the images sequence of acquisition, a reconstructed 3D profile might be recovered.

Even though 3D depth profile characterization has revealed limitations of

the capacitive device, measurements attained by considering information related to planar structures only, as revealed by the distance between two adjacent local minima of the profile representing the inter-wrinkle distance IWD measured, have shown congruent numerical quantifications between profilometric and capacitive wrinkle analysis.

This proves the effectiveness and the reliability of the measures related to 2D skin topography attained from the capacitive device.

Finally, a database collection of skin capacitive and optical samples (mainly of the ventral forearm region) has been carried out together with a team of dermatologists. A protocol of acquisition of the skin samples has been studied in order to minimize the source of possible errors and to limit the issues related to the capacitive device.

Chapter 3

Capacitive images quality assessment

THIS CHAPTER deals with a potential problem that affect the acquisition of the capacitive images of the skin by the proposed device. In fact, most of the images acquired by non trained personnel have been subsequently judged of poor quality by an expert. To overcome this unwanted behavior, potentially dangerous for the subsequent evaluation steps, a Support Vector Machine (SVM) classifier has been trained in order to recognize good quality and bad quality images.

3.1 Introduction

In medical image analysis it is of a great importance to deal with correct acquisition of the input images since most of the subsequent analysis strongly depends on this stage. An incorrect acquisition results in a misguided output of the system. Although there exist analytical description of image quality for medical imaging [33], it is widely accepted to take this stage for granted usually by relying on the expertise of a human operator. However, not all the possible applications could count on experts following thoroughly the acquisition stage. When this is the case, an automatic method should be employed in order to guide the operator in making decision about the quality of the image acquired.

The scope of this chapter is to investigate the feasibility of a quality check algorithm based on image analysis techniques and supervised learning algorithms. In particular, relevant features are extracted from the image of the skin

of different healthy subjects acquired by a CMOS capacitive device and then processed by a Support Vector Machine (SVM) classifier.

The capacitive device, which senses the capacitance of the skin by modulating each resulting pixel of the output image in a 8-bit gray level scale, has a resolution of 50 micron per pixel (see Section 2.1 for details). Due to the physics of the device the image formation is different from a classic optical image. Due to the fact it is a contact device, also the pressure applied between the sensor and the skin play a key role in the quality of the resulting image. Moreover, the capacitive image is altered by physiological factors such as pore sweat and differences in moisture content of the skin. Also, before each acquisition, the device must be cleaned in order not to image residuals of the previous acquisition. Therefore, the acquisition is particularly sensitive and great care should be paid during this stage.

The input dataset has been collected during a normal dermatological examination by dermatologists not specifically trained to deal with this particular application. More than 320 samples have been acquired by the capacitive device. A further analysis carried out by an expert has divided the dataset into two groups: a good-samples dataset (GS) of 77 images and a bad-samples dataset (BS) composed of the remaining 250 images, where the former represents the set of acceptable quality images and the latter the one of badly acquired samples, respectively.

3.2 Extracted features

Figure 3.1 shows examples of good quality (Figure 3.1(a,b)) and badly acquired capacitive images (Figure 3.1(c,d)), respectively. The latter are considered bad formed due to an insufficient pressure applied during the acquisition (mostly on the one of Figure 3.1(d)) and the presence of artifacts due to a non proper cleaning of the device before the acquisition took place. Also in this figure, artifacts due to physiological factors are clearly visible, such as the black spots due to pores perspiration activity or differences in the gray level values due to different hydration (possibly not uniform as one can see in Figure 3.1(b)). Even such artifacts should be considered when judging the overall image quality, keeping in mind that the objective of the acquisition focuses primarily on the skin surface pattern and not in the difference of the gray levels. In order to capture the differences in well formed and badly acquired images, gray level co-occurrence matrices (GLCM) are computed, since they have proved excel-

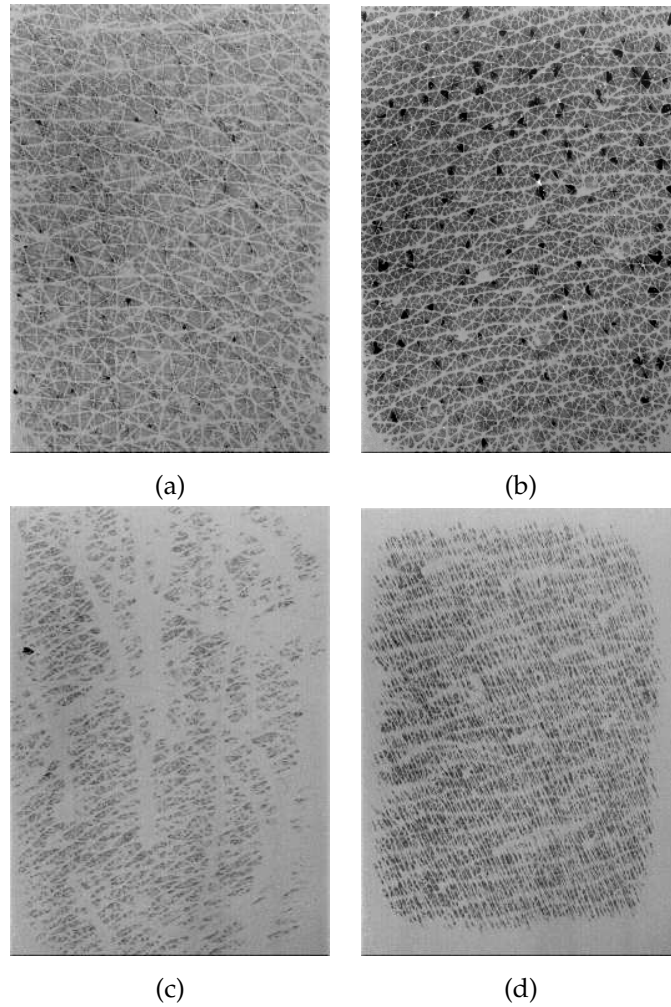


Figure 3.1: Good (a,b) and bad (c,d) skin capacitive images acquired on different subjects.

lent ability in texture characterization [34]. Recalling that a GLCM is built as:

$$C(i, j) = \sum_{p=1}^n \sum_{q=1}^m \begin{cases} 1, & \text{if } I(p, q) = i \wedge I(p + \delta x, q + \delta y) = j \\ 0, & \text{otherwise} \end{cases} \quad (3.1)$$

where $I(\cdot)$ is the input image of size $n \times m$ and $\delta x, \delta y$ represent the desired amount of horizontal and vertical displacement, respectively. Figure 3.2 shows the GLCM of the image shown in Figure 3.1(a).

From this matrix it is possible to extract several features based on second order statistics. In particular, the 8 chosen feature are: 'Energy', 'Contrast', 'Homogeneity', 'Correlation', 'Dissimilarity', 'Entropy', 'Centroid' and 'Sigma' (see [34] for details on this topic).

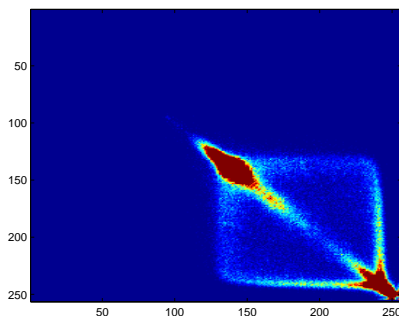


Figure 3.2: GLCM of the image of Figure 3.1(a).

3.3 SVM classifier

In order to implement the quality assessment algorithm a binary SVM classifier has been used to discriminate between good and bad images. Generally, given a training set of *instance-label* pairs $(\mathbf{x}_i, y_i), i = 1, \dots, n$ where $\mathbf{x}_i \in \mathbf{R}^n$ and y_i belongs either to \mathbf{R} or to the set $\{1, -1\}$ according to the case of a regression problem or a binary classifier, a learning algorithm is expressed by the following functional:

$$\arg \min_{f \in \mathcal{H}} \frac{1}{n} \sum_{i=1}^n V(y_i, f(x_i)) + \lambda \|f\|_{\mathcal{H}}^2 \quad (3.2)$$

The prediction function f belongs to the hypothesis space of functions \mathcal{H} . In Equation 3.2, V is the chosen loss function that drives the cost to pay in taking the predicted value $f(x)$ instead of the true value y while λ controls the Tikhonov regularization parameter, necessary to find a solution for these ill-posed problems in which the solution might be not unique or too data driven, and represents a trade-off between the Empirical Risk Minimization principle due to the first term and the penalty factor due to the second term [35, 36]. In statistical learning theory, different loss functions lead to different algorithms. The Hinge loss function $(1 - yf(\mathbf{x}))_+$ leads to the SVM algorithm.

In Equation 3.2, the so called kernel trick can be applied, which makes use of a Reproducing Kernel Hilbert Space (RKHS) \mathcal{H} . By using the reproducing kernel K one can evaluate the kernel $K(x, y)$ instead of having to choose the set of mapping functions ϕ_n and having to compute the dot product in feature space $\langle \phi(x), \phi(y) \rangle$, so that $K(x, y) = \langle \phi(x), \phi(y) \rangle$ (Mercer theorem). After having applied the Representer theorem which gives a solution of the form $f(x) = \sum_{i=1}^n c_i K(x, x_i)$ by the coefficients $c_i \in \mathbf{R}^n$, the minimization prob-

lem over the infinite space of functions \mathcal{H} can be reduced to a minimization problem over R^n , leading to:

$$\min_{f \in \mathcal{H}} \frac{1}{n} \sum_{i=1}^n (1 - y_i(Kc_i))_+ + \lambda \mathbf{c}^T K \mathbf{c} \quad (3.3)$$

where in this case, the kernel matrix representation has been used. Kernel could be very useful when dealing with not linearly separable datasets. By using an appropriate kernel, it is possible to jump from the input space (where feature values might not be linearly separable) to a (possibly) higher dimensional feature space in which the features could be linearly separable. When the input data set is not linearly separable, the SVM yields to the following minimization problem, in which (\mathbf{w}, b) identify the separating hyperplane:

$$\begin{aligned} \min_{\mathbf{w}, b} \quad & \frac{1}{2} \langle \mathbf{w} \cdot \mathbf{w} \rangle + C \sum_{i=1}^n \xi_i \\ \text{subject to} \quad & y_i(\langle \mathbf{w} \cdot \mathbf{x}_i \rangle + b) \geq 1 - \xi_i, \quad i = 1, \dots, n \\ & \xi_i \geq 0, \quad i = 1, \dots, n \end{aligned}$$

In this case, as λ play a trade-off as a penalty factor, C controls the number of misclassified points, determining the trade-off between the minimization of training error and the maximization of the margin. To allow for the non separability of classes (soft margin), a set of slack variables has been introduced into the problem. Whenever the slack variables ξ_i are non zero the corresponding points represent margin errors. Solving the dual problem, yields

$$\mathbf{w}^* = \sum_{i=1}^n \alpha_i y_i \mathbf{x}_i \quad (3.4)$$

The \mathbf{x}_i for which the corresponding coefficients $\alpha_i \neq 0$ are termed support vectors (SV) and represent the (possibly) few characteristic points from which an optimal separating hyperplane can be determined. By using the kernel trick, the dot product in \mathcal{H} can be replaced by using an appropriate kernel K , whose effect is to identify a non linear separating hyperplane in input space (associated with the linear separating hyperplane in feature space). In order to infer which class a new sample $\bar{\mathbf{x}}$ belongs to, for a binary classifier it is sufficient to evaluate the the decision function:

$$f(\bar{\mathbf{x}}) = \text{sign}\left(\sum_{i=1}^n y_i \alpha_i K(\bar{\mathbf{x}}, \mathbf{x}_i) + b\right) \quad (3.5)$$

A public available SVM classifier has been used to this purpose (libSVM, [37]).

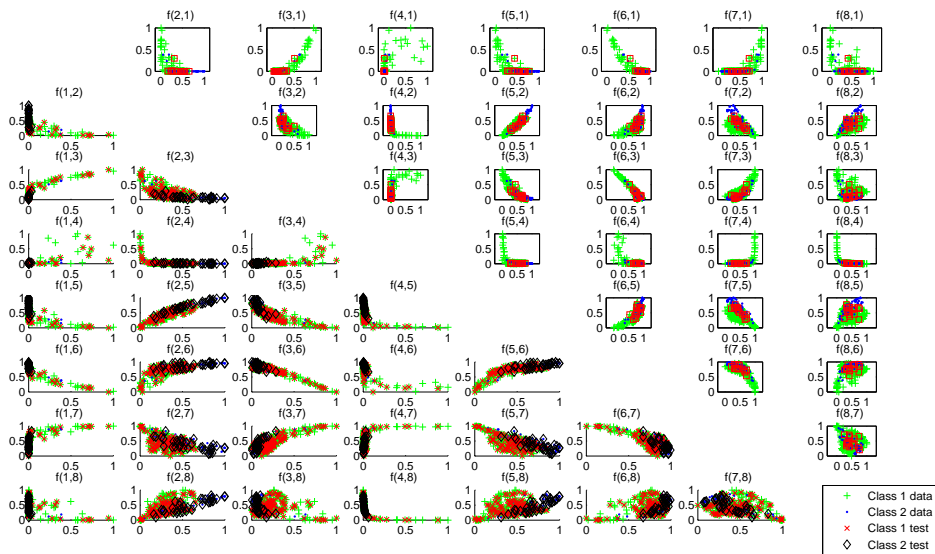


Figure 3.3: Haralick' features of the training and validation sets. Class 1 and 2 are bad and good quality images, respectively.

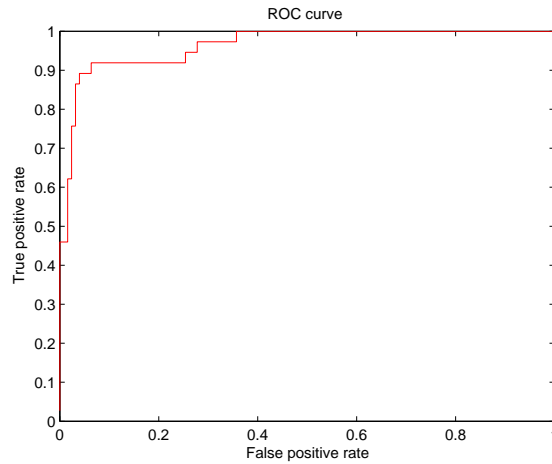
3.4 Experimental results

The whole dataset, composed of 327 samples has been partitioned into 2 different sets: a training set (S), a validation set (V). The set S and V have been generated by using a hold-out validation strategy, where the data set has been randomly split into two equally sized groups, one used for training and one used for validation.

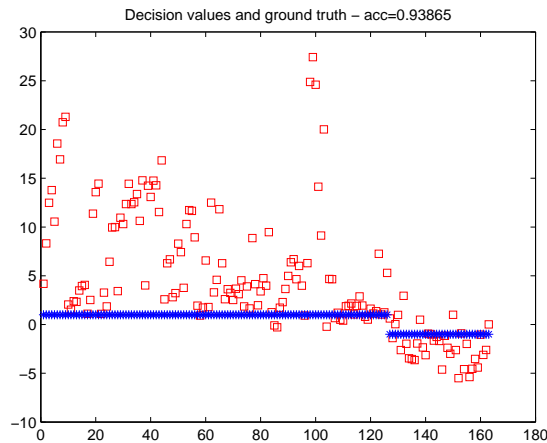
Prior to train the SVM classifier with S, a simple min / max scaling has been applied to the input data in order to compensate for large magnitude feature values that could mislead the learning stage. These normalization values have been subsequently applied to scale the data set V.

By a thorough analysis on the extracted feature, as depicted in Figure 3.3, where each pair of the Haralick' GLCM features are plotted one against the other, it has been possible to see that the set of feature $\{(x_i, y_i)\}, i = 1..n$ is not linearly separable in input space. Also, in this figure, the support vectors are depicted by red squares on the top-right side of the plot, while the bottom-left side shows the values of the training and validation sets for each pair of features. In Figure 3.3, class 1 and 2 refer to bad and good quality images, respectively.

Therefore, in order to have a better separating (soft margin) hyperplane in



(a)



(b)

Figure 3.4: ROC curve (a) and decision values (b) of the hold-out validation strategy.

feature space, a radial basis function kernel has been used (RBF, $K(x_i, x_j) = \exp(-\gamma \|x_i - x_j\|^2)$, $\gamma > 0$). In order to tune the parameters (C, γ) of the C-SVC, an iterative approach has been followed by changing one parameter at a time while leaving fixed the other one. Also, to speed up the computation of the tuning process, a hold-out validation strategy has been adopted. The best parameters found were $C = 12$ and $\gamma = 0.13$. The best classification results achieved in this stage are shown in Figure 3.4, where the Receiver Operative Characteristic (ROC) curve together with the decision values (red squares) and the ground truth labels (blue stars) are shown. Each good sample has been

labeled with a negative value (-1) while bad images are labeled as $+1$. Therefore, the classifier targets bad images with positive decision values. Here, a total of 18 support vectors yielded a correct classification rate of 93.86%.

To better capture the generalization property of how effective is the classification performance of the SVM classifier, a more complete validation strategy should be adopted. Since the number of samples is not so small, a k -fold cross validation is preferable rather than a leave-one-out strategy. To this end, a 5-fold cross validation has been performed, which tries to depict the real classification results in a more general way. Finally, on average, a 90.77% correct classification rate has been reached. The average values of sensitivity, which is the true positive rate (defined as $TP/(TP + FN)$), is 89.19% while specificity (the true negative rate $TN/(TN + FP)$) is 91.27%, where TP and TN are the true positive and negative samples (correctly classified by the SVM) and FP and FN are the false positive and negative samples (mismatched by the classifier), respectively.

3.5 Conclusion

This work describes a SVM based method for quality assessment of capacitive images used in dermatological applications. The experiments accomplished on a dataset of correctly and badly formed images acquired by a commercially available capacitive device show that features extracted from the GLCM of the capacitive images can correctly classify the two set with a ratio of about 90%.

Even though these results are of particular interest for our application, it is worth remarking that this work represents a preliminary study and a larger dataset should be considered to enforce the learning by example paradigm applied to this particular context.

Chapter 4

Algorithms

THIS CHAPTER deals with the algorithms involved in the analysis of the images acquired by the capacitive device. Features are devised to extract characteristic information out of the skin capacitive micro-relief. In particular, three main features will be presented: the first one is based on the area of the skin plateau that forms the typical pattern of the skin and is computed by using the watershed segmentation; the second one is related to a multiresolution analysis carried out using the wavelet transform, whereas the last feature is based on a photometric property related to the local contrast of the enhanced skin wrinkles.

4.1 Skin surface characterization

The output of the skin surface characterization should be a quantitative and objective measure regarding some properties of the skin surface micro-relief. In fact, it is well established in literature, that skin diseases or simply the ageing process changes the skin appearance and therefore topographic properties of the skin. These properties are necessarily related to the overall skin health status. [1] The main topographic structures of the skin are due to the intersecting primary and secondary lines forming the skin micro-relief. Therefore, lines and fine wrinkles (hereinafter, briefly *wrinkles*) and the corresponding plateau of skin tissue delimited by these lines (hereinafter, briefly *macro-cells*), form the typical pattern whose components represent our target objects we intend to analyze.

In order to characterize the skin topographic structures, an automatic algorithm should extract quantitative information, as much as possible descriptive

of the process of changes that can occur to the morphology of the skin. To give an example of the images and the main topography we are about to analyze, Figure 4.1 shows the capacitance image of skin samples referring to the arm of

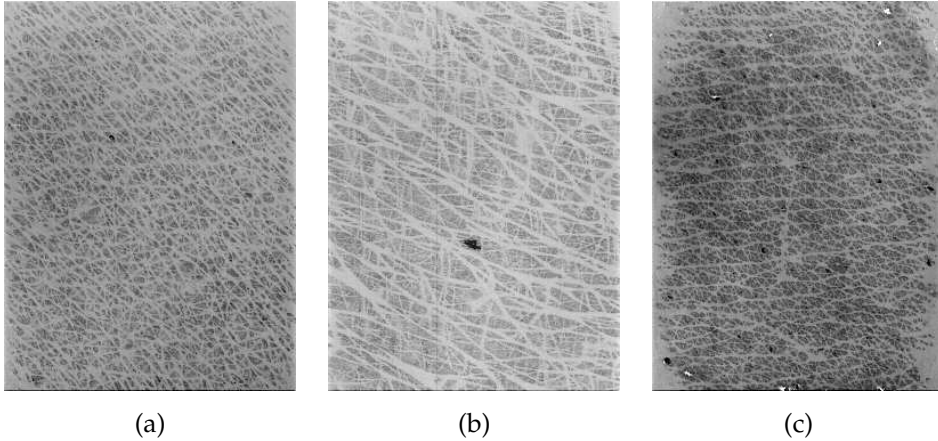


Figure 4.1: Capacitance images referring to a ROI's arm of a 72 y.o. female (a), a 94 y.o. female (b) and a 55 y.o. male (c).

a 72 y.o. female (a), a 94 y.o. female (b) and a 55 y.o. male (c): brighter pixels represent either wrinkles or possibly background (Figure 4.1(c), mainly at side borders) while the darker structures are made of macro-cells. However, when looking at the images of Figure 4.1, it could be very difficult to extract useful topographic information using those images “as is”.

Even though some countermeasures have been taken in order to tackle and resolve some issue of the capacitive sensor, like for example the shift in background intensity due to a non flat output response of the cell array (discussed in Section 2.3.1), other gray-level dependencies of the sensor output are still present. It is worth remarking that even though the capacitance image is insensitive to light changes, darker regions could be present due to either a higher hydration (Figure 4.1(a)) or the presence of pore sweat (Figure 4.1(b)). Figure 4.1(c) is an example containing both these artifacts. In particular, as already discussed in Chapter 2, the different gray level values produced by either different skin hydration or simply the sensor noise make a possible thresholding process very hard to be accomplished. Moreover, the different brightness between images could mislead any further processing stage.

For this reasons, performing a preprocessing step becomes essential.

As an outline, the main structure of the skin characterization algorithm is presented in Figure 4.2. Here, the capacitive skin sample acquired under specific conditions of pressure, as remarked in Chapter 2, is given as input to a

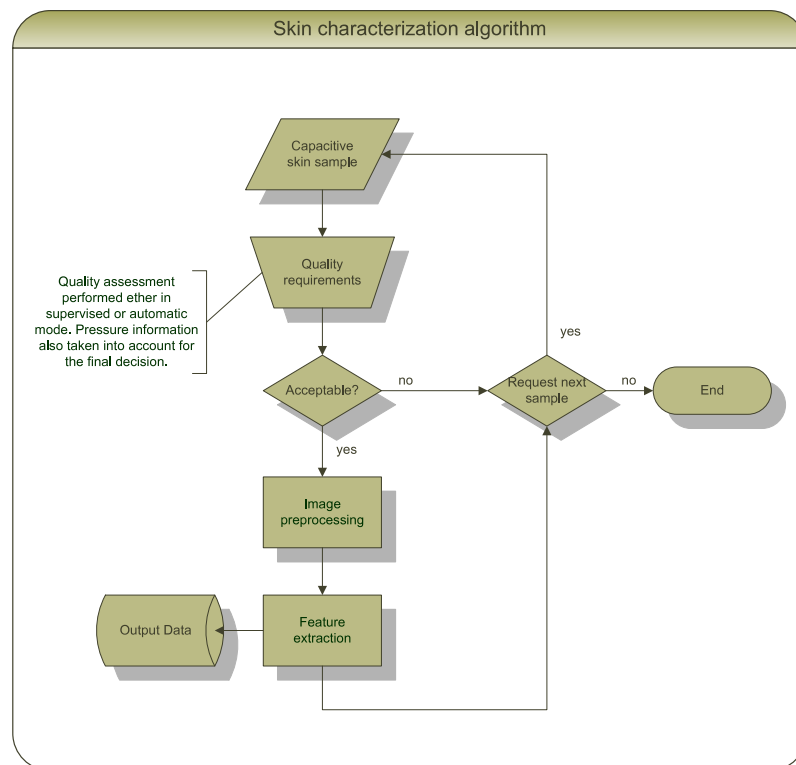


Figure 4.2: Outline of the skin characterization algorithm.

quality assessment test, performed either in automatic or supervised mode (see Chapter 3), and if the image is considered of acceptable quality, it will be given as input to a preprocessing stage in order to reduce or remove some of the artifacts which the capacitive sensor is affected. Only after the image has been preprocessed, features can be extracted and stored for later evaluation.

4.1.1 Preprocessing

The preprocessing step plays always a key role in every signal processing application even because the outcome of this stage affects all the subsequent stages. The type of preprocessing required should be set accordingly to the kind of target signal we intend to extract. In our case, since we are interested in extracting features related to topographic structures, the preprocessing step should leave these structures almost intact while removing or leveling other misleading information, such as noise or differences in the image gray levels, which could represent not only uninteresting phenomena in this setting, but also possible errors for the subsequent stages.

In Figure 4.3, the outline of the preprocessing performed on the input capac-

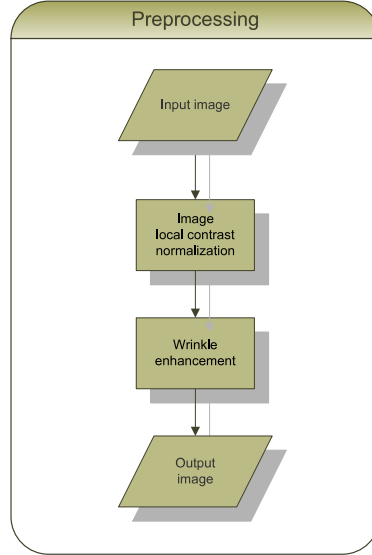


Figure 4.3: Outline of the preprocessing step.

itive image for the skin characterization algorithm is presented. The capacitive image under analysis is firstly normalized by a local contrast algorithm, and then a further enhancement of the wrinkles structures is performed.

Image normalization

As far as we have seen by looking at the dataset of images collected, changes in gray levels due to a difference in skin moisture content affect the contrast of the images, as depicted by gray level histograms of Figure 4.4. Here histograms of the images shown in Figure 4.1(a–c) reveals changes of the peaks' positions of gray levels due either to skin tissue macro-cells (darker values) or wrinkles (brighter values). Therefore, before segmenting each capacitive image, normalization of the local contrast [38,21] has been performed according to Equation 4.1. Here, by using a square sliding window of size w , the output normalized image $N(\cdot)$ is computed as:

$$N(x, y) = \sigma_0 \frac{I(x, y) - \mu_w}{\sigma_w} + \mu_0 \quad (4.1)$$

where $I(x, y)$ denote the gray-scale value at pixel position (x, y) in the original image, μ_w and σ_w the local mean and standard deviation of the square window

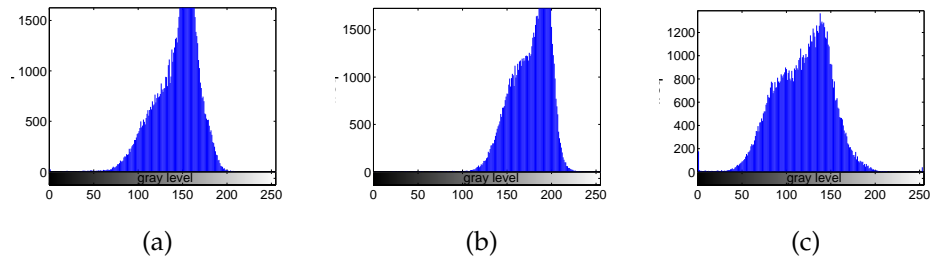


Figure 4.4: Gray level histograms (a–c) corresponding to the images of Figure 4.1(a–c).

centered on the current pixel position; μ_0 and σ_0 are the desired mean and variance values, respectively. This step reduces the effects of the sensor noise and of the grey level deformation due to both pressure differences and the effects of skin hydration. In particular, the larger the window size, the more preserved the structure (with respect to details); the higher the sigma value, the higher the contrast.

The images of Figure 4.5 show the effects of the normalization preprocessing with different choices of the parameters used.

If we set parameters according to $\sigma_0 = 100$ and $w = 20$, we can see in Figure 4.6(a–c) the effect of the normalization applied to the images of Figure 4.1(a–c) and the corresponding normalized gray level histograms (d–f). Here it is rather clear that images are much more comparable in terms of gray levels, whereas the size and shape of the skin topographic structures are left quite unaltered. Moreover, histograms show that structures are much more detectable, as revealed by the two distinct peaks at the left and right bounds of the plot corresponding to macro-cells and wrinkles structures, respectively.

Wrinkle enhancement

To achieve a better representation of the skin wrinkles, a further image processing step is required. From a topographic point of view, wrinkles can be approximately considered as continuous curves made of joining line segments having different spatial orientations. Therefore, a line enhancement algorithm is used to emphasize wrinkles. To this purpose, a set of bidimensional Gaussian filters having $N = 14$ different orientations has been used. The filter-bank

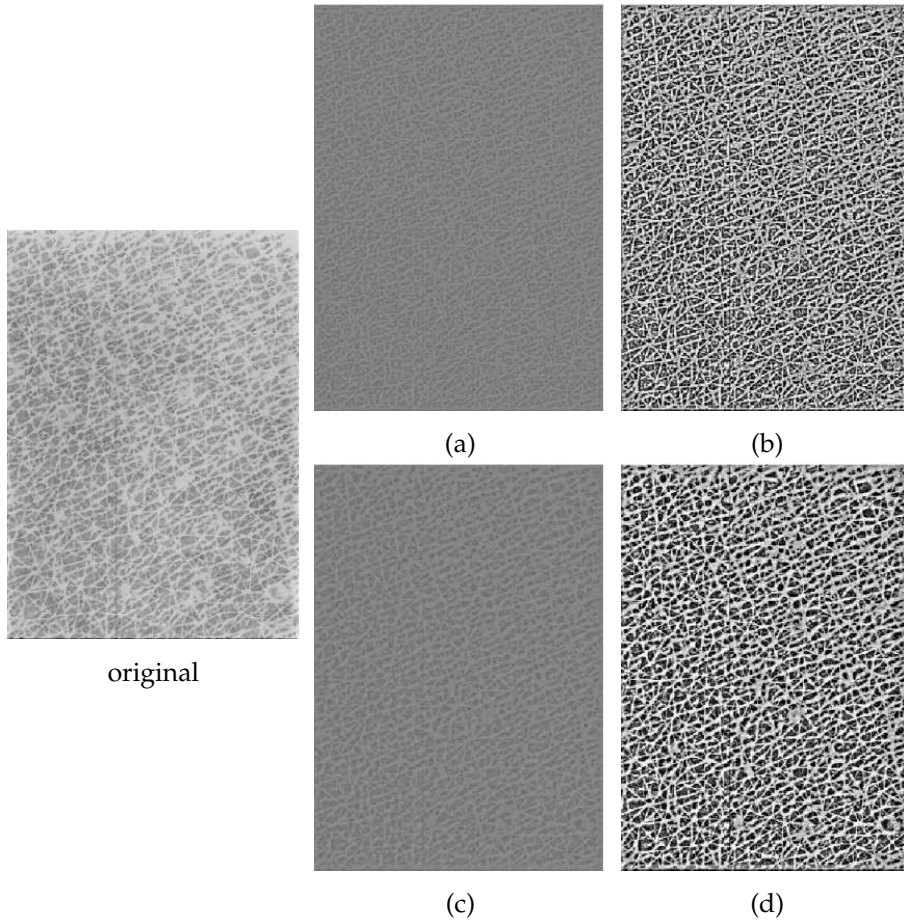


Figure 4.5: A comparison between an original sample and the same sample normalized by using different parameter values. The original image of a ROI's arm of a 64 y.o. female (on the left); $\sigma_0 = 10$ and $w = 10$ (a); $\sigma_0 = 100$ and $w = 10$ (b); $\sigma_0 = 10$ and $w = 20$ (c); $\sigma_0 = 100$ and $w = 20$ (d).

is given by:

$$\begin{aligned}
 G(x, y; \theta) &= \exp \left\{ -\frac{1}{2} \left[\frac{x_\theta^2}{\sigma_{x_\theta}^2} + \frac{y_\theta^2}{\sigma_{y_\theta}^2} \right] \right\} & (4.2) \\
 x_\theta &= x \sin \theta + y \cos \theta \\
 y_\theta &= x \cos \theta - y \sin \theta
 \end{aligned}$$

In Equation 4.2, the parameter θ is the wave orientation along the direction from the x -axis, while σ_{x_θ} and σ_{y_θ} are the space constant of the Gaussian envelope along the x_θ and y_θ axes respectively. After that the image has been filtered using the Gaussian filtering, N filtered images are generated, one for

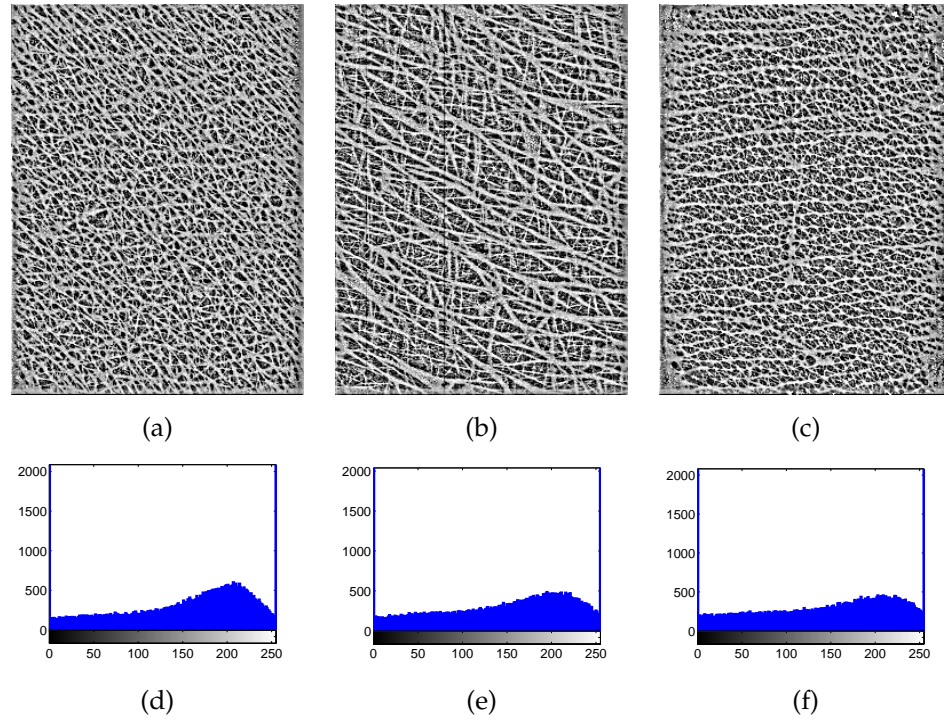


Figure 4.6: Effects of the applied normalization step ($\sigma_0 = 100$ and $w = 20$) to the capacitive arm' images of a 72 y.o. female (a), a 94 y.o. female (b) and a 55 y.o. male (c) and the corresponding gray level histograms (d–f).

each orientation θ which the filter has been applied for.

In Figure 4.7, the filtering convolution on the sample image of Figure 4.1(a) is shown for $\theta = 0$ deg (d), $\theta = 45$ deg (e) and $\theta = 90$ deg (f) together with each applied Gaussian kernel (a–c).

Each of these images retains all the wrinkles components (in pixels) along one specified direction θ . If we consider for each pixel of the resulting enhanced image E the maximum value each pixel has had in the overall set of orientation images O_θ , according to:

$$E(x, y) = \max \left\{ O_{\theta_i}(x, y), \theta_i = i \frac{\pi}{N}, i = 0..N - 1 \right\} \quad (4.3)$$

then we obtain a new representation where all wrinkles are emphasized. The image of Figure 4.8(b) shows the effect of the line-enhancement step performed on the ROI's arm of the 44 years old female.

On the other hand, the total amount O_θ of "wrinkle components" along a given direction θ could be also a relevant information providing us with a measure of wrinkles orientation. In particular, by arranging the O_θ values in

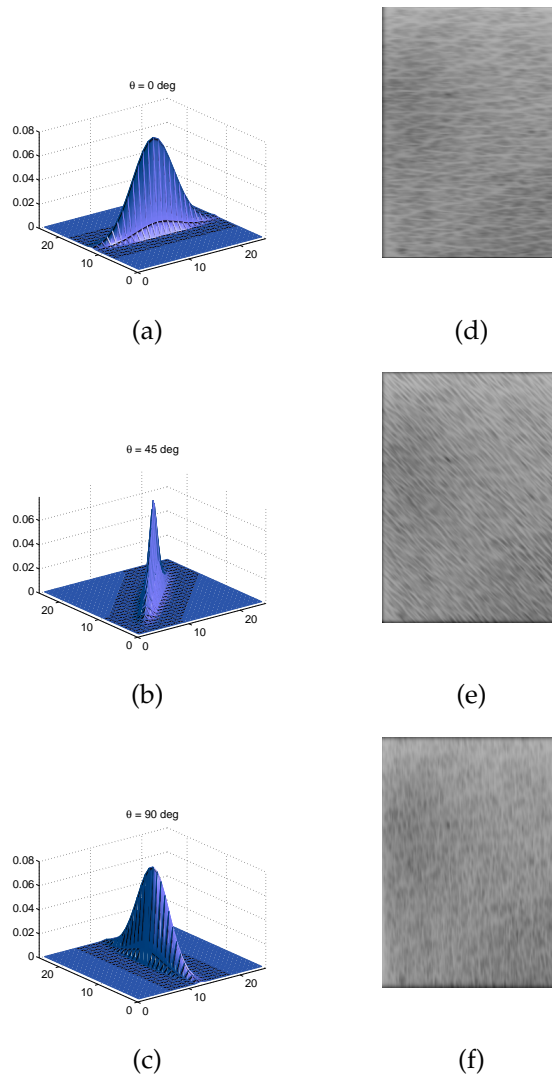


Figure 4.7: Gaussian kernel ($\sigma_x = 4$, $\sigma_y = .5$) for $\theta = 0$ deg (a), $\theta = 45$ deg (b) and $\theta = 90$ deg (c). The effect of the kernel convolution (d–f) on the image of Figure 4.1(a)

a polar plot for every direction θ considered, we could calculate how wrinkles are oriented in the image. Thus, by using the Gaussian filter-bank, we are able to obtain the whole wrinkle orientation chart (Figure 4.8(c)).

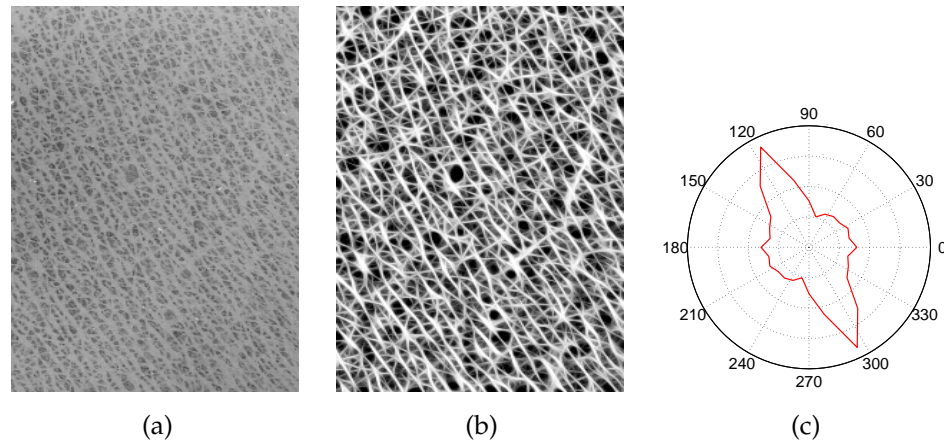


Figure 4.8: The original (a) and line-enhanced image (b) of a ROI's arm of a 44 y.o. female; in (c), the corresponding wrinkle orientation chart.

4.2 Feature extraction and testing methodology

The ultimate goal of the algorithm is to characterize the skin on the basis of surface topographic analysis. Firstly, it is worth noticing that there are many different types of skin, which could be roughly classified on the basis of their surface pattern. Moreover, these patterns could be related to changes occurred in skin surface topography due to the ageing process. Age-related features extracted from the skin capacitive images are therefore sensible to these changes and a validation through the skin ageing process could be particularly valuable. This is a necessary step in order to extract global texture features sensitive to changes in the skin micro-relief. In fact, the skin ageing effect is not only the primary cause of topographic changes in the skin surface micro-relief but also the most natural process of changes of skin properties. Having at our disposal features sensitive to these changes could represent a primary indication of the overall health status of the skin. Therefore, since the only available ground truth is represented by the true age of the subjects, correlation between values of features extracted from the skin capacitive images and the subject's age could represent a viable indicator in order to infer changes in the skin micro-relief. Besides, other environmental and physiological factors may affect the real skin ageing process occurred for each subject, depending, for example, on life habits, such as repetitive exposure to the sun. Changes in human skin due to sun ultraviolet light (photoaging) and changes occurring as a consequence of the passage of time (chronological or natural aging) are considered to be distinct phenomena. Even though the chosen body site presents a limited

exposure to environmental factors, most probably the only subject's age is not sufficient to obtain a perfect indication of the skin ageing effect. In other words, a perfect correlation between features values and chronological age should not be expected. However, a global trend in features values versus the subjects age could be a useful indication of changes occurred in the skin morphological properties due to ageing. A totally different approach could have been followed in order to obtain the ground truth; for example, by making use of skin biopsy, the true age of the skin could have been graded and quantified histologically, regardless of the subject's chronological age. However, even at experimental level, this approach would have been considered too invasive to be performed on a the whole number of subjects involved, thus being unfeasible. Nevertheless, skin ageing quantifications through skin biopsy are still grounded to subjective evaluations, therefore presenting high variability as reflected by final measurements being affected by errors. [39] Finally, the subject's age have been considered as the most valuable ground truth related to the skin ageing process.

After having looked at a large number of male and female arm' samples, a set of possibly age-related features have been identified and tested in order to see whether it is possible to find out an indication of the skin ageing effect. What soars from this earlier analysis is that as the age of subjects increases, the skin micro-relief arranges itself to form wrinkles and furrows in the oldest subjects. Moreover, also an increase of the area reserved to skin macro-cell structures in older subjects has been noticed, where the skin plateau area enlarges due to ageing. Therefore, to quantify the changes in the skin micro-relief due to the ageing process, wrinkles and the complementary structures represented by skin macro-cells are likely candidates to be studied. Besides, wrinkles are usually a matter of investigation since they show the most visible changes due to ageing. [26,30]

After the necessary preprocessing operations, features are devised to extract an overall indicator of changes in skin surface micro-relief out of the capacitive images. In particular, three characteristic features are extracted from the preprocessed input image, as outlined in the diagram of Figure 4.9.

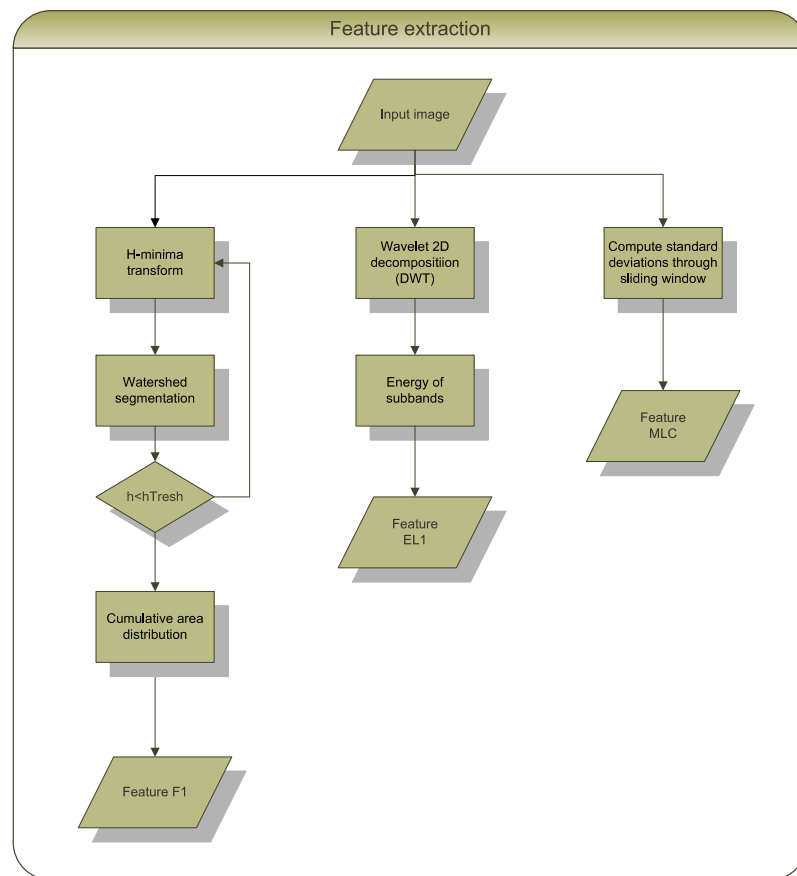


Figure 4.9: Outline of the features extraction algorithm.

4.2.1 Feature f_1 : the area of skin plateau

Watershed segmentation

Figures 4.10(a) and (b) are two extreme cases of capacitive images referring to a 1 year old baby and a 94 year old grandmother. Looking at the images in this figure, it might be difficult to realize that these are skin samples. These images look more like digital elevation maps (DEM) whereby the value of a pixel represents an elevation rather than luminance intensity: the darker the pixel, the higher the elevation of the terrain point. The basic assumption standing behind this feature is supported by the original definition of skin macro-cell. A skin macro-cell is a macro-structure composed of skin tissue, surrounded by main wrinkles and made of nearly “uniform” micro-wrinkles (with respect to the wrinkles surrounding the cell). With this view in mind, skin tissue macro-cells represent mountains and wrinkles represent valleys. Therefore, the problem of

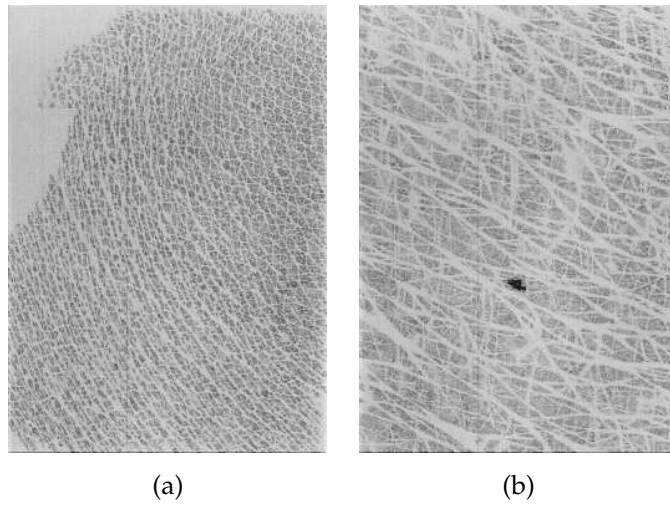


Figure 4.10: Two extreme cases of images referring to a 1 year old baby (a) and a 94 year old grandmother (b).

segmenting cells and wrinkles becomes the problem of segmenting mountains and valleys. To this end, such images can be segmented by using the methods usually employed in geomorphological applications. In particular, the watershed segmentation [40] has been used, which subdivides the image into catchment basins (locally homogeneous connected sets of pixels) surrounded by watershed lines (connected pixels exhibiting local maxima in gradient magnitude). To achieve a final segmentation, these lines are typically absorbed into their respective adjacent catchment basins. Therefore, at the end of the segmentation process, wrinkles are watershed lines and cells are catchment basins (see Figure 4.11(a-b), where each watershed line is displayed in red and superimposed on the original image).

In Figure 4.11(c-d), images of Figure 4.10(a-b) are segmented by the watershed algorithm, where each segmented macro-cell has been labeled and displayed with colors.

Granulometry analysis

Even though the watershed segmentation is a powerful tool, it is widely established that it is very sensitive to noise present in the input image, yielding oversegmented results. Oversegmentation occurs because every regional minimum, even if tiny and insignificant such as due to noise present in the image, forms its own catchment basin. As a matter of fact, skin capacitive images are very noisy when considering the size of the structures we intend to seg-

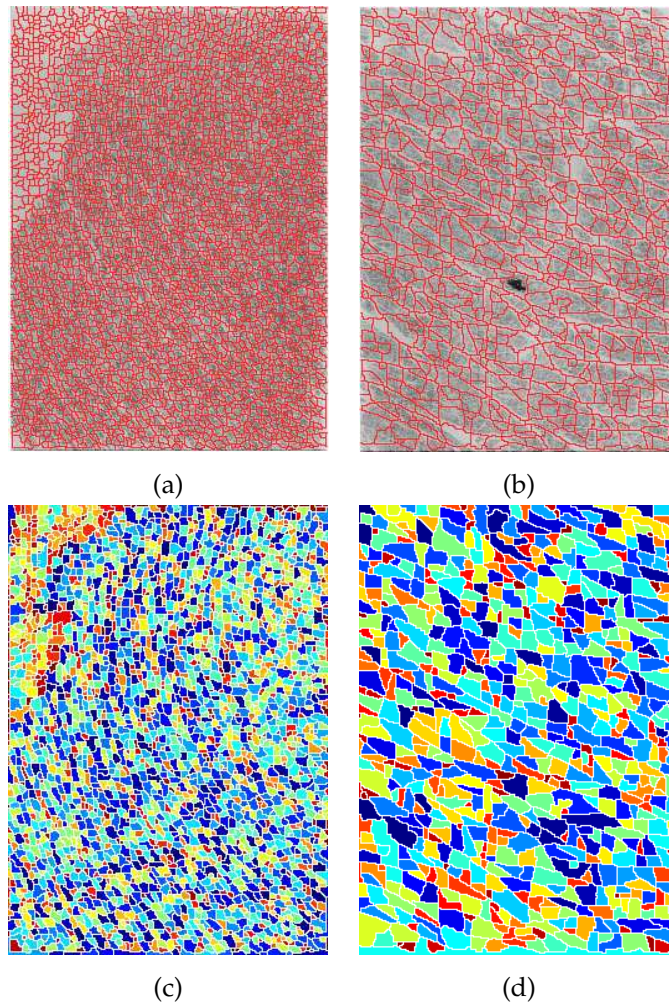


Figure 4.11: The segmented images of a 1 year old baby (a) and a 94 year old grandmother (b). In images (c) and (d) each segmented macro-cell has been labeled and displayed with different colors.

ment. In fact, a skin macro-cell could be even 10 pixels wide and within such a small region, local minima due to noise might split the macro-cell into several subregions, yielding oversegmentation. Even after the normalization and wrinkle-enhancement preprocessing, images presents a high gray level variability in the skin macro-cells. This poses the problem for a reliable segmentation. To overcome this behavior, in order not to generate oversegmented images, a granulometry analysis of the watershed segmentation carried out by using the *h-minima* transform [41] has been employed. The *h-minima* transform, suppress the local minima that are too shallow according to a height threshold

parameter. In particular, in order to achieve the best threshold parameter, the algorithm work in this way (see Figure 4.9): a granulometry analysis is carried out by varying the threshold value from the minimum to the maximum possible value, which is in the range $[0, 1]$ when considering a normalized image. To this end, the h-minima transform is applied to the normalized and enhanced image I , which is subsequently segmented by the watershed algorithm. The segmented image I_h is then binarized and used as a pattern to test the goodness of the segmentation result. A distribution of the absolute differences between the normalized, wrinkle-enhanced source image I and its h-minima segmented binarization I_h is computed according to:

$$\text{SAD}(h) = \sum_{(x,y) \in \{I_h=1\}} |I(x,y) - I_h(x,y)|, 0 \leq h \leq 1 \quad (4.4)$$

The Sum of Absolute Differences distribution (SAD) present a local minimum when the right value of the threshold parameter h is reached: that is, the sum of absolute difference between the h-minima segmented pattern and the input image is minimized. This value is the choice of h for the h-minima transform applied to the image before the final watershed segmentation.

The feature f_1

As a person gets on in years (see the images referring to the 94 y.o. female, Figure 4.10(b)), more and more wrinkles appear to get deeper and deeper, and wider! However, other wrinkles seem to keep roughly unchanged when compared to the deepest ones. This means that the region reserved to *each* macro-cell increases. Besides, the overall region reserved to cells as well as the overall amount of cells in a unit area (the device area) diminishes.

Since ageing enlarges macro-cells, the sum of the cells whose area is smaller than a given threshold could represent a significant feature. Figure 4.12(a-b) shows the histogram $H(x)$ of the macro-cells area related to the images of Figure 4.11 referring to the 1 year old baby and the 94 year old female. In Figure 4.12(c-d) the related cumulative histogram $H_C(x)$ (that represents the non-normalized cumulative distribution function) is calculated from the $H(x)$ of the two samples. The ordinate $H_C(x)$ represents the overall amount of cells whose area is lower than the respective abscissa value x and it represents the feature f_1 . Here, the abscissa M of the point P has been considered to be a relevant thresholding value. In fact, in P ($x = M$) the derivative of $H_C(x)$ is equal to one: that is, for $x < M$ the derivative is greater than one while for $x > M$ it is lower. Finally, $H_C(M)$ represents the feature f_1 which has been considered.

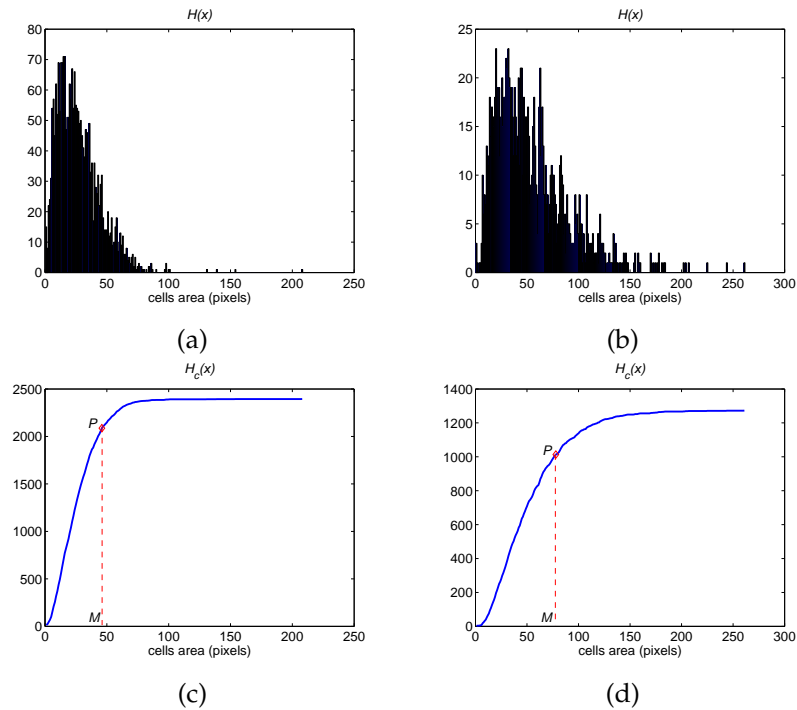


Figure 4.12: Cells area: histogram (a-b) and cumulative histogram (c-d) referring to the segmented images of Figure 4.11 of the 1 year old baby (a,c) and the 94 year old female (b,d).

4.2.2 Feature E_{L_1} : the wavelet analysis of skin wrinkles

Wavelet Analysis

When looking at Figure 4.10 you can see different kinds of wrinkles. While the main pattern is characterized by wide wrinkles, there are more thin wrinkles within the skin surface. Also, young subjects present more thin wrinkles than wide lines as opposed to elderly subjects where wider wrinkles are predominant. Since wrinkles appear as a network having different pattern size from coarse to fine resolution, the multiresolution analysis accomplished through the wavelet decomposition is a natural approach. In fact, the ability to analyze data at multiple resolutions together with wavelet transform being invertible (the source signal can be perfectly reconstructed from its wavelet coefficients) has brought the wavelet analysis to a successful application in many image processing tasks. Simply speaking, the wavelet transform acts as an adjustable zoom lens, resolving a signal at different scales, allowing to focus the analysis on different levels of detail.

The key idea is that any signal can be expressed as a linear combination of functions, generated starting from a prototype function (or mother wavelet) $\psi(t)$ by dilation and translation of a scaling function $\varphi(t)$. A similar approach is found in the Fourier series analysis, which provides the ability to localize a signal in frequency. However, it cannot localize a signal in time, since its basis functions are sinusoids of different frequency, which have an infinite amount of energy. On the other hand, the basis functions of a wavelet system, that is the scaling function $\varphi(t)$ and the wavelet function $\psi(t)$, have finite energy concentrated around a point. This property of the wavelet transform gives the ability to localize any $L^2(R)$ signal in both time and frequency.

The focus of attention is on the Discrete dyadic Wavelet Transform (DWT), which permits to transform a discrete signal into an approximation at a resolution 2^{-j} , where $j > 0$ represents the scale factor. In particular, the DWT model is applied to images which are nothing but 2D signals having finite energy. In the multiresolution scheme (due to *Mallat*) the signal decomposition is determined by successive filtering operations, where each scale is determined by upsampling and downsampling. [42] In practice, the multiresolution analysis is carried out using two channel filter-banks composed of a low-pass and a high-pass filter, G and H respectively (see Figure 4.13(a)). At each decomposition level, firstly the input image is convolved by rows with each filter and then downsampled. Secondly, the image achieved is convolved by columns with each filter and downsampled again. Thirdly, before starting to process subsequent level, the frequency of each filter is halved. By applying this procedure repeatedly it is possible to have a multiresolution representation of the input signal at different scales, each of them representing a level of decomposition. According to the steps described above, for each level of decomposition the original image can be transformed into four sub-images (or *sub-bands*), as one can see in Figure 4.13(b). Here, wavelet coefficients C_i are imaged for each sub-band i , namely:

- C_1 : LL sub-band (approximation) where both horizontal and vertical directions have low-frequencies (LL)
- C_2 : HL sub-band (horizontal details) where the horizontal direction has high-frequencies (H) and the vertical one has low-frequencies (L)
- C_3 : LH sub-band (vertical details) where the horizontal direction has low-frequencies (L) and the vertical one has high-frequencies (H)
- C_4 : HH sub-band (diagonal details) where both horizontal and vertical directions have high-frequencies (HH)

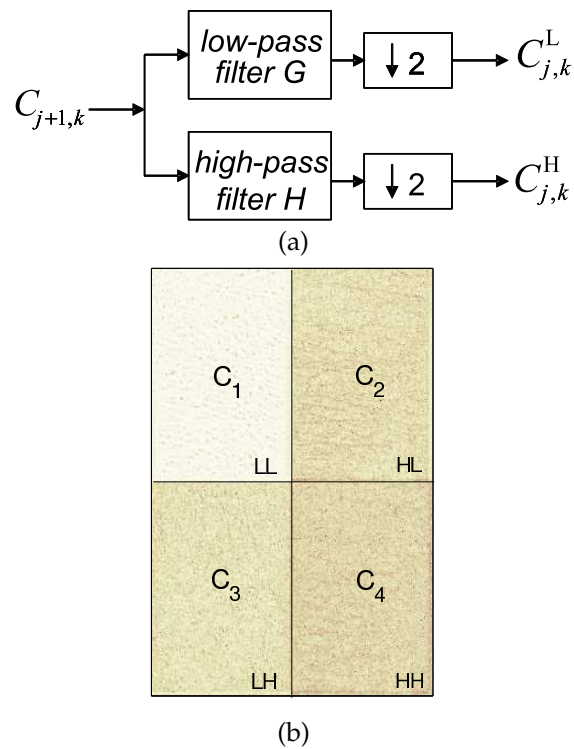


Figure 4.13: Schematic view of the DWT with one level of decomposition (a) applied to a capacitive image (b). Each sub-band's coefficients block has been labeled with C_i where i range from 1 to 4.

Thus, for L levels of decomposition, there are $3L + 1$ sub-bands, each of which contains the proper coefficients of the wavelet transform. Usually, sharp edge points (where the magnitude of the gradient of the image intensity has local maximum) are representative features of the image. Therefore, since the magnitude of the wavelet coefficients around position p is related to the size of the derivative of the signal at each scale j , larger coefficients are related to "features" in the source signal.

The feature E_{L_1}

After that the line enhanced image has been computed according to Eq. 4.3, the DWT with one level of decomposition is performed. The DWT coefficients present a higher value when a local maximum in the image gradient is reached, thus identifying a transition between wrinkles and skin surface. To give a measure of these transitions between low and high gray level pixels the normalized

energy E_{C_i} of coefficients C_i , as expressed by:

$$E_{C_i} = \frac{\sum_{(x,y) \in C_i} C_i^2(x,y)}{\text{card}(C_i)}, 1 \leq i \leq 4 \quad (4.5)$$

is usually employed, since it has proved to be very effective for texture characterization.

At last, the second feature extracted is the coefficients energy of level 1 of the DWT decomposition (hereinafter, briefly E_{L_1}), expressed by:

$$E_{L_1} = E_{C_2} + E_{C_3} + E_{C_4} \quad (4.6)$$

The energy of these coefficients gives a measure of how many transitions between wrinkles and skin surface tissue are present in the enhanced capacitive image.

4.2.3 Feature MLC: the local contrast of wrinkles

Photometry of wrinkles

As stated above, an increase in wrinkles width due to the ageing process has been noticed. Therefore, a proper measure of some of the photometric properties related to wrinkles in the skin sample retains the information we are looking for. Recalling that all the images are normalized by a local contrast function, a likely candidate feature could be the local contrast after that the wrinkles have been enhanced. Thus, what is measured is the wrinkles component of each image.

The feature MLC

Consequently, the extracted feature represents the Mean value of the Local Contrast (hereinafter, briefly MLC) and it is expressed by:

$$MLC = \frac{\sum_{(x,y) \in E} \sigma_w(x,y)}{\text{card}(E)} \quad (4.7)$$

where $\sigma_w(x,y)$ is the standard deviation value over a window of size w centered on the point $(x,y) \in E$, and $\text{card}(E)$ means the cardinality of the set of pixel in E . The window size w must be set according to the one chosen in the normalization step.

Even though capacitive images are not related to photons, since the image formation is not optical but due to a different physic phenomenon, we still

can treat the capacitance map as a sort of intensity based image where wrinkles that appear in brighter pixel values (firstly normalized by a local contrast correction and subsequently enhanced by the Gaussian filter-bank), can yield different contrast values according to their total amount and how wide they are. Therefore, this feature would give us a measure of the intensity of wrinkles present in the capacitive images by measuring the local contrast of the normalized and enhanced image: the wider the wrinkles are, the higher the feature value would be.

Chapter 5

Experimental results

IN THIS CHAPTER the algorithms previously devised for characterizing the skin are tested and evaluated. Recalling that the output of the skin surface characterization should be a quantitative and objective measure, all the image processing algorithms devised should be validated and compared with the only available “ground truth”: the age of the skin. Even though the information related to the skin ageing could be weak when considering the age of the subjects as an index of aged skin, because many other factors can alter the skin appearance, this value represents the only available quantitative characteristic to deal with when evaluating the goodness of the extracted features. Therefore, the available dataset of skin samples acquired during dermatological examination is used for the feature extraction. Each feature is analyzed in terms of correlation between feature values and chronological age of the subjects. A good correlation with the *skin ageing effect* means that the feature is able to capture *changes* in the skin topographic structures due to ageing. This represents a necessary test in order to evaluate changes induced by other physiological factor such as physical response to dermatologic or dermocosmetic treatments.

5.1 Feature sensitivity

Features extracted have been firstly analyzed in terms of sensitivity to translations, rotations and noise present in the capacitive images. Moreover, since contact pressure affect the outcome of the capacitive device sensor, pressure analysis have been also evaluated.

5.1.1 Invariance to translation, rotation and noise

In order to test translations invariance, several image samples have been cropped and disposed on a background image in different location according to the translation displacement considered. Results have shown that all the three features are invariant to translation.

The main problem arises from rotation and noise. Regarding the rotation invariance test, a cropped region of several samples has been subsequently analyzed by the algorithm after having rotated the whole image, whose angle has been varied in the range between 0 and 180 degrees with a step of 10 degrees. Images rotated in this way have been resampled by a bilinear interpolation.

Figure 5.6, shows the results of variations of the displacement of each feature value with respect to the zero degree (no rotation performed) as long as the angle of rotation increases.

For the feature f_1 , in figure (a) the variability with respect to the initial absolute value is between about -7% and 8% . Mean range variability computed on several samples has shown that f_1 varies of about 12.7% around the zero degree initial values. The coefficient of variation (CV), which measures the variability by computing the standard deviation over the mean of all the samples' values, is 7.56% on average.

The feature E_{L_1} also show relevant variability with respect to rotations. Averaged values show absolute variability of 6.7% and CV is about 5% on average. The feature that show limited dependency to angle of rotation is the MLC , which presents, on average, only 3.4% range variability and a CV of about 2% on the samples considered.

As far as the noise invariance is concerned, a zero-mean white Gaussian noise has been added to images before being analyzed by the algorithm. The Additive White Gaussian Noise (AWGN) test results for one sample are shown in Figure 5.7. Here, the plots show the results of variations of each feature value at increasing values of Gaussian white noise variance. Variability is computed as the difference (in percent) respect to the zero-variance (no noise added). All the features present variability due to the noise added: however, in this case, none of them had a monotonic increasing displacement as long as noise increased. Contrary to what one can imagine, especially for the wavelet energy-based feature, the effect of noise on the skin topographic structures of the capacitive images seems to have a non monotonic behavior. However, this could depends on the different processing carried out during the normalization and Gaussian filter banks applications, as well as segmentation and wavelet de-

composition stages. Moreover, white noise is spread randomly on the skin structures and no correlation between spatial distribution and skin topography exists.

For the feature f_1 , in figure (a) the variability with respect to the zero degree absolute value is between about -5% and 15% , showing high sensitivity of the watershed segmentation due to noise, even if normalization preprocessing has limited the effect of the noise added. This is comprehensible since the more the noise added, the different are the watershed lines and catchment basins identified during the segmentation according to the more local minima added.

Also feature E_{L_1} show relevant variability with respect to noisy images. In this case, an increase of the feature value is even up to 20% in Figure 5.7(b). Here, wavelet decomposition is very sensitive to noise due to the more gray level gradients added.

Noise added show limited effect on the evaluation of the *MLC* feature, which presents only 3% maximum variability in Figure 5.7(c). On average, the *MLC* feature has reported only 2.61% range variability due to noise on the whole sample dataset, and CV of about 2% .

These tests suggest that feature *MLC* should respond better to variation of the alignment of the device on the sampling body site, with respect to the other two features, having limited impact on variability due to both noise, always present in the device sensor output, and orientation of the capacitive images.

5.1.2 Pressure Analysis

As already pointed out in Section 2.3, image gray level values are affected by the pressure applied. Therefore we must also take into account how the features extracted vary as long as the pressure changes during the sample acquisition. In Figure 5.8, the features f_1 , E_{L_1} and *MLC* are plotted against the pressure applied during the acquisition of one sample. Among the images acquired in each sequence, only samples falling in the “saturated” zone at the right of the plots have been taken into account, where the derivative of the measured feature rapidly decreases. As already pointed out in Section 2.3, the acceptable range of contact pressure during the sample’s acquisition is between $25 \times 10^{-3} N/mm^2$ and $20 \times 10^{-2} N/mm^2$, where the skin is imaged correctly. Outside this range, either no complete skin structures are imaged (insufficient pressure) or distortion in the skin structures becomes predominant (high pressure values). Therefore, as expected, in this range the variation of the features with respect to pressure changes are relatively small compared to pressure values outside the range.

5.2 Skin ageing evaluation

The available dataset, firstly composed of more than 320 samples, has been subsequently analyzed in terms of quality of the acquired capacitive images. As already discussed in Chapter 3, most of the images acquired by non trained personnel have been subsequently judged of poor quality by an expert. Namely, the number of images of acceptable quality were only 77. Later on, other images have been acquired under the supervision of trained personnel. Finally, 90 good samples have been considered for the algorithm testing stage.

In Figure 5.1, the age distribution of the testing dataset is presented. Though

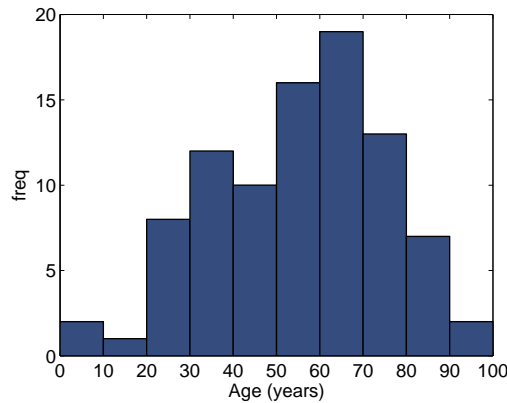


Figure 5.1: Distribution of the samples acquired according to subjects' chronological age.

the total number of samples is limited, this distribution resembles a normal distribution (even if skewed to the right), as it is not so easy to find very young and elderly volunteers.

As regards the parameters of the normalization stage, $\mu_0 = 128$ (mean value between 0 and 255), $w = 30$ and $\sigma_0 = 200$ have been identified as suitable values.

Regarding the parameter values related to the filtering operations necessary for the wrinkle-enhancement stage, extended experiments have been accomplished in order to find out the best parameter setting, by varying the parameters one at a time. This thorough inquiry has provided some guidelines to fix heuristically a proper parameter setting for Equation 4.2:

- a high value for σ_{x_θ} allows the filter to enhance thin wrinkles. On the other hand, a too high value may produce artificial wrinkle-like structures. For the skin samples considered, small values ranging from 0.5 to

1 could fit best. In the experiments $\sigma_{x_\theta} = 0.5$ have been chosen;

- the higher σ_{y_θ} , the longer the wrinkles detected. However, a too high value could yield the filter to join together short wrinkles close to each other. On the other hand, if σ_{y_θ} is too small a long wrinkles might not be detected. The experiments accomplished reveal that small values ranging from 2 to 5 could answer our purposes. In the experiments, it has been chosen $\sigma_{y_\theta} = 4$.

5.2.1 Feature f_1

To characterize the skin surface, a first starting point has been by measuring the area covered by clusters of skin tissue, called macro-cells. The first feature conceived soars from the cumulative area distribution of the skin macro-cells' area. The most frequent values measured for a macro-cell area range from about 13 pixels ($32 \times 10^{-3} mm^2$) for a 1 years old baby to 51 pixels ($127 \times 10^{-3} mm^2$) for a 94 years old grandmother. In Figure 5.2(a), the value of f_1 is plotted versus subjects' chronological age together with mean and standard deviation of each age group (ranging from 0-9, 10-19, 20-29, 30-39, etc.) and the regression line. As far as the graphical output is concerned, data shown in this plot are normalized between 0 and 100.

The high correlation between feature f_1 and chronological age is evident and surprising as well.

Figure 5.2(b) show the result of the feature f_1 after the first two age groups have been removed. This is due because in the 0-19 range only three samples were available, and they might not be statistically significant. Even in this plot, the negative correlation is quite good, being the correlation coefficient $r = -0.83$. That is, the amount of macro-cells whose area stands below the threshold M (dynamically chosen) diminishes as the chronological age increases.

5.2.2 Feature E_{L_1}

The line enhanced image obtained by Gaussian convolutions along different directions could reveal several aspects of the skin wrinkles. In particular, when using a multi-resolution approach such as the wavelet decomposition yielded by Dyadic discrete Wavelet Transform (briefly DWT), interesting details may come into view. In fact, the DWT coefficients present a higher value when a local maximum in the image gradient is reached, thus identifying a transition between wrinkles and skin surface in the normalized and line-enhanced image.

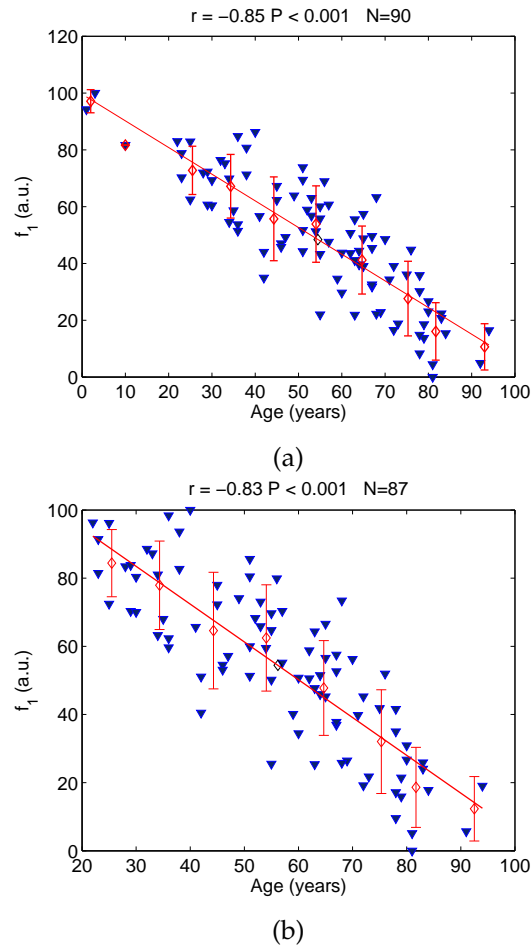


Figure 5.2: Feature f_1 versus chronological age on the whole test dataset (a). In (b) the first two age groups have been removed.

Recalling that despite sharing common properties, each wavelet transform leads to a unique decomposition of the signal depending on which mother wavelet has been selected, the choice of the mother wavelet used for the DWT decomposition has been found empirically. Finally, the Symlet wavelet with 8 vanishing moments (sym8) has been used, which is a nearly symmetric orthogonal wavelet with compact support and it owns better localization properties for the images considered in the experiments.

In Figure 5.3, the feature E_{L_1} is plotted against the subjects chronological age, where E_{L_1} data have been normalized between 0 and 100 for displaying purposes. Also, mean and standard deviation of each age group and the regression line are shown. In Figure 5.3(b) the first two age groups have been removed due to the fact that in this range few samples were available. How-

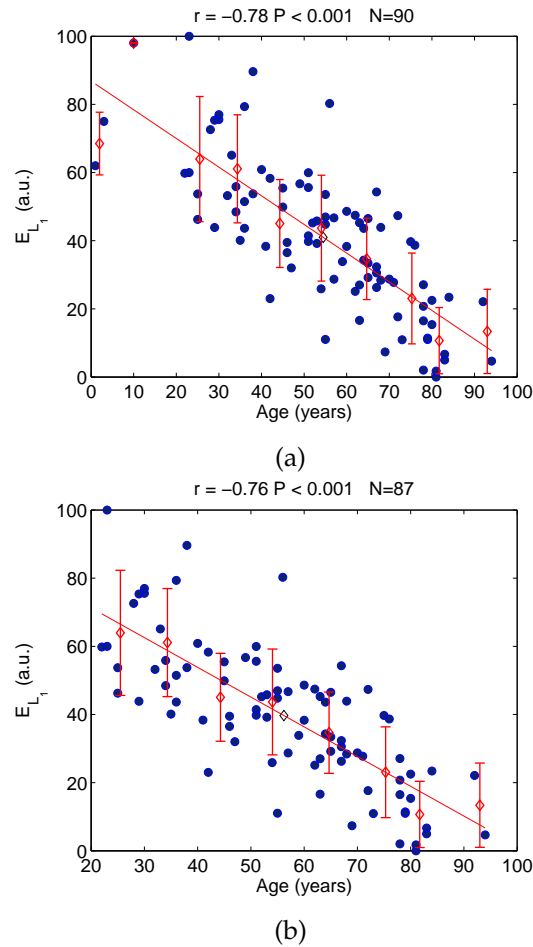


Figure 5.3: Feature E_{L_1} plotted versus subjects chronological age on the whole test dataset (a). In (b) the first two age groups have been removed.

ever, also the E_{L_1} feature present a good correlation with the skin ageing effect ($r = -0.76$). Moreover, if we exclude also the last age group where only two elderly subjects are present, the centroid of the class are monotonic descendant, giving an indication of the global skin ageing process of changes occurred in the skin structures.

5.2.3 Feature *MLC*

In Fig. 5.4 the value of *MLC* is plotted versus subjects' chronological age. Also, mean and standard deviation of each age group together with the regression line are shown. As far as the graphical output is concerned, data shown in this plot are normalized between 0 and 100. As for the other features, the first

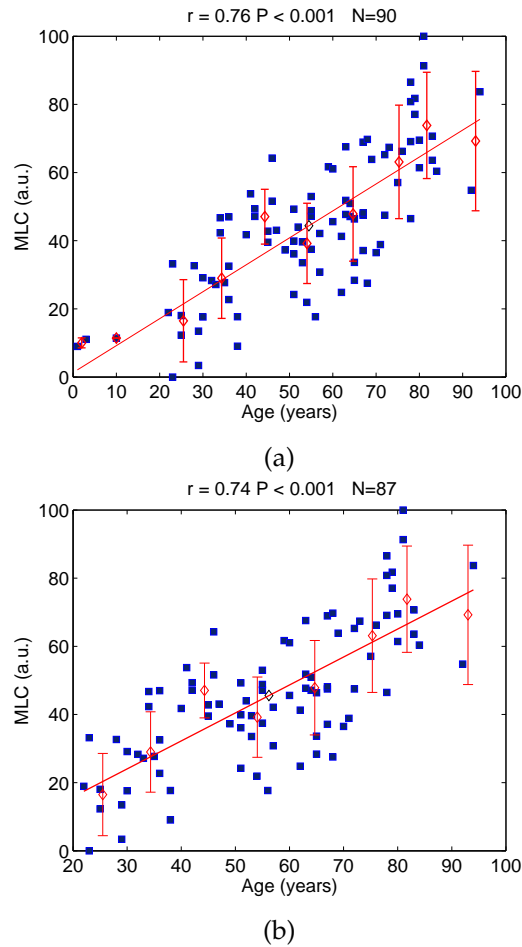


Figure 5.4: Feature *MLC* versus subjects' chronological age on the whole test dataset (a). In (b) the first two age groups have been removed.

two age groups have been removed due to the fact that in this range few samples were available (Figure 5.4(b)). Here, the *MLC* feature present a positive correlation with the subjects' age, being the correlation coefficient $r = 0.74$.

5.2.4 Discussion

For all the features devised, even though a non-linear correlation with the subjects age may exist, it has been tentatively calculated the correlation coefficient based on the assumption that the relationship is linear. The presented features all show a good correlation with the chronological age of the subjects involved in the test. Due to limited number of available samples in the first two classes (age ranges from 0-9 and 10-19), where only three subjects are present, results

have been presented also without these classes, with the intent to have more reliable statistics.

For the feature f_1 the correlation coefficient reduces from $r = -0.85$ to $r = -0.83$. In any case, the strong relationship between area of the watershed segmented macro-cells and subjects' age, confirm the first assumption that, in a general view, there is a strong tendency the area reserved to a skin macro-cell would enlarge due to ageing.

Also, the correlation between subjects age and E_{L_1} is quite good ($r=-0.76$, $p < 0.001$). Recalling what stated in Section 4.2, E_{L_1} gives a measure regarding the amount of transitions between wrinkles and skin tissue existing in the image. As a consequence, since the value of the feature E_{L_1} decreases with age, the total number of thin wrinkles in younger subjects appears to be greater than the ones of elderly subjects. Conversely, the latter presents fewer thin wrinkles and possibly many wrinkles of wider area.

A close correlation ($r=0.74$, $p < 0.001$) is found also between the MLC values, which is sensible to the total amount of wrinkles in the capacitive images, and the chronological age of the subjects. On the other hand, MLC gives a measure of how wide are the wrinkles. Therefore, the increasing of the MLC values as long as subjects go on in years, confirms that elderly subjects presents few thin wrinkles and many wider wrinkles, according to the results found for the feature E_{L_1} .

Moreover, the *MLC* feature has shown to be limitedly affected by noise and rotation of the device under the skin region of acquisition. Among the other features, it should be preferred in terms of reliability of the measurements achieved.

As far as the skin ageing evaluation is concerned, results show that a perfect correlation between these features and the chronological age is unfeasible. Nevertheless, we have not to forget that what we have is the ground truth (that is, the chronological age) while what we measure is the age of the skin. The subjects belong to a caucasian white "healthy" population, so most of the times these values presumably coincide. However, as already pointed out in Section 4.2, skin ageing depends not only by the chronological age of the subjects but also by other environmental factors. Therefore, even if it has been assumed that the ventral forearm region should present limited effects of these environmental factors, changes in the real age of the skin might depend from subject to subject. This is reflected by some subject' feature values not in the "right position". Therefore, rather than being a generic evaluation of the age of the subjects, these features give an indication of the global effect of changes

caused by the skin ageing process.

Other works have been reported in literature dealing with different devices: in [27], for example, results have been achieved by means of an ultrasound scanner. Here, authors measure in vivo subepidermal low-echogenic band (SLEB) grade of the skin forearm and find some correlation with the age of the subject. Their study involved 138 samples but the correlation coefficient is lower ($r = 0.72$) than the ones presented here. Other results reported in [26], using an optical device based on a CCD, have been achieved by correlating the width of forearm skin wrinkles to the subjects chronological age. Upon a number of 101 samples, they achieved a correlation coefficient of $r = 0.88$ which is substantially comparable with the results shown in this work. In the end, these results are substantially comparable to state-of-the-art results found in literature.

However, the results presented here have been achieved by using original features and mostly important, through a low cost system. What must be pointed out here, is that they could be of a great importance in dermatologic and dermocosmetic fields, since they allow the characterization of the skin surface by a routine approach, without the need of complex and high cost systems.

5.3 Repeatability of measures

Among the different features extracted and validated with the skin ageing effect the most promising feature, both for its ability to capture the skin status as well as its effective stability over time and limited variability due to noise and rotation is the *MLC* feature. To assess an accurate reliability analysis of the *MLC* feature, different capacitive images of the same subject taken in different periods of time have been analyzed. Table 5.1, shows a summary of the Coefficient of Variation (CV), defined as the ratio of the standard deviation over the mean of the measured *MLC* feature, calculated for the body sites considered during the acquisition of the samples in different days. In each day of acquisition the session accounts for 3 subsequent sequences of sample, each for every body site considered, taken one next to the other. After having performed a pressure analysis, a total of 768 samples were considered in this study. The samples come from 7 different body site (front cheek, lateral cheek, central forehead, periocular eye, perioral lips, ventral forearm, volar hand) of a 27 year old female.

The fairly low intra-day results of the CVs (for example in the front and lateral cheek and in the central forehead body sites) compared to the total body

Body site	Day 1	Day 2	Day 3	Day 4	Day 5	All samples
front cheek	0.90%	1.59%	0.55%	1.11%	1.55%	2.28%
lateral cheek	1.13%	1.29%	1.97%	0.38%	2.64%	2.52%
central forehead	0.97%	0.65%	1.68%	1.03%	1.34%	1.59%
periocular eye	-	-	0.87%	1.03%	-	0.95%
perioral lips	-	-	3.46%	3.97%	0.76%	3.23%
ventral forearm	-	-	0.33%	0.40%	0.56%	0.56%
volar hand	-	-	1.50%	1.10%	1.49%	1.44%

Table 5.1: Coefficient of variation for the 7 body sites considered during the acquisition of the samples in different days.

site's CV are possibly due to the fact that environmental (temperature and humidity) and physiological (moisture level) factors could affect the MLC feature, especially during the acquisition of samples in different days. During the experimental acquisition it has been tried to minimize these factors by controlling the temperature and by preventing the application of any sort of hydrating cream by the subject before the acquisition. In any case, forcing to take complete ownership of these variables is beyond the scope of this work and would lean towards limited experimental settings, far from a real context of possible application of the method. Despite these unwanted contributions due to both environmental and physiological factors, the measured CV variability is still quite low. The higher values correspond to the perioral lips body site. Here the sensor is unable to achieve good enough sequences of capacitive images, since, from a morphological point of view, it is a non planar site and the contact between the sensor and the skin alter in an inevitably manner the sensed area surface. Only on Day 5 it has been possible to achieve good sequences.

Figure 5.5 shows the CV of all the samples considered for each body site. Here, on the y-axis we have the CV, which is a measure of variability of the feature for all the measured value referring to the same body site. As far as we can see, there is a limited variability and, among all the sites involved, the minimum variability is achieved in the upper ventral forearm, thus supporting in terms of reliability the results of skin ageing evaluation previously achieved.

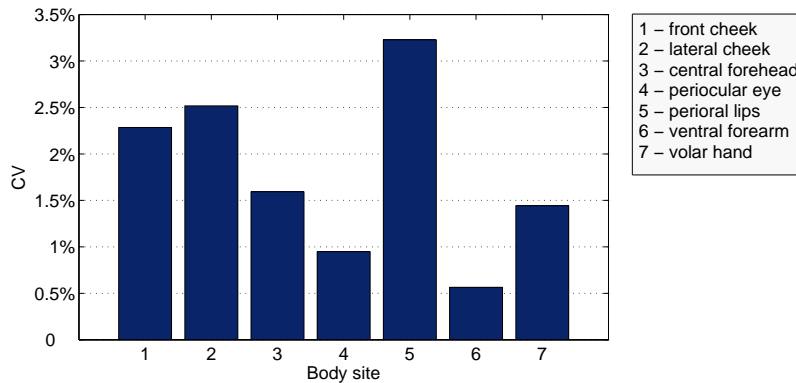


Figure 5.5: *MLC* repeatability on different body site of a subject. A total of 768 images, taken from sequences in different period of times spanning a week, have been analyzed.

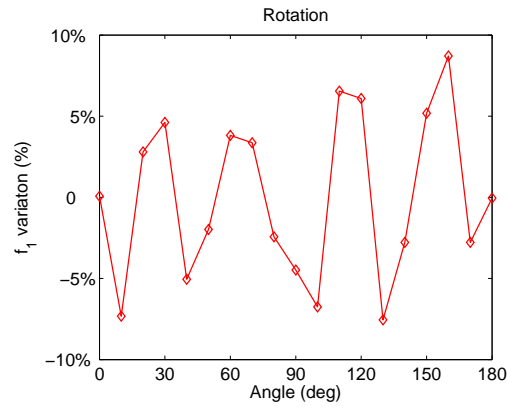
5.4 Computational complexity

The computational issue related to the algorithms presented for the skin surface characterization have been mainly due to the watershed granulometry (which is quite processor consuming, since repetitive segmentations are needed in order to find the correct h-minima threshold value), Gaussian line enhancement (which needs convolutions of 14 different kernels) and wavelet analysis. The elapsed time required by the algorithm to process one image is less than 3 seconds on an Athlon 1.6 GHz CPU, thus being negligible as far as our needs are concerned. Besides, no optimization tasks have been accomplished yet to speed up the process, since for the time being there are no needs for that. However, at first sight, it seems possible to lower the whole clock time to process 4-5 images per second. As for memory requirements, one image is 92 KB in size and few temporary data structures are necessary in the algorithms. Therefore, the RAM occupancy for the complete algorithm keeps widely below 1 MB.

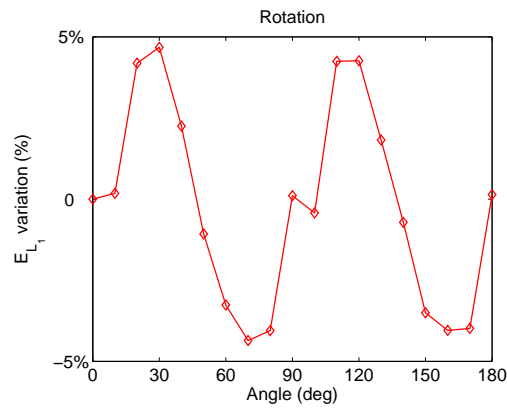
5.5 Conclusion

This chapter has been focused on the detailed analysis of the features devised for the skin surface characterization. The features, analyzed on the skin ageing effect that changes the skin topographic structures recognized by the algorithms, which are wrinkles and its complements that forms the skin macro-cells, have shown a good correlation with the age of the subjects. These results, substantially comparable to state-of-the-art results found in literature

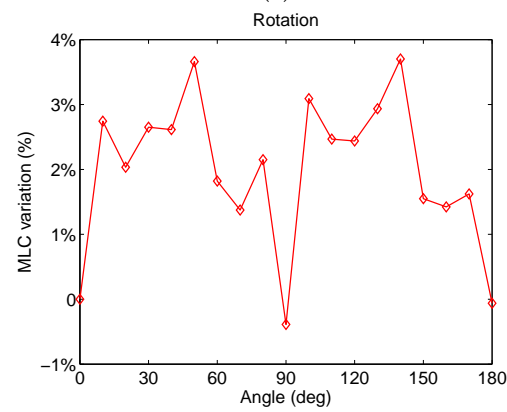
due to other authors [26, 27], have been achieved by using original features and mostly important, through a low cost system. Therefore, they could be of a great importance in dermatologic and dermocosmetic fields, since they allow the characterization of the skin surface by a routine approach, without the need of complex and high cost systems. A reliability analysis performed on the three devised features has revealed some issue mostly related to rotation and noise, which are the two main possible source of uncontrollable errors. In fact, neither the orientation by which the sensor is placed on the skin under test, nor the noise that always affect the sensor output, can be completely under control. However, among the features presented, the *MLC* showed a limited variability due to rotation and noise. Therefore, this feature should be a likely candidate for the evaluation of subjects' response to dermatologic or dermocosmetic treatments, in which repetitive acquisition and evaluation of the skin during the course of the treatment are needed. In particular, a repeatability analysis of the *MLC* feature, carried out by acquiring the the same skin region of different body sites during several days, has shown that the variability expressed by the coefficient of variation (CV) is quite limited, and also present a minimum in the ventral forearm region, that is the chosen body site to test the skin ageing effect. This support even more the the previously achieved results of skin ageing evaluation in terms of reliability.



(a)

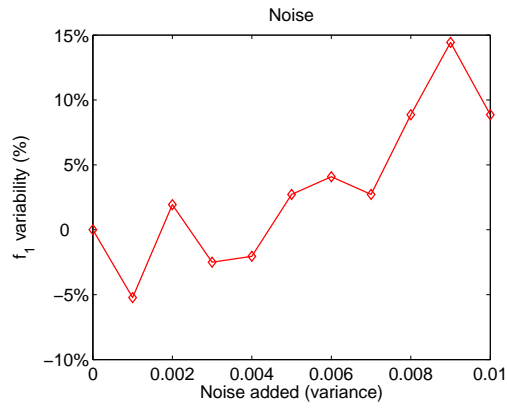


(b)

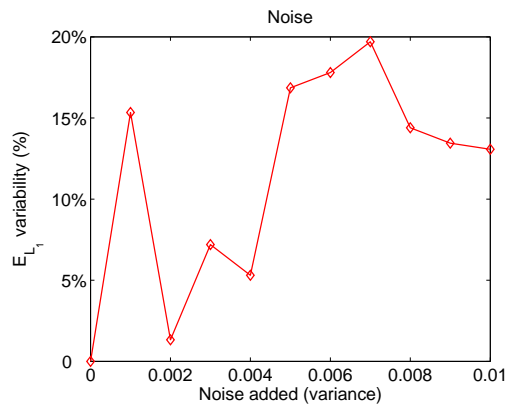


(c)

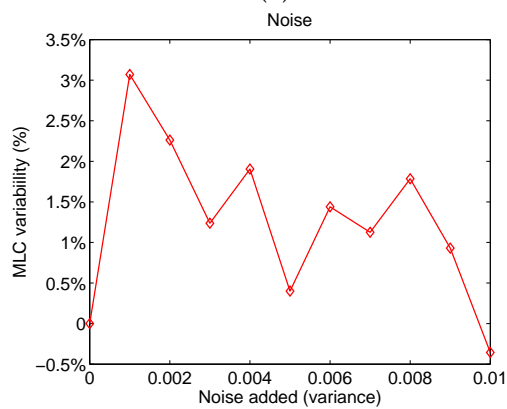
Figure 5.6: Features f_1 (a), E_{L_1} (b) and MLC (c) versus angle of rotation (in degrees) applied to one sample.



(a)

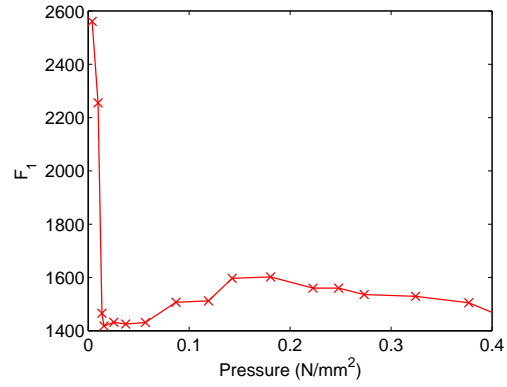


(b)

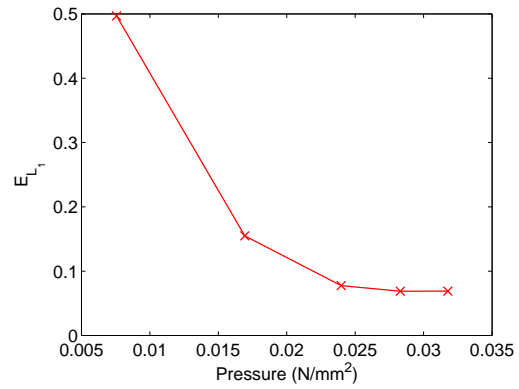


(c)

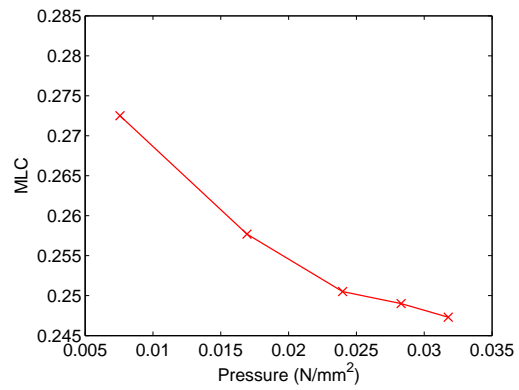
Figure 5.7: Features f_1 (a), E_{L_1} (b) and MLC (c) versus added white Gaussian noise at increasing values of variance applied to one sample.



(a)



(b)



(c)

Figure 5.8: Features f_1 (a), E_{L_1} (b) and MLC (c) versus pressure applied during the acquisition of one sample.

Chapter 6

Applications: follow-up studies

AFTER having validated the proposed features, an application of the method in follow-up studies is presented. The ability to detect changes in the skin topographic structures is used to keep track of the possible improvements due to a dermatologic treatment. To this end, a simple hydrating treatment has been evaluated by using the MLC feature. Preliminary results and considerations about the proposed method will be discussed in this chapter.

6.1 Introduction

The ultimate scope of this research work is to build a low-cost system able to characterize the skin surface changes. Therefore, a natural application to test the devised system is represented by a follow-up analysis during a dermatologic treatment.

In this context, the scope of the analysis is to measure the short term changes in the skin surface topographic structures of different subjects treated with a hydrating cream. In particular, the interest is focused in evaluating how much the micro-wrinkles shrink as a consequence of the hydrating treatment. To this purpose, the capacitive device allows to acquire high resolution capacitive images of the skin surface. However, due to the limited area covered by the device, subsequent acquisition might not be referring to the exact same skin region. In order to perform reliable measurements, so to minimize variation of the measures due to displacements of the acquired skin images, it is necessary to compare two images of *exactly* the same body part taken before and after the

treatment. The reduced dimension of the sensor cannot ensure an operator to be able to acquire, only *by sight* and after a long time has been elapsed between two acquisitions, an area large enough to allow reliable measures.

However, a larger skin area can be achieved by registering together different overlapping images through a mosaicing method developed on purpose. In such a way, images acquired before and after treatment can be compared effectively.

6.2 The method

Follow up studies generally use photographic images of the treated skin surface to assess differences according to a scoring or a scaling system. Despite the variety of published scoring and scaling systems for assessing skin topographic changes, none of them has been established as being the standard [43]. Moreover, most of the methods either rely on visual evaluation or achieve quantitative evaluation by means of histologic examinations using biopsy, which are *invasive* techniques. [39]

Many devices are known to measure the skin topographic age-related changes, but only few of them are portable and suitable for a routine approach.

This work aims at investigating the feasibility of the proposed skin characterization system to be employed routinely in follow-up analysis.

Firstly, the same skin area under treatment is imaged by the capacitive device in two subsequent acquisitions (before and after treatment). Among the skin macro structures, here the focus is on wrinkles of the skin micro-relief, whose effect is to wide as age increases. Skin micro-relief is composed of many micro-wrinkles and few larger wrinkles. The effect of the hydrating treatment is mostly visible for micro-wrinkles, which are relaxed and sometimes disappear. Even larger wrinkles could present beneficial short term effect due to an increase of the moisture content of the stratum corneum.

Secondly, for each acquisition a measure related to the overall amount of wrinkles, given by the feature MLC, is recorded. The difference between the two measures (given in percent) represents the output of the treatment evaluation, which should indicate an improvement or a worsening of the skin condition according to its sign.

Since MLC increases with age, the differential analysis should indicate a reduction in its value due to the effect of the hydrating treatment.

Therefore, the differential analysis relies on the MLC feature, which is measured before and after the cream application, thus allowing to quantify the

effect of the hydrating treatment.

Image acquisition

In order to perform a reliable differential analysis we need to perform two subsequent acquisition, at different time (hours or days as well), sharing (part of) the same body site. Since for obvious reasons employing artificial markers is not feasible, we could only rely on human guidance and natural markers. However, this approach would produce a shared area smaller than the sensor surface and it would be not enough to perform the measurements reliably. To overcome this problem, the approach is to acquire more images for each acquisition session covering a large area and then building a global mosaic. Having defined the *acquisition session* as the whole set of acquisition shots performed on a same skin region in a reduced amount of time (less than one minute), this permits to consider skin physiological properties as being constants and to cover, at sight, an area large enough to perform a reliable differential measure. Pressure is recorded during the acquisition of the sequence of capacitive images, in order to take into account only those falling in the right range of allowed pressure.

Automatic Image Mosaic

As stated before, image mosaicing is necessary to obtain a large capacitive area common to different acquisition session, starting from single acquisition images. Moreover, image registration is necessary anyway in order to compare data obtained from different acquisitions.

Image registration is the process of aligning two images of the same scene by warping the first one (input image) into the second one (base image), so to have the same coordinate system. Mosaicing is the process of creating a larger view by applying image registration to multiple overlapping images.

Image mosaicing and therefore image registration, presents large number of applications in digital imaging. [44] In the past decades many solutions have been presented for merging images from aerial views, video sequences and documents. In the filed of medical imaging, image registration is a very active research field, where techniques have also to deal with nonrigid registration, due for example to the particular morphology or the elasticity of the human body.

Many approaches use *area-based* method: the structures of the images are searched via correlation metrics. For example, the very interesting method de-

scribed in [45] deals with histological skin images. The solution employs phase correlation coupled with normalized cross correlation for automatic alignment of histological images acquired through a digital camera. It estimates the amount of overlap between images by ensuring the sub-pixel accuracy with phase correlation. However, although it can deal with large displacements, it covers only translational displacements, by forcing the acquisition to exclude any rotation.

Another way to estimate the transformation between overlapping images, is to use a set of corresponding markers: firstly a set of interesting points from both the images are extracted and secondly, correspondences between these set of points are searched. In this case, the method is called *feature-based*.

Due to the fact that changes in skin structures may become predominant after treatment applications, together with the fact that the skin structures are very similar even in different position along the skin body site region considered, an area-based method would not be able to effectively estimate the transformation. Therefore, a feature-based method has been employed. As the feature point extractors, Harris [46] has been firstly chosen because it has proved to be the better among those considered, both in terms of simplicity and performances.

Nevertheless, since some capacitive images showed poor results on the application of the Harris corner extractor, also (Scale Invariant Feature Transform) SIFT [47] features have been evaluated. From a general point of view, SIFT performs better when elastic deformation of the skin surface are more marked as well as when we need to compare profilometric and capacitive images: in this latter case, the difference in scale between the two images due to the differences in capacitive and profilometric resolution is better captured by the SIFT features. However, in the general mosaicing algorithm, the Harris corner extractor has been used to register between capacitive images.

Since the skin is an elastic and deformable medium, the pressure applied manually by contact during acquisition yields elastic deformation of the skin. This, necessarily influences the complexity of the transformation model to choose. By relaxing the constraint of elastic deformation, an affine transformation model is preferable, which is a 6-parameter linear combination of translation, rotation and scaling. It permits different stretching along image rows and columns and it is the most general linear transformation. For a robust assessment of the affinity between the two images, the RANSAC [48] algorithm has been used, which simultaneously computes the affinity and rejects the outliers. Figure 6.1 shows two images of the upper ventral forearm region of a 25 y.o. male successfully registered and blended in the resulting mosaic image. As we can see

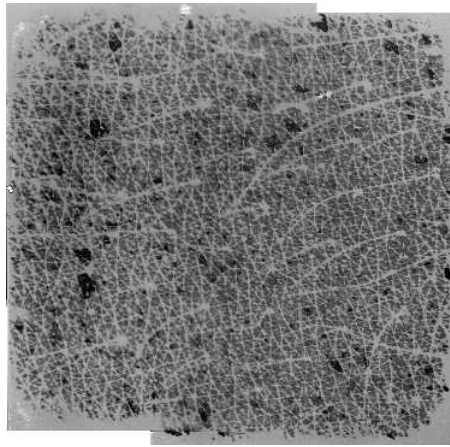


Figure 6.1: A mosaic of two skin images of a 25 y.o. male.

the stitching is seamless and the skin structure of both images is preserved. This is the simplest registration case involving two images. As for the registration of more than two images, an all-to-all registration is performed, which produces a graph with skin images at the nodes and the corresponding affinities. Computing the minimum spanning tree of the graph, leads to reduce the registration errors that may arise from concatenating affinities. The composition of the mosaic is finally realized by warping the whole image data set into the base image plane. Finally, a seamless mosaic is created by performing an alpha blending on the borders coupled with a vignetting removal process.

This permit to obtain two mosaics sharing a common area between two different acquisition sessions. Moreover, to extract measurements for the differential analysis, the two mosaic are further registered together in order to extract the same shared area, which is large enough to achieve reliable pre-treatment and post-treatment measures.

6.3 Experimental results

This preliminary work aims at quantify short term changes of the topographic skin structures of subjects belonging to two classes: under 30 y.o. and over 30 y.o. volunteers. In particular, 6 subjects will be analyzed, 3 belonging to the first class and other 3 belonging to the second class. The experiments are accomplished on the upper ventral forearm region, which is the least suffering from environmental exposure. The results attained strongly depend on life habits (e.g. usually, women use more beauty care products than men) and on

the physiological response of each subject to hydrating treatments. Choosing far classes allows to appreciate in a better way how ageing affects the skin elasticity. The first acquisition session is performed before applying any treatment. Further on, a hydrating cream is applied and after one hour the effects of the hydrating treatment become visible. Then the subsequent acquisition sessions is performed and extraction of the MLC values from the shared area attained by the two mosaics is computed. Figure 6.2 shows two images extracted from

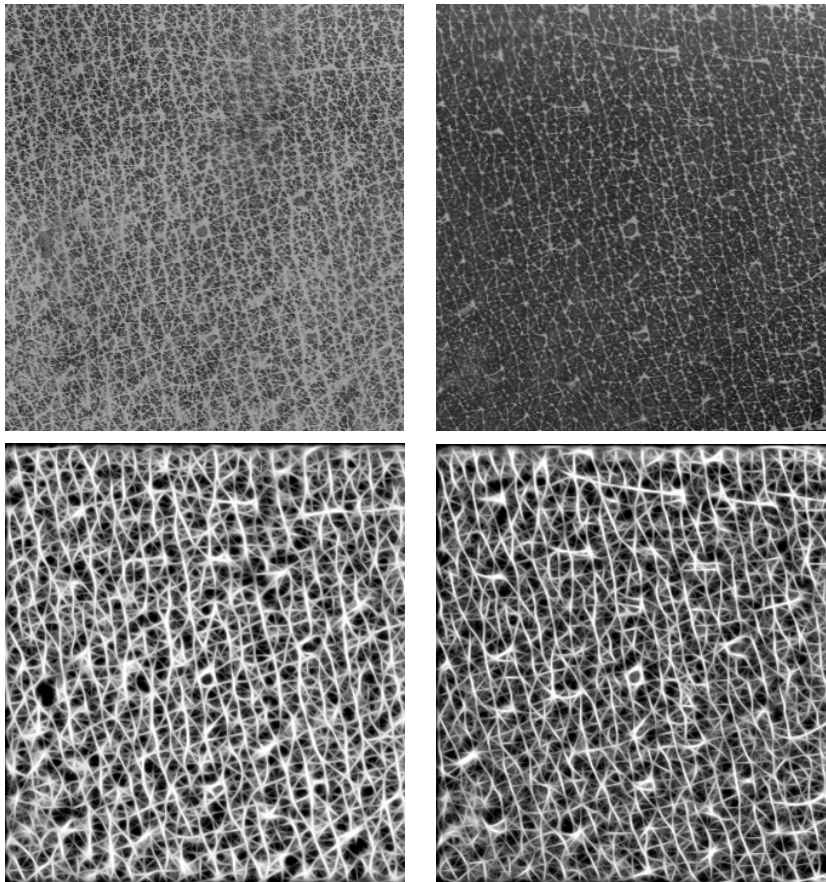


Figure 6.2: Shared area from two mosaics referring to a 22 y.o. female, before (left) and after (right) treatment. Bottom images are the result of the preprocessing stage where normalization and wrinkle enhancement have been applied.

the shared area of the two mosaics referring to a 22 y.o. female. On the left you can see how the skin appears before treatment, while on the right the skin has had a hydrating treatment.

Different gray levels are due to the physics of the device: right image appears far darker since the hydrating cream has added water content in the star-

tum corneum, which in turn is sensed by the capacitive sensor as a higher capacitance due to a rising of the dielectric permittivity (water dielectric constant is 80 times greater than air). Besides differences in image brightness, the effect of the cream application is that micro-reliefs shrank due to hydration and this phenomenon is appreciable by sight. This is even more evident when looking at the same images after the preprocessing is applied. The images at the bottom of Figure 6.2, show the same images after the normalization and wrinkle-enhancement preprocessing applied during the computation of the MLC feature. Here images are similar in terms of gray levels. What has changed are the wrinkle structures. After the cream application (figure on right), wrinkles appears far much thinner than before. In addition, we can measure it.

MLC values have been calculated before and after the hydrating treatment. For all samples the value of the MLC feature after treatment decreases, thus proving an overall improvement. Figure 6.3 shows the improvement for each

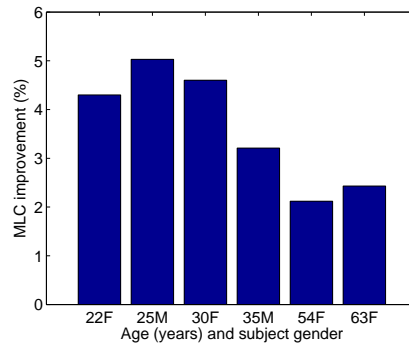


Figure 6.3: MLC improvement after the hydrating treatment for the three subjects.

subjects due to the hydrating treatment. As for the 22 y.o. female of Figure 6.2, the improvement has been measured in 4.3%. You can see that for younger subjects the reduction of the skin micro-wrinkles is more than twice with respect to the older subject. This is due to the skin of the young subjects being more elastic and reactive than the skin of older subjects. In Figure 6.4 you can see a common area extracted from two mosaics referring to the 54 y.o. subject, before (left) and after (right) hydrating treatment. The improvement is of 2.0%. Comparing this couple of images with the ones of Figure 6.2 it becomes evident how the younger subject shows a better response to the hydrating cream application. In regard to the improvement for the 25 y.o. male, it is of 5.0%, which is higher than the one of the 22 y.o. female. Probably, this is due to the overall skin hydration state of the female subject being better than the male

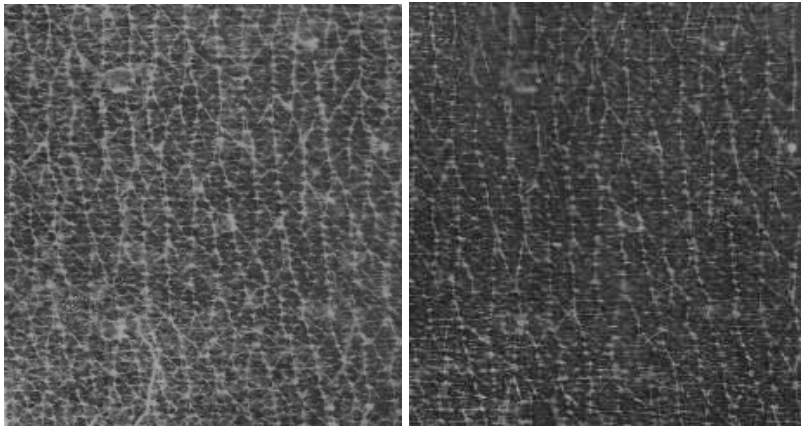


Figure 6.4: Shared area from two mosaics referring to a 54 y.o. female, before (left) and after (right) treatment.

one. In fact, the 22 y.o. woman often applies herself hydrating creams, thus reducing the margin for further improvements. At the opposite, this is the first time for the 25 y.o. male to apply himself a hydrating cream, and his skin owns a higher absorption potential.

In Figure 6.5 two images, referring to the 63 y.o. female arm, are extracted

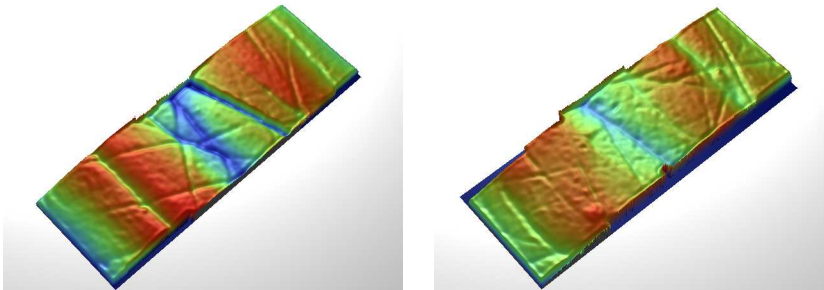


Figure 6.5: Profilometry analysis of the 63 y.o. female before (left) and after (right) treatment as evaluated by a skin surface replica. Images are magnified by a $20.58\times$ factor and measures $305 \times 875 \mu m$.

from the same area of skin surface replicas after the analysis by optical profilometry. The skin replicas have been created after the two acquisition sessions, before and after the application of the cream. Although these sample may not refer to the same exact area, due to differences in the alignment of the replica specimens under the profilometer, they refer to a very small region around the main wrinkle. In fact, the area covered by these images is $305 \times 875 \mu m$ in size and so quite limited. To give an idea of the actual size, the capacitive

images would cover the same region by only 6×17 pixels, approximately. Profilometric detailed images, taken at a magnification factor of 20.58, show the improvement of the cream application. In particular, the image on the right side of the figure, which refers to the state of the skin after the hydration treatment, shows how thin wrinkles have been almost disappeared comparing to the pre-treatment condition (left image). The main wrinkle (depicted at low height levels in blue colors), also showed a relevant reduction due to added moisturizing cream. This effect, however, would not last for much time, since it is just temporary. Once the hydrating effect is terminated, this wrinkle will return in its original shape. The profilometric analysis has shown a reduction in the mean surface roughness parameter (Ra) of about 4%. On the contrary, the improvement measured by MLC is about 2%. However, the capacitive images considered for the MLC evaluation are larger than this small area, where the wide wrinkle is predominant. Nevertheless, assessment of the relationship between surface roughness parameters and MLC feature is beyond the scope of these experiments.

However, comparison between these profilometric analysis, which represent the ground truth of the changes occurred in the skin micro-relief due to the cream application, and capacitive images, could better reveal the effectiveness of the method. In Figure 6.6 two magnified capacitive images are presented:

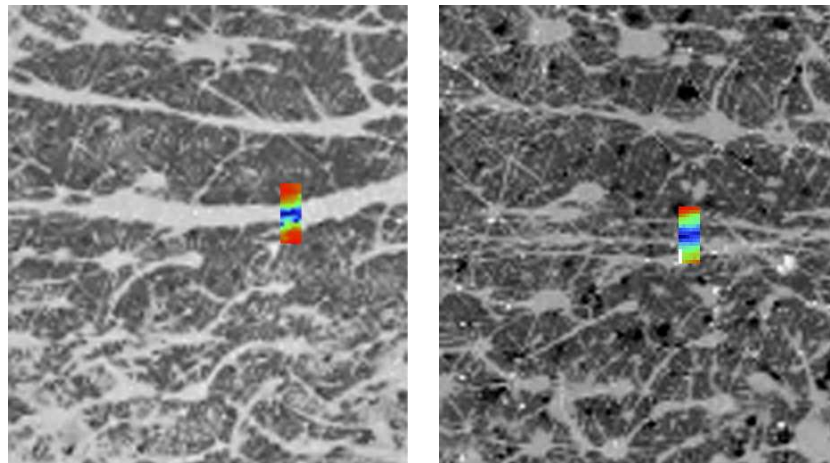


Figure 6.6: Details of magnified capacitive images referring to the images of the 63 y.o. female shown in Figure 6.5, before (left) and after (right) treatment. On the capacitive images, profilometric images have been stitched in order to better show where the profilometric analysis of the skin surface replica has been performed. Images are magnified by a $4\times$ factor and measures 5.6×6.45 mm.

before (left) and after (right) treatment. They refer to the images of the 63 y.o. female shown in Figure 6.5. Here, profilometric images have been stitched on the capacitive images, in order to better show where the profilometric analysis of the skin surface replica has been performed. Nevertheless, distortion of the skin surface are present, so that the registration has been very hard to be accomplished. The after-treatment capacitive image show a relevant improvement on the wide wrinkle, according to the profilometric analysis.

6.4 Conclusion

In this chapter, the feature MLC previously validated on the skin ageing effect, has been employed to *measure* changes of the skin topographic structures due to hydrating treatments. In order to reliably measure these changes from subsequent acquisitions of the skin body site region, a mosaicing method has been developed to register different images on the same coordinate system. This method, based on the matching of corner features extracted from the capacitive images, has been employed to build mosaics of the skin region under evaluation with the purpose of having a region larger than the limited device area. This allowed to extract a common area to be compared in the pre-treatment and post-treatment evaluation. The approach, even if carried out on a limited number of samples, showed the feasibility of the method to quantify changes of the skin surface due to hydrating treatments applied on the ventral forearm site. In fact, as expected, all the subjects show improvements on their skin condition after one hour from the hydrating cream application. The improvement was quantified (in percent) by the decreasing MLC value with respect to the pre-treatment condition. Also, a skin replica-based profilometry analysis has been carried out on the same area of one subject. Comparisons between capacitive skin images and profiometric images show congruent results. The experiments accomplished indicate that the developed skin characterization system is able to measure changes due to treatment in a follow-up setting. This method might be an interesting option to evaluate after treatments skin conditions in the dermocosmetics field.

It is worth remarking that this work represents the first attempt of measuring such a kind of changes by using a portable capacitive device. Future works should deal with a large number of sample by considering also replica-based profilometric analysis to better support the obtained results. Further on, the mosaicing method, although showed good results in almost every considered case, should be extended in order to preserve the finest details and to model the

skin elastic deformation due to the interaction between skin surface and acquisition device, which become more evident in the elderly subjects. Finally, more extensive case studies have to be carried out to address topological changes after dermatological treatments.

Chapter 7

Final Conclusion

THIS DISSERTATION has been focused on the presentation of a skin surface characterization system based on image analysis of the capacitive images acquired by the device. All the original results presented are summarized here.

The motivation that supported this research arise from current skin surface evaluation methods being primarily grounded to complex, non portable, and expensive devices. Although very accurate measurements can be achieved by using such instruments, these factors limit their applicability on a large scale.

Therefore, a new skin surface characterization system has been devised and evaluated. This portable and compact system, which relies on a capacitive sensing principle of acquisition, offer the possibility to imagine the skin surface in an unconventional manner. Capacitance map of the skin surface reveal all the main components of the skin surface topography: fine lines and wrinkles of the skin micro-relief. It is well established that skin surface analysis retains all the information regarding the overall skin condition, and moreover could be considered as a marker of individual health status.

Device pros and cons

The capacitive device used to imagine the skin surface suffers from physiological skin conditions as well as physics due to the acquisition principle. Images of a number of volunteers acquired on different body sites under disparate conditions have shown that gray levels do not depend only on 3D skin surface information and several drawbacks limit the applicability of this method.

Prior to devise any algorithm able to extract information out of the skin capacitive images, in order to attain better knowledge of the device, the system

has been evaluated and characterized.

In particular, after having calibrated the background to denoise the capacitive images through background subtraction, a profilometric analysis has been carried out. Accurate experiments have been accomplished by comparing the measures attained from capacitive images with the ground truth achieved by an optical profilometer. In particular, the same line extracted from corresponding points in capacitive and profilometric images has been profiled and analyzed.

A linear model has been devised according to the capacitive sensing principle of acquisition, in order to map the gray-level capacitive profile to a micrometric output. The model has been further integrated with spline interpolation in order to increase the capacitive profile resolution and to allow the comparison with the high-resolution profilometric data.

The capacitive device show a saturation effect in the depth characterization of the skin profile: this is due to a limited electric field that penetrates the skin tissue, limiting the appreciable depth of the real skin profile. Exploiting gradient-based spline interpolation of the sensed capacitive profile increases the ability to characterize skin wrinkles depths up to $50\mu m$. However, some of the skin wrinkles could be deeper than this value.

Since the system relies on a contact method when acquiring the skin surface, contact pressure plays a key role during the acquisition. In order to take into account contribution to the final skin output capacitive image due to pressure, a pressure sensor has been integrated into the characterization system. Experiments have shown that when pressure is lower than $25 \times 10^{-3} N/mm^2$ not all the skin structures are imaged, yielding incorrect profiles. Above this pressure threshold value, skin is imaged correctly up to about $20 \times 10^{-2} N/mm^2$. Further increasing in contact pressure yields distortions of the skin structures to become predominant. This upper limit, however, may depends from different body site and from person to person. Besides, by exploiting low-pressure information of the skin structures during the images sequence of acquisition, a reconstructed 3D profile has been recovered, limiting the distortion of the skin structures directly in contact with the device sensor.

Even though 3D depth profile characterization has revealed limitations of the capacitive device, measurements attained by considering information related only to planar structures have shown congruent numerical quantifications between profilometric and capacitive wrinkle analysis. In particular, the distance between two adjacent local minima of the profile, which represents the inter-wrinkle distance (*IWD*), has been measured and compared with pro-

filometric data. Good correlation between the two measurements system has been achieved. This proves the effectiveness and the reliability of the measures related to 2D skin topography attained from the capacitive device.

Collection of capacitive skin images

A database collection of skin capacitive and optical samples (mainly of the ventral forearm region) has been carried out together with a team of dermatologists. The choice to sample this forearm region is due to the fact that it presents limited exposure to environmental factors, as well as a better defined topography. A protocol of acquisition of the skin samples has been studied in order to minimize the source of possible errors and to limit issues related to the capacitive device. In a first stage, dermatologists were not sufficiently trained to deal with such unconventional kind of images. As a matter of fact, later evaluations of the images acquired revealed issue related to bad acquisitions: insufficient pressure, non proper cleaning of the device before the acquisition, are only few of the possible encountered drawbacks. Later acquisition were performed in a better way. However, the total dataset of more 320 samples have been reduced to only 90 available good quality samples.

In order to try to overcome bad acquisitions in the future, an automatic quality assessment method has been studied with the intent of discarding low quality images. A supervised classification has been performed on the set of available capacitive images by using a Support Vector Machine (SVM) classifier. The experiments accomplished on a dataset of correctly and badly formed images acquired by the capacitive device showed that features extracted from Gray Level Co-occurrence Matrix (GLCM) of the capacitive images can correctly classify the two set with a ratio of about 90%. Even though results of this preliminary study are of particular interest for the final reliability of the skin characterization system, it is worth remarking that a larger dataset should be considered to enforce the learning by example paradigm applied to this particular context.

Skin ageing evaluation

In order to characterize the skin surface acquired by means of the capacitive device, interesting features have been devised to sense changes of the skin micro-relief. Here, the skin ageing process has been addressed. As a matter of fact, it represents the most natural process of changes of the skin functions, which in turn has the most visible effect on the skin surface topography. Aged skin is

different from young skin: everybody knows, but quantifying these changes is a challenging task!

Three features have been presented: the first one is based on the area of the skin plateau that forms the typical pattern of the skin and is computed by using the watershed segmentation; the second feature is related to a multiresolution analysis carried out using the wavelet transform, whereas the last feature is based on a photometric property related to the local contrast of the enhanced skin wrinkles. After a necessary preprocessing stage, which tries to limit the effect of noise and differences in gray levels due to uncontrollable physiological factors proper of each individual, features have been evaluated on the available dataset.

The chosen ground truth related to the skin ageing effect has been found in the chronological age of the subjects analyzed. Despite several changes occur in the skin surface topography due to other environmental factors (exposure to UV solar radiation) or life habits (smoking, for example), the forearm region, chosen as the body site to sample, should present limited effect of these phenomena.

Results of the skin ageing evaluation have shown significant correlation between the devised features and the chronological age, demonstrating the ability to sense changes in the skin topographic structures as long as age increases. Nevertheless, this is the first time skin ageing has been addressed with such a system: other works have been dealing with optical devices, ultrasound scanner, optical or mechanical profilometers, suction methods exploiting mechanical properties of the skin tissue, to cite a few. However, even if the proposed system is low-cost with respect to other devices, results achieved are comparable to state-of-the-art evaluations of skin ageing. Moreover, the proposed prototype system is compact and could be easily integrated into portable devices with minimum efforts. This could be of a great importance for dermatologists and cosmetic scientists in order to achieve in-vivo quantitative evaluations of the skin conditions by using a routine approach.

Treatments follow-up analysis

The main advantage of using skin characterization systems is the possibility to achieve numerical results of the skin under examination. This can lead the typical approach of a subjective and qualitative evaluation of the skin surface, to objective and quantitative measurements of the changes occurred to the skin. Often this methodology is precluded due to high cost of the current skin characterization devices.

The proposed skin characterization system has been evaluated in a treatment follow-up setting. To this end, a simple hydrating treatment has been performed on the forearm region of a set of volunteers. Prior to have given the hydrating cream, skin forearm samples have been acquired by the system. After one hour from the cream application, another acquisition session has been performed on the same treated area. By comparing the results of features extracted before and after treatment, the system is able to quantify the effect of the hydrating cream application. In particular, as expected, all the subjects showed an improvement of their skin condition, measured (in percent) by the MLC feature, with respect to the pre-treatment condition. Detailed analysis of a skin sample replica achieved by optical profilometry, confirmed this behavior.

It is worth remarking that, although these are preliminary results, they are promising and could be of great importance for dermatologists and cosmetic scientists to measure the state of the skin health *routinely*.

Appendix A

Skin acquisition framework

In this section, some details about the developed application used for the skin surface characterization system are presented. Being a research work, the solution is based on two different development tools: a first framework is built in Matlab, whereas another prototype application is built in Microsoft Visual C#. The former serves as a rapid development tool in order to develop and test the skin characterization algorithms, in order to devise and extract a set of features from the capacitive image samples. The latter is used with two purposes: firstly, by means of the C# application interfaced with the device driver acquisition library (TCI) it is possible to acquire sequences of images from the capacitive sensor. Also, pressure information is acquired during the sample acquisitions. By storing and exporting the bitmaps of each acquisition of skin samples, a database collection is carried out for the Matlab analysis and validation steps. Secondly, once the devised features have been tested on the available dataset, the resulting algorithms are coded into the C# application for the prototype skin characterization system. The diagram of Figure A.1 depicts the relationship between all the components of the framework.

Being a preliminary work, all the code produced has been written without focusing on implementation performances and optimization for memory or speed.

Matlab implementation

The algorithms devised for extracting features from the skin capacitive images, are written in Matlab R14 (version 7.0.1 with service pack 3). Most of the image processing algorithms have been developed on purpose. For simplicity and

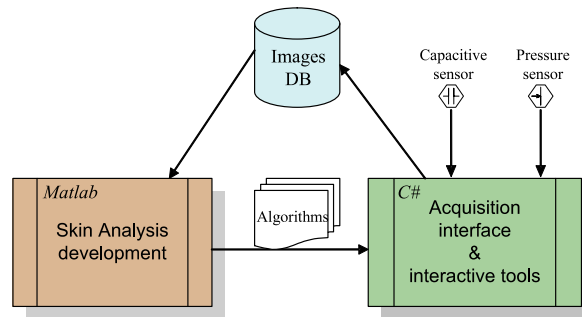


Figure A.1: The relationship between the components of the framework.

rapid prototyping, some functions of the Image Processing Toolbox have been used as well. A public available SVM tool has been used in order to train the model and to find the Support Vectors that better classify good quality against bad quality images. All the feature extraction and evaluations have been performed in batch mode, running the algorithms on the available dataset.

C# implementation

The UML class diagram of Figure A.2 depicts the main components of the C# application.

The diagram resembles the main classes and packages used in the application. Mainly, we have two distinct layers: a *Graphical User Interface* (GUI) which contains the main acquisition form and all the graphical custom controls needed to control the logic of the acquisition process by responding to user input and by presenting data to the user. Instances of the *PropertyBox* class can display results of the processing carried out in a $\langle \text{property}, \text{value} \rangle$ fashion. The GUI of the application is represented by the *AcquisitionForm* class that contains several controls for user input and processing output. A *ProcessingQueueControl* allow the user to select, from a list of registered *ImageProcessing* objects, which one has to be applied in the ordered set of image processing tasks after each image is presented to the user by calling the method *ApplyProcessingInQueue()*. A custom *SliderControl* allows the user to select a sample from the sequence of acquired images by clicking on the container of the control and determining a particular *CurrentPosition*. Events of the type *SliderEventArgs* are fired back to the GUI and appropriate actions are taken. Also, by using the arrow keys of the keyboard, the *SampleMoveNext()*, *SampleMovePrevious()*, are fired accordingly.

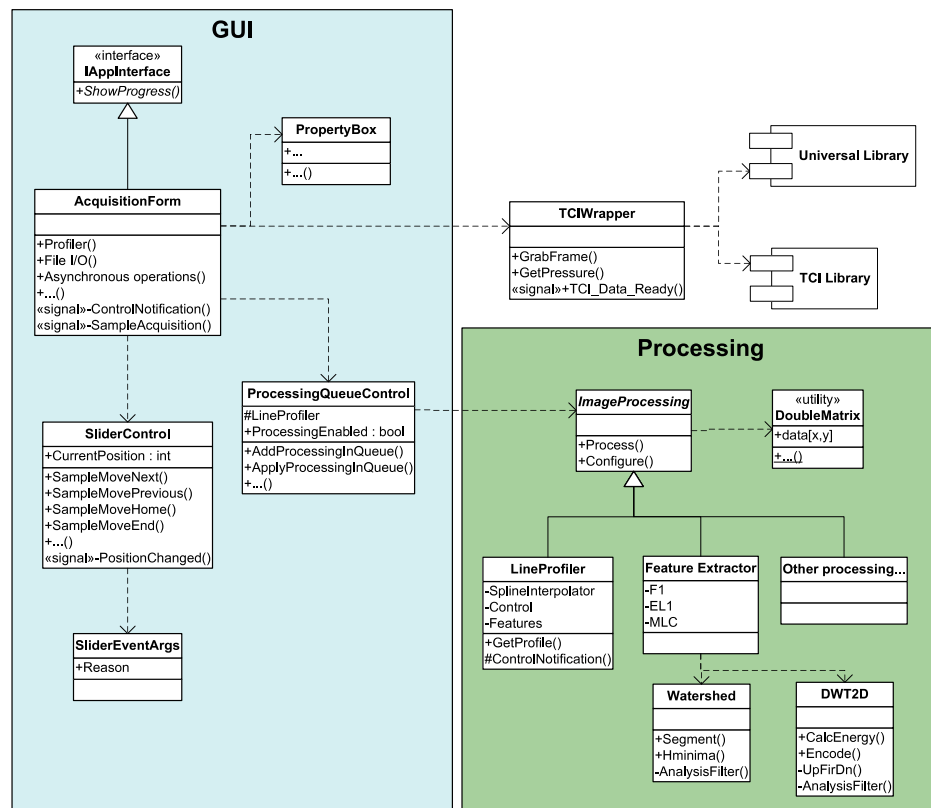


Figure A.2: The UML class static diagram of the main C# components.

Another layer, which is more computation oriented, is the processing layer. Here, an abstract class *ImageProcessing* is used as a prototype for the derived classes that implement the specific processing task, such as, for example, optical flow computation, image Gaussian filtering, or in this particular context, features extraction. The *Feature Extractor* class, for example, implements the abstract *Process()* method in order to compute the feature values out of the current selected capacitive image. Each *ImageProcessing* derived class has its own parameters, which can be adjusted to the user needs by the *Configure()* method of the abstract class. The processing is carried out by converting the input image into a *DoubleMatrix* object, which is an instance of a helper class providing basic matrix computation.

The application makes use of external libraries. A capacitive sensor image acquisition library (TCI.dll) is wrapped by importing all the API functions to interface the sensor image acquisition. The other external library (UL.dll) is used to interface the Digital Acquisition board (DAQ) where the pressure sen-

analogic output is converted into the digital domain. In this way, every acquired capacitive sample is associated with its own contact pressure value.

In Figure A.3 the C# application is presented. Here is where the acquisition

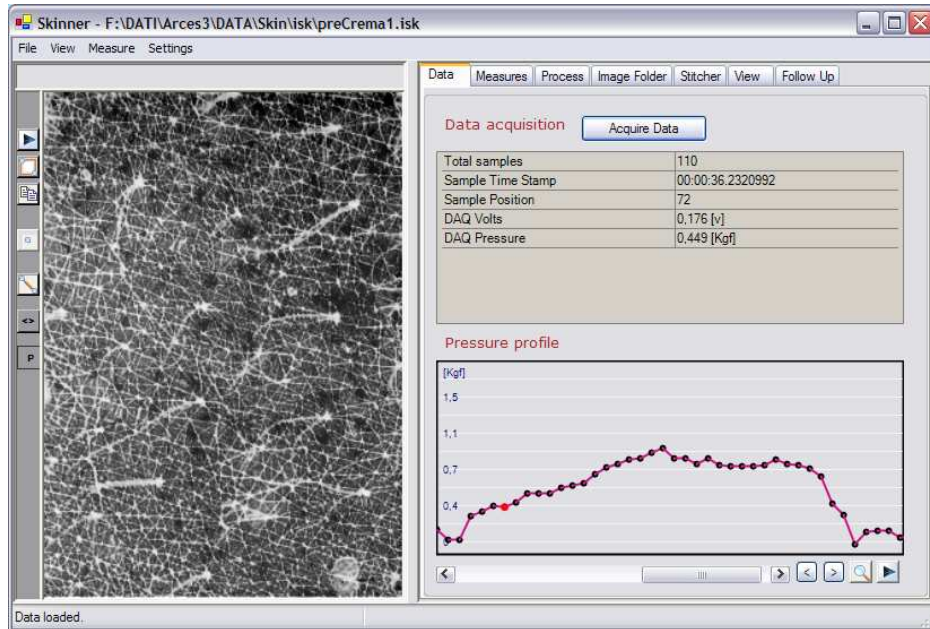


Figure A.3: The GUI of the C# application.

of the sequences of capacitive samples are performed. Along with each capacitive sample, the pressure graph gives numerical information about the contact pressure between the capacitive device and the subject's skin.

Some tools have been developed in order to interactively analyze the skin sample. The *Line Profiler* tool, for example is used to draw a line segment on the skin capacitive image in order to analyze the profile of wrinkles. Figure A.4 shows the line profiler used to extract information out of the skin samples. On the *PropertyBox* control, information regarding the current line segment are shown, such as mean roughness of the profile, distance between the two reference points, etc. To this end, the capacitive profile has been interpolated by natural cubic spline in order to achieve a sub-pixel accuracy.

Through this tool, comparative analyses between capacitive and profilometric images have been carried out.

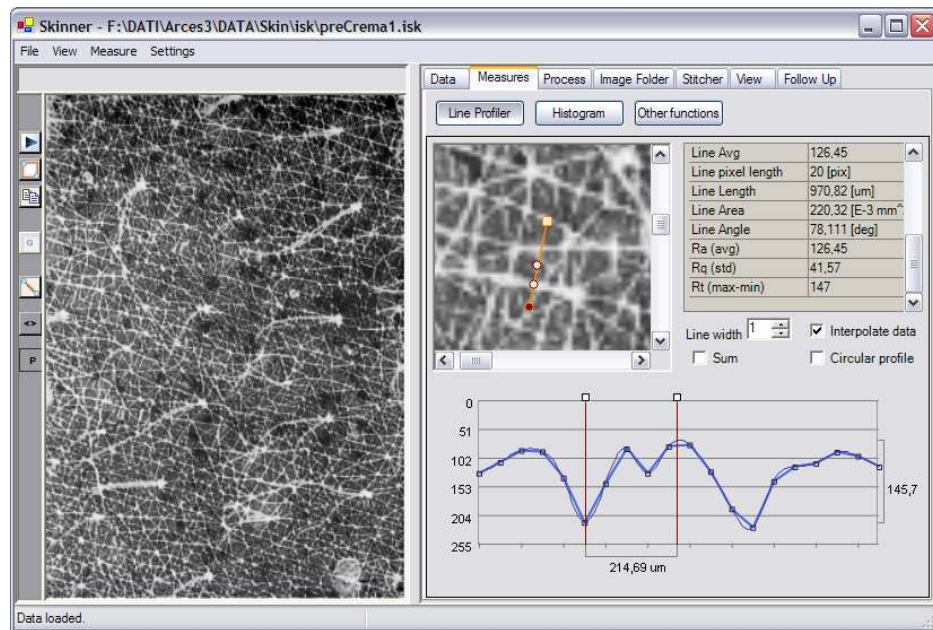


Figure A.4: The Line Profiler tool of the C# application.

Appendix B

Basic notions

In this appendix, some basic notions used in this dissertation are given.

Pearson correlation coefficient

Correlation analysis aims at measuring the degree of association between two variables x and y . We can say that there is a linear relationship between x and y , if a straight line, drawn through all the points as seen in a scatter diagram of the two variables, is the most appropriate for the observed relationship. The measure of how close is the linear relationship can be calculated by the Pearson Product Moment Correlation Coefficient given by:

$$r = \frac{\sum(x - \bar{x})(y - \bar{y})}{\sqrt{\sum(x - \bar{x})^2 \sum(y - \bar{y})^2}} \quad (\text{B.1})$$

The value of r varies in the range from -1 to $+1$ according to a negative or positive correlation, respectively, being the extremes an indication of perfect correlation. In fact, the absolute value of r is a measure of how close the observations lay on the straight line. The higher the magnitude of r the close the correlation.

Often, also the *p-value* is computed to estimate the reliability of the correlation. The *p-value* of an experiment is a random variable defined over the sample space of the experiment in such a way that the underlying distribution under the null hypothesis is uniform in the $[0, 1]$ interval. It is calculated by transforming the correlation to create a *t-test* statistic having $n - 2$ degrees of freedom, where n is the number of observation of the two variables. It is widely assumed that, the *p-value* is the probability of getting a correlation as large as the observed value by random chance when the true correlation is zero. If this

value is less than 0.05, then the correlation is significant. However, this is a common misunderstanding. [49]

Natural cubic spline interpolation

For a set $\{x_i\}$ of n knot points, $x_{i-1} < x_i, i = 1, \dots, n-1$, a cubic spline is the set of $n-1$ piecewise cubic polynomials between the data points so that:

$$S(x) = \begin{cases} S_1(x) & , x \in [x_0, x_1] \\ S_2(x) & , x \in [x_1, x_2] \\ \dots & \\ S_{n-1}(x) & , x \in [x_{n-2}, x_{n-1}] \end{cases} \quad (\text{B.2})$$

represents the spline function interpolating the n knot points values y_i , where each S_i is a cubic polynomial. In order to be a natural cubic spline, the $S(x)$ must be twice continuous differentiable ($S'_{i-1}(x_i) = S'_i(x_i)$ and $S''_{i-1}(x_i) = S''_i(x_i), i = 1, \dots, n-2$); must join up so that $S_{i-1}(x_i) = S_i(x_i), i = 1, \dots, n-2$ and at the borders must be $S''(x_0) = S''(x_{n-1}) = 0$.

The general form of a natural cubic spline is:

$$S_i(x) = \frac{z_{i+1}(x-x_i)^3 + z_i(x_{i+1}-x)^3}{6h_i} + \left(\frac{y_{i+1}}{h_i} - \frac{h_i}{6} z_{i+1} \right) (x-x_i) + \left(\frac{y_i}{h_i} - \frac{h_i}{6} z_i \right) (x_{i+1}-x) \quad (\text{B.3})$$

where $h_i = x_{i+1} - x_i$ is the length between two consecutive knot points.

The coefficients z_i can be found by solving the system of equations given by:

$$\begin{aligned} z_0 &= 0 \\ h_{i-1}z_{i-1} + 2(h_{i-1} + h_i)z_i + h_i z_{i+1} &= 6 \left(\frac{y_{i+1}-y_i}{h_i} - \frac{y_i-y_{i-1}}{h_{i-1}} \right) \\ z_n &= 0 \end{aligned} \quad (\text{B.4})$$

Amongst all twice continuously differentiable functions, natural cubic splines yield the least oscillation about the function f which is interpolated. Also, the spline is the configuration of minimal energy of an elastic strip constrained to n points.

Watershed segmentation

The watershed segmentation exploit geomorphology by considering region over which all points flow downhill to a common point. For example, is this

way rainfall flow to a single lake or river. This effect mostly depends on particular points, where maximal gradients magnitude is reached. These points forms the boundaries of what are called *watershed regions* or *catchment basins*. In order to find the watershed lines, regions must be identified first. The algorithm works by immersion simulation: by filling from the bottom, water is allowed to rise from each minimum, yielding catchment basins in the image. Watershed lines are built according when water rising from different catchment basins meet each other. In this way the segmentation is performed and each pixel of the catchment basins is assigned the same label. Supposing that the input image is within a gray-scale range, the general algorithm work as follows:

```

level ← 0
repeat
  Add pixel according to level
  if pixel added are close to existing watershed regions then
    join adjacent regions together
  else
    form new watershed regions
  end if
  level ← level + 1
until maximum level is reached

```

Each minimum of the input image give rise to a different catchment basins, and therefore watershed lines may not be referring to effective object of interest. In this case over-segmentation occurs. Noise is usually a source of such minima. In order to remove uninteresting minima, the *h-minima transform* can be used. Doing so will suppress all minima in the input intensity image whose depth is less than a given threshold value.

Gray Level Co-occurrence Matrix Features

Gray Level Co-occurrence Matrix (GLCM) of a gray-scale image I of size $m \times n$ is defined as

$$M(i, j) = \sum_{p=1}^n \sum_{q=1}^m \begin{cases} 1, & \text{if } I(p, q) = i \wedge I(p + \delta x, q + \delta y) = j \\ 0, & \text{otherwise} \end{cases} \quad (\text{B.5})$$

where δx and δy are the desired horizontal and vertical offset. Usually, since these offsets are dependent upon rotation, multiple offset are used when

computing the GLCM, accounting for angles between 0 and 180 degrees at the same distance radius to achieve a sort of rotation invariance.

The resulting GLCM M is a $N \times N$ symmetric matrix, where N is the quantization level of the original image (the maximum number of possible gray levels).

To obtain second order (a relationship between groups of two pixels) statistics features, a probability distribution is needed rather than on a count of occurrences. To this purpose, the GLCM M is normalized by dividing each element by the sum of all elements:

$$C_{i,j} = \frac{M_{i,j}}{\sum M_{i,j}} \quad (\text{B.6})$$

Common features extracted from this matrix (due to *Haralick* [34]) are:

$$\text{Energy (or Angular Second Moment): } \sum_{i,j=0}^{N-1} C_{i,j}^2$$

$$\text{Contrast: } \sum_{i,j=0}^{N-1} C_{i,j} (i-j)^2$$

$$\text{Homogeneity: } \sum_{i,j=0}^{N-1} \frac{C_{i,j}}{1+(i-j)^2}$$

$$\text{Dissimilarity: } \sum_{i,j=0}^{N-1} C_{i,j} |i-j|$$

$$\text{Entropy: } \sum_{i,j=0}^{N-1} C_{i,j} (-\ln(C_{i,j} + \epsilon))$$

$$\text{Centroid: } \mu_i = \sum_{i,j=0}^{N-1} i C_{i,j}, \mu_j = \sum_{i,j=0}^{N-1} j C_{i,j}$$

$$\text{Variance: } \sigma_i^2 = \sum_{i,j=0}^{N-1} C_{i,j} (i - \mu_i)^2, \sigma_j^2 = \sum_{i,j=0}^{N-1} C_{i,j} (j - \mu_j)^2$$

$$\text{Correlation: } \sum_{i,j=0}^{N-1} \frac{(i-\mu_i)(j-\mu_j)}{\sqrt{(\sigma_i)^2(\sigma_j)^2}}$$

These features have proved good texture characterization properties in many image processing context.

Publications

Journal

- [1] A. Bevilacqua, A. Gherardi and M. Ferri, Evaluation of skin ageing through wrinkle analysis in capacitive images. *International Journal of Modern Physics C (IJMPC)* Vol. 17, pp. 1663–1678, 2006.
- [2] A. Bevilacqua, A. Gherardi and R. Guerrieri, Predicting biological age from a skin surface capacitive analysis. *International Journal of Modern Physics C (IJMPC)* Vol. 15, pp. 1309–1320, 2004.

Conference Proceedings

- [3] A. Bevilacqua and A. Gherardi, A fast binary morphological operator for real time sequence analysis, *International Symposium on Nonlinear Theory and its Applications (NOLTA 2006)*, Bologna, Italy, September 11-14, pp.715–718, 2006.
- [4] A. Bevilacqua, A. Gherardi and R. Guerrieri, Measuring skin topographic structures through capacitance images analysis, *IEEE International Conference on Advanced Video and Signal based Surveillance (AVSS 2006)*, Sidney, NSW, Australia, November 22-24, pp. 53–57, 2006.
- [5] A. Bevilacqua and A. Gherardi, Measuring the skin surface changes due to hydrating treatments through capacitive images analysis, *International Symposium on Nonlinear Theory and its Applications (NOLTA 2006)*, Bologna, Italy, September 11-14, pp. 831–834, 2006.
- [6] A. Bevilacqua, A. Gherardi and R. Guerrieri, Studying skin ageing through wavelet-based analysis of capacitive images, *IEEE International Conference on Advanced Video and Signal Based Surveillance (AVSS 2005)*, Como, Italy, September 15-16, pp. 360–365, 2005.

- [7] A. Bevilacqua, A. Gherardi and R. Guerrieri, In vivo quantitative evaluation of skin aging by capacitance image analysis, *IEEE Workshop on Motion and Video Computing (WACV'05)*, Breckenridge, CO, USA, January 5-7, Vol. 1, pp. 342–347, 2005.
- [8] A. Bevilacqua and A. Gherardi, Age-related skin analysis by capacitance images, *17th IEEE IAPR International Conference on Pattern Recognition (ICPR 2004)*, Cambridge, UK, August 23-26, Vol. 2, pp. 703–706, 2004.

Bibliography

- [1] M. B. Purba, A. Kouris-Blazos, N. Wattanapenpaiboon, W. Lukito, E. Rothenberg, B. Steen, and M. L. Wahlqvist, "Can skin wrinkling in a site that has received limited sun exposure be used as a marker of health status and biological age?," *Age and Ageing*, vol. 30, pp. 227–234, 2001.
- [2] B. Marte, J. Finkelstein, and L. Anson, *Nature Insight: Skin Biology*, vol. 445. Nature Publishing Group, 2007.
- [3] H. Gray, *Grays Anatomy*. Lea & Febiger, Philadelphia, U.S.A., 1985.
- [4] D. Roop, "Defects in the barrier," *Science*, vol. 267, pp. 474–475, 1995.
- [5] F. Schellander and J. Headington, "The stratum corneum: some structural and functional correlates.," *British Journal of Dermatology*, vol. 91, pp. 507–515, 1974.
- [6] J. Leveque and P. Corcuff, *Noninvasive methods for the quantification of skin functions*. Springer, 1993.
- [7] R. O. Potts, E. M. Buras, and D. A. Chrisman, "Changes with age in moisture content of human skin.," *J Invest Dermatol*, vol. 82, pp. 97–100, 1984.
- [8] M. Gniadecka and G. B. E. Jemec, "Quantitative evaluation of chronological ageing and photoageing *in vivo*: studies on skin echogenicity and thickness," *British Journal of Dermatology*, vol. 139, pp. 815–821, 1998.
- [9] M. Yaar, M. S. Eller, and B. A. Gilchrest, "Fifty years of skin aging," *Journal of Investigative Dermatology*, pp. 51–58, 2002.
- [10] C. Escoffier, "Age related mechanical properties of human skin: an *in vivo* study.," *J Invest Dermatol*, vol. 93, pp. 353–357, 1989.
- [11] S. Diridollou, F. Patat, F. Gens, L. Vaillant, D. Black, J. M. Lagarde, Y. Gall, and M. Berson, "In vivo model of the mechanical properties of the human skin under suction," *Skin Research and Technology*, vol. 6, pp. 214–221, 2000.
- [12] P. A. Payne, "Measurement of properties and function of skin," *Clin. Phys. Physiol. Meas.*, vol. 12, pp. 105–129, 1991.

- [13] S. Grimnes, "Pathways of ionic flow through human skin in vivo.," *Acta Derm. Venereol.*, vol. 64, pp. 93–98, 1984.
- [14] J. J. B. Jack, D. Noble, and R. W. Tsien, *Electric current flow in excitable cells*. Oxford: Calderon Press., 1975.
- [15] J. Sato, M. Yanai, T. Hirao, and M. Denda, "Water content and thickness of the stratum corneum contribute to skin surface morphology.," *Arch Dermatol Res*, vol. 292, pp. 412–417, 2000.
- [16] D. Rallan and C. C. Harland, "Skin imaging: is it clinically useful?," *Clinical and Experimental Dermatology*, vol. 29, pp. 453–459, 2004.
- [17] J. Ulrich and C. Voit, "Ultrasound in dermatology: part ii, ultrasound of regional lymph node basins and subcutaneous tumours.," *Eur J Dermatol*, vol. 1, pp. 73–79, 2001.
- [18] M. Vogt, A. Knuttel, and K. Hoffman, "Comparison of high frequency ultrasound and optical coherence tomography as modalities for high resolution and non-invasive skin imaging.," *Biomed Technik*, vol. 48, pp. 116–121, 2003.
- [19] S. Richard, B. Querleux, and J. Bittoun, "In vivo proton relaxation times analysis of the skin layers by magnetic resonance imaging.," *J Invest Dermatol*, vol. 97, pp. 120–125, 1991.
- [20] S. D. Cotton, E. Claridge, and P. Hall, "Non-invasive skin imaging," in *Proc. of International Conference on Information Processing in Medical Imaging*, pp. 501–506, 1997.
- [21] A. J. Round, A. W. G. Duller, and P. J. Fish, "Lesion classification using skin patterning," *Skin Research and Technology*, vol. 6, pp. 183–192, 2000.
- [22] O. G. Cula and K. J. Dana, "Image-based skin analysis," in *Proceedings of Texture 2002 - The 2nd international workshop on texture analysis and synthesis, Copenhagen, Denmark*, pp. 35–41, June 1st 2002.
- [23] J. M. Lagarde, C. Rouvrais, D. Black, S. Diridollou, and Y. Gall, "Skin topography measurement by interference fringe projection: a technical validation," *Skin Research and Technology*, vol. 7, pp. 112–121, 2001.
- [24] U. Jacobi, M. Chen, G. Frankowski, R. Skgraven, M. Hund, B. Rzany, W. Sterry, and J. Lademann, "In vivo determination of skin surface topography using an optical 3D device," *Skin Research and Technology*, vol. 10, pp. 207–214, 2004.
- [25] C. Edwards, R. Heggie, and R. Marks, "A study of differences in surface roughness between sun-exposed and unexposed skin with age," *Photodermatology Photoimmunology & Photomedicine*, vol. 19, pp. 169–174, 2003.
- [26] S. Akazaki, H. Nakagawa, H. Kazama, O. Osanai, Y. Takema, and G. Imokawa, "Age-related changes in skin wrinkles assessed by a novel three-dimensional morphometric analysis," *British Journal of Dermatology*, vol. 147, pp. 689–695, 2002.

- [27] J. Sandby-Møller and H. C. Wulf, "Ultrasonographic subepidermal low-echogenic band, dependance of age and body site," *Skin Research and Technology*, vol. 10, pp. 57–63, 2004.
- [28] M. Rajadyaksha, M. Grossman, and D. Esterowitz, "In vivo confocal scanning laser microscopy of human skin: melanin provides strong contrast.," *J Invest Dermatol*, vol. 104, pp. 946–952, 1995.
- [29] J.-L. Lévêque and B. Querleux, "Skinchip, a new tool for investigating the skin surface *in vivo*," *Skin Research and Technology*, vol. 9, pp. 343–347, 2003.
- [30] J.-L. Lévêque and E. Goubanova, "Influence of age on the lips and perioral skin," *Dermatology*, vol. 208, pp. 307–313, 2004.
- [31] M. Tartagni and R. Guerrieri, "A fingerprint sensor based on the feedback capacitive sensing scheme," *IEEE Journal of Solid-state Circuits*, vol. 33, no. 1, pp. 133–142, 1998.
- [32] B. G. Rosen, L. Blunt, and T. R. Thomas, "On in vivo skin topography metrology and replication techniques," *In proc. of 7th International Symposium on Measurement Technology and Intelligent Instruments*, vol. 13, pp. 325–329, 2005.
- [33] W. R. Hendee and E. R. Ritenour, *Analytical description of Image Quality. Medical Image Physics (Fourth Edition)*, 2003.
- [34] R. M. Haralick, K. Shanmugam, and I. Dinstein, "Textural features for image classification," *IEEE Transactions on Systems, Man and Cybernetics*, vol. 3, pp. 610–621, 1973.
- [35] B. Boser, I. Guyon, and V. Vapnik, "A training algorithm for optimal margin classifiers," *In Proceedings of the Fifth Annual Workshop on Computational Learning Theory*, pp. 144–152, 1992.
- [36] V. Vapnik, *The Nature of Statistical Learning Theory*. Springer-Verlag, 1995. New York, NY.
- [37] "LIBSVM: a library for support vector machines." [Online], 2001. Software available at <http://www.csie.ntu.edu.tw/~cjlin/libsvm>.
- [38] A. K. Jain, S. Prabhakar, L. Hong, and S. Pankanti, "Filterbank-based fingerprint matching," *IEEE Transactions on Image Processing*, vol. 9, pp. 846–859, May 2000.
- [39] J. Varani, R. L. Warner, M. Gharaee-Kermani, S. K. Sem H Phan, J. Chung, Z. Wang, S. C. Datta, G. J. Fisher, and J. J. Voorhees, "Vitamin a antagonizes decreased cell growth and elevated collagen-degrading matrix metalloproteinases and stimulates collagen accumulation in naturally aged human skin," *Journal of Investigative Dermatology*, pp. 480–486, 2000.
- [40] L. Vincent and P. Soille, "Watersheds in digital spaces: An efficient algorithm based on immersion simulations," *IEEE Transactions on Pattern Analysis and Machine Intelligence*, vol. 13, pp. 583–598, June 1991.

- [41] P. Soille, *Morphological Image Analysis: Principles and Applications*. Springer-Verlag, 1999.
- [42] S. G. Mallat, "A theory for multiresolution signal decomposition: The wavelet representation.," *IEEE Transactions on Pattern Analysis and Machine Intelligence*, vol. 2, pp. 674–693, 1989.
- [43] U. P. Kappes, "Skin ageing and wrinkles: clinical and photographic scoring," *Journal of Cosmetic Dermatology*, vol. 3, pp. 23–25, 2004.
- [44] J. Kosecka, W. Zhang, and F. Li, "Mosaic construction from sparse set of views," *1st International Symposium on 3D Data Processing Visualization and Transmission (3DPVT 2002)*, pp. 123–125, 2002.
- [45] W. S. Hoge, H. Mamata, and S. E. Maier, "Efficient construction of histology slide mosaics via phase correlation registration of high resolution tiles," *Proc. of International Conference on Image Processing (ICIP03)*, pp. 1117–1120, 2003.
- [46] C. G. Harris and M. Stephens, "A combined edge and corner detector," *4th Alvey Vision Conference*, pp. 189–192, 1988.
- [47] D. G. Lowe, "Distinctive image features from scale-invariant keypoints," *International Journal of Computer Vision*, pp. 91–110, 2004.
- [48] M. A. Fischler and R. C. Bolles, "Random sample consensus: A paradigm for model fitting with applications to image analysis and automated cartography," *Communications of the ACM*, pp. 381–395, 1981.
- [49] J. Sterne and G. Smith, "Sifting the evidence - what's wrong with significance test?," *British Medical Journal*, pp. 226–231, 2001.